

UC Berkeley

UC Berkeley Electronic Theses and Dissertations

Title

Optical Injection Locking of Vertical Cavity Surface-Emitting Lasers: Digital and Analog Applications

Permalink

<https://escholarship.org/uc/item/3d88d14r>

Author

Parekh, Devang

Publication Date

2012

Peer reviewed|Thesis/dissertation

Optical Injection Locking of Vertical Cavity Surface-Emitting Lasers:

Digital and Analog Applications

by

Devang Parekh

A dissertation submitted in partial satisfaction of the

requirements for the degree of

Doctor of Philosophy

in

Engineering – Electrical Engineering and Computer Sciences

in the

Graduate Division

of the

University of California, Berkeley

Committee in charge:

Professor Constance Chang-Hasnain, Chair

Professor Ming Wu

Professor Junqiao Wu

Spring 2012

Optical Injection Locking of Vertical Cavity Surface-Emitting Lasers:
Digital and Analog Applications

© 2012

by Devang Parekh

Abstract

Optical Injection Locking of Vertical Cavity Surface-Emitting Lasers: Digital and Analog Applications

by

Devang Parekh

Doctor of Philosophy in Engineering – Electrical Engineering and Computer Sciences and the
University of California, Berkeley

Professor Constance J. Chang-Hasnain, Chair

With the rise of mobile (cellphones, tablets, notebooks, etc.) and broadband wireline communications (Fiber to the Home), there are increasing demands being placed on transmitters for moving data from device to device and around the world. Digital and analog fiber-optic communications have been the key technology to meet this challenge, ushering in ubiquitous Internet and cable TV over the past 20 years. At the physical layer, high-volume low-cost manufacturing of semiconductor optoelectronic devices has played an integral role in allowing for deployment of high-speed communication links. In particular, vertical cavity surface emitting lasers (VCSEL) have revolutionized short reach communications and are poised to enter more markets due to their low cost, small size, and performance. However, VCSELs have disadvantages such as limited modulation performance and large frequency chirp which limits fiber transmission speed and distance, key parameters for many fiber-optic communication systems. Optical injection locking is one method to overcome these limitations without re-engineering the VCSEL at the device level. By locking the frequency and phase of the VCSEL by the direct injection of light from another laser oscillator, improved device performance is achieved in a post-fabrication method.

In this dissertation, optical injection locking of VCSELs is investigated from an applications perspective. Optical injection locking of VCSELs can be used as a pathway to reduce complexity, cost, and size of both digital and analog fiber-optic communications. On the digital front, reduction of frequency chirp via bit pattern inversion for large-signal modulation is experimentally demonstrated showing up to 10 times reduction in frequency chirp and over 90 times increase in fiber transmission distance. Based on these results, a new reflection-based interferometric model for optical injection locking was established to explain this phenomenon. On the analog side, the resonance frequency enhancement was exploited for millimeter-wave radio over fiber communications. Experimental demonstration of 4 Gb/s data transmission over 20 km of fiber and 3 m of wireless transmission at a 60 GHz carrier frequency was achieved.

Additionally, optical injection of multi-transverse mode (MM) VCSELs was investigated showing record resonance frequency enhancement of > 54 GHz and 3- dB bandwidth of 38 GHz. Besides these applications, a number of other intriguing applications are also discussed, including an optoelectronic oscillator (OEO) and wavelength-division multiplexed passive optical networks (WDM-PON). Finally, the future of optical injection locking and its direction going forward will be discussed.

TABLE OF CONTENTS

TABLE OF CONTENTS.....	i
LIST OF FIGURES	iii
LIST OF TABLES.....	x
ACKNOWLEDGEMENT	xi
CHAPTER 1 OPTICAL INJECTION LOCKING OF VCSELS	1
1.1 INTRODUCTION	1
1.2 HISTORY OF OPTICAL INJECTION LOCKING.....	1
1.3 THEORY OF OPTICAL INJECTION LOCKING.....	3
1.3.1 Basic Concept and Experimental Setup	3
1.3.2 Classical Rate Equation Model.....	4
1.3.3 Reflection-based Rate Equation Model	5
1.3.4 Experiment.....	11
1.4 SUMMARY	14
CHAPTER 2 ANALOG APPLICATIONS OF OPTICALLY INJECTION LOCKED VCSELS 15	
2.1 MOTIVATION.....	15
2.2 RESONANCE FREQUENCY ENHANCEMENT	15
2.2.1 Single Transverse Mode VCSEL.....	15
2.2.2 Multi-Transverse Mode VCSEL.....	18
2.2.3 Resonance Frequency and 3-dB Bandwidth Enhancement	19
2.2.4 Spatial Detuning.....	23
2.2.5 Resonance Frequency Enhancement in Large Aperture VCSELS.....	25
2.2.6 Locking Range of Multimode VCSELS.....	27
2.2.7 Conclusion	28
2.1 MILLIMETER-WAVE RADIO OVER FIBER TRANSMISSION	29
2.1.1 Motivation.....	29
2.1.2 Optical Injection Locking for RoF.....	29
2.1.3 60 GHZ RoF without Master Laser Suppression.....	31
2.1.4 60 GHZ RoF with Master Laser Suppression.....	33
2.1.5 Conclusion	38
2.2 OPTOELECTRONIC OSCILLATOR	39
2.3 POLARITY-SWITCHABLE UWB-MONOCYCLE GENERATION.....	42
2.4 SUMMARY	44
CHAPTER 3 DIGITAL APPLICATIONS OF OPTICALLY INJECTION LOCKED VCSELS 45	
3.1 MOTIVATION.....	45
3.2 ADJUSTABLE PATTERN INVERSION	45
3.2.1 Single Transverse Mode VCSEL.....	45
3.2.2 Multi-Transverse Mode VCSEL.....	46
3.2.3 Background.....	47
3.2.4 Experimental Setup.....	47

3.2.5 Results.....	48
3.2.6 Discussion.....	52
3.2.7 Conclusion.....	53
3.3 PHASE MODULATION OF INJECTION LOCKED VCSELS.....	54
3.3.1 Theoretical modeling and simulation.....	54
3.3.2 Direct Detection Experiment.....	55
3.3.3 Coherent Demodulation Experiment.....	57
3.3.4 Results.....	57
3.3.5 Conclusions.....	59
3.4 ADVANCED MODULATION FORMATS.....	60
3.4.1 Discrete Multi-tone Modulation.....	60
3.4.2 Single Subcycle Modulation.....	63
3.5 WAVELENGTH-DIVISION MULTIPLEXED PASSIVE OPTICAL NETWORKS.....	64
3.5.2 Discussion and conclusion.....	67
3.5.3 WDM-PON with OIL-VCSELS.....	68
3.5.4 Experiment and Results.....	69
3.5.5 Summary.....	71
3.6 SIGNAL PROCESSING.....	72
3.6.1 Motivation.....	72
3.6.2 Concept and Working Principle.....	72
3.6.3 Experimental Setup and Time-Resolved Chirp after OIL.....	73
3.6.4 NRZ-to-RZ format conversion/Clock recovery.....	73
3.7 OPTICAL LOGIC GATES.....	74
3.7.1 Theory and Experimental Setup.....	75
3.7.2 Results.....	75
3.7.3 Conclusions.....	78
3.8 SUMMARY.....	78
CHAPTER 4 CONCLUSION.....	79
APPENDIX 1 METAL NANOPARTICLE AND QUANTUM DOT METAMATERIALS FOR NEAR RESONANT SURFACE PLASMON WAVEGUIDES.....	80
BIBLIOGRAPHY.....	94

LIST OF FIGURES

Figure 1.1 Historical timeline of optical injection locking through 1996.....	2
Figure 1.2 Historical timeline of optical injection locking of VCSELs until 2007	2
Figure 1.3 Typical experimental setup for optical injection locking of VCSELs. Different subsystems are included within application.....	3
Figure 1.4 Picture of basic experimental setup.....	4
Figure 1.5 Close-up of lensed fiber coupling and RF probing	4
Figure 1.6 OIL-VCSEL model with the interference effect. Total output field $E_t=E_s+E_r$. [50].....	6
Figure 1.7 OIL-VCSEL total output power where master laser's reflection is ignored [50]	7
Figure 1.8 OIL-VCSEL total output power where master laser's reflection is considered [50]	7
Figure 1.9 Relative magnitude response simulation for OIL-VCSEL small-signal frequency response curves for different detunings, compared with the free running case. [50]	8
Figure 1.10 Phase response for OIL-VCSEL small-signal frequency response curves for different detunings, compared with the free running case. [50]	9
Figure 1.11 Simulation results for 1 Gb/s data pattern for different detunings. [50]	9
Figure 1.12 . Simulation results for the RF response of the small-signal analysis at 1 GHz of the 1 Gb/s OOK large-signal modulation on the same locking map. [50].....	10
Figure 1.13 . Simulation results for the extinction ratio of the 1 Gb/s OOK large-signal modulation on the same locking map. The blue line indicates the conditions where $r_e=0$. [50].....	10
Figure 1.14 Magnitude RF response of the small-signal modulation of the OIL-VCSEL for different detunings (at a fixed injection ratio). [50].....	11
Figure 1.15 Phase RF response of the small-signal modulation of the OIL-VCSEL for different detunings (at a fixed injection ratio). [50].....	12
Figure 1.16 Simulation results for 1 Gb/s data pattern for different detunings. [50]	12
Figure 1.17 RF response of the small-signal modulation at 1 GHz [50]	13
Figure 1.18 Extinction ratio of the 1 Gb/s OOK large-signal modulation on the locking map. [50].....	13
Figure 2.1 Frequency response of an OIL VCSEL at various detuning values. A record resonance frequency of 107 GHz is shown. [53].....	16
Figure 2.2 Optical spectra of an OIL VCSEL at various detuning values. [53].....	17
Figure 2.3 Frequency response of an OIL VCSEL under various injection ratio levels. The detuning is adjusted to result in a resonance peak with ~ 20 dB gain for all the cases. [53]..	17
Figure 2.4 Optical spectra of an OIL VCSEL under various injection ratio levels. Both the power and the wavelength of the master laser are tuned. [53].....	18

Figure 2.5 3-dB frequency response enhancement of an OIL VCSEL to 80 GHz. [53]	18
Figure 2.6 Optical spectra of 10um MM VCSEL. The tranverse modes are spectrally and spatially distinct.[58].....	19
Figure 2.7 Schematic of MM OIL resonance frequency enhancement experimental setup.....	20
Figure 2.8 Optical spectra of 10 um 1550-nm multimode VCSEL under optical injection with constant injection ratio (~8.1 dB) and negative detuning. [58]	21
Figure 2.9 Frequency response of 10 um 1550-nm multimode VCSEL under optical injection with constant injection ratio (~8.1 dB) and negative detuning. [58]	21
Figure 2.10 Optical spectra of 10 um 1550-nm multimode VCSEL under optical injection with constant injection ratio (~9.03 dB) and positive detuning. Black trace is free running MM VCSEL. [58].....	22
Figure 2.11 Frequency response of 10um 1550-nm multimode VCSEL under optical injection with constant injection ratio (~9.03 dB) and positive detuning. Black trace is free running MM VCSEL. [58]	22
Figure 2.12 Optical spectra of 15um 1550-nm multimode VCSEL under optical injection with constant injection ratio (~6 dB) and negative detuning with 1 st order mode selected as the dominant mode. [58].....	23
Figure 2.13 Frequency response of 15um 1550-nm multimode VCSEL under optical injection with constant injection ratio (~6 dB) and negative detuning with 1 st order mode selected as the dominant mode. Dual peak in frequency response is due to dual polarization modes of the 1 st order mode. Black trace is the free running MM VCSEL. [58].....	24
Figure 2.14 Locking range for MM VCSEL with two transverse modes, optimized for locking on fundamental mode. [58].....	24
Figure 2.15 Small-signal frequency response for a 20 um aperture VCSEL. Resonance frequency increases from 2 GHz up to 12 GHz and 3-dB bandwidth of 15 GHz is obtained.....	25
Figure 2.16 Optical spectra for 20 μm aperture VCSEL. OIL occurs on the fundamental mode. The higher-order transverse modes and spontaneous emission are suppressed under external light injection	26
Figure 2.17 Small-signal frequency response for 30 um aperture VCSEL. Resonance frequency increases from 2 GHz up to 28 GHz and 3-dB bandwidth of 30 GHz is obtained.....	26
Figure 2.18 Optical spectra for 30 μm aperture VCSEL. OIL occurs on the fundamental mode. The higher-order transverse modes and spontaneous emission are suppressed under external light injection.	27
Figure 2.19 Optical spectra of MM VCSEL under optical injection at various detunings showing different locking regions of each transverse mode. Black trace is free running MM VCSEL[59]	28

Figure 2.20 Optical spectra of OIL VCSEL with single RF tone applied at different frequencies. Single sideband behavior is seen as frequency approaches cavity mode.....	29
Figure 2.21 Frequency response of different fiber lengths measured with the OIL VCSEL transmitter ($f_R=64$ GHz). Amplitude fluctuations lessen at 60 GHz, indicating less dispersion-induced fading for SSB modulation.....	30
Figure 2.22 Experimental setup of OIL VCSEL RoF transmission system	31
Figure 2.23 Small-signal frequency response with resonance frequency at 60 GHz after injection locking. Free running VCSEL response shown for comparison.....	31
Figure 2.24 Optical spectra of OIL VCSEL ROF link without modulation (black), with 60 GHz carrier (blue), and with 60 GHz carrier and ASK modulation.	32
Figure 2.25 BER curves for 2 Gb/s ASK baseband modulation of 60 GHz OIL VCSEL RoF link for B2B, 500 m and 1 km fiber.....	33
Figure 2.26 Experimental setup of OIL VCSEL RoF transmission system with wireless transmission	33
Figure 2.27 Optical spectra of OIL VCSEL RoF link with filters and EDFAs and without modulation (black), with 60 GHz carrier (blue), and with 60 GHz carrier and ASK modulation.	34
Figure 2.28 EVM versus received optical power for 1 and 2 Gb/s subcarrier modulated QPSK signals on 60 GHz OIL VCSEL RoF link for B2B and 20 km fiber and 3 m wireless transmission.	34
Figure 2.29 BER curves for 2 and 3 Gb/s ASK baseband modulation of 60 GHz OIL VCSEL RoF link for B2B (dashed) and 20km fiber, and 3 m wireless transmission.....	35
Figure 2.30 Eye diagrams of 2 and 3 Gb/s ASK baseband modulation after 60 GHz OIL VCSEL RoF link for B2B (-9.5 dBm 2 Gb/s/-9 dBm 3 Gb/s) and 20km (10.5 dBm 2 Gb/s /-10 dBm 3 Gb/s) fiber and 3 m wireless transmission	36
Figure 2.31 BER curves for 4 Gb/s ASK baseband modulation of 60 GHz OIL VCSEL RoF link for B2B and 10km fiber, and 3 m wireless transmission.....	36
Figure 2.32 RF spectrum of 1Gb/s QPSK subcarrier located 1 GHz away from the 60 GHz carrier after propagation over 20 km SSMF and 3 m wireless.	37
Figure 2.33 Constellation diagrams for 1 and 2 Gb/s subcarrier modulated QPSK signals on 60 GHz OIL VCSEL RoF link after for B2B fiber and 3 m wireless transmission at different received powers (-15 dBm for 1 and 2 Gb/s, -10 dBm for 1 Gb/s and -8 dBm for 2 Gb/s).....	37
Figure 2.34 EVM versus received optical power for 1 and 2 Gb/s subcarrier modulated QPSK signals on 60 GHz OIL VCSEL RoF link for B2B and 20 km fiber and 3 m wireless transmission.	38
Figure 2.35 SNR versus received optical power for 1 and 2 Gb/s subcarrier modulated QPSK signals on 60 GHz OIL VCSEL RoF link for B2B and 20 km fiber and 3 m wireless transmission.	38
Figure 2.36 Experimental of OIL-based OEO showing DFB based experimental setup	40

Figure 2.37 Thermal isolation of OIL-based OEO experimental setup using insulation and Plexiglas.....	40
Figure 2.38 Open loop (blue) versus closed loop (red) operation of OEO. Enhancement of the cavity mode is seen in closed loop operation.[70].....	41
Figure 2.39 Phase noise spectra of OIL VCSEL OEO versus a HP 83650 signal generator.[70].....	41
Figure 2.40 RF spectrum of OIL VCSEL-OEO at 20 GHz (red) versus an HP signal generator (grey).[70].....	42
Figure 2.41 Experimental setup of multifunctional generator using a chirp adjustable injection-locked VCSEL followed by a tunable interferometer. [71].....	42
Figure 2.42 Polarity-switchable differentiator from positive and negative slope of DLI. [71]....	43
Figure 2.43 Measured UWB-monocycles using multi-mode VCSEL under OIL. [71].....	43
Figure 2.44 RF spectrum of the UWB-monocycle of Figure 2.37 showing 129% fractional bandwidth at 5.1 GHz. [71].....	44
Figure 3.1 Transmission measurements demonstrating distance enhancement of a direct-modulated OIL VCSEL with negative chirp at 10 Gb/s. Eye diagrams for OIL VCSEL at back-to-back (B2B), after 25-km and 100-km transmission are shown.[72]	46
Figure 3.2 Schematic of experimental setup for frequency chirp study	47
Figure 3.3 Optical spectra of the same 15 μm MM VCSEL modulated at 10 Gb/s free-running (top) and under injection locking (bottom). VCSEL bias is shown for each.[76]....	48
Figure 3.4 Measured intensity and chirp waveforms for free-running and R=6 dB optically injection-locked 10 μm aperture MM VCSELs. The peak-to-peak transient (above line) and adiabatic (below line) chirp are reduced by a factor of 6 through injection locking. [76].....	49
Figure 3.5 Measured intensity and chirp waveforms for free-running, R=3 dB, and R=6 dB optically injection-locked 15 μm aperture MM VCSELs. The peak-to-peak transient (above line) and adiabatic (below line) chirp are reduced by almost a factor of 3 through injection locking.[76].....	50
Figure 3.6 Transmission measurements demonstrating distance enhancement of a direct-modulated OIL 10 μm aperture MM VCSEL with negative chirp at 10 Gb/s. [76].....	51
Figure 3.7 Optical eye diagrams for OIL VCSEL at 0 km, after 25, 55 and 85-km transmission are shown. [76]	51
Figure 3.8 Transmission measurements demonstrating distance enhancement of a directly-modulated OIL 15 μm aperture MM VCSEL at R=3 and 6 dB at 10 Gb/s. [76]	52
Figure 3.9 Eye diagrams for OIL VCSEL at 0 km and after fiber transmission are shown. [76].....	52
Figure 3.10 Interferometric model of optically injection locked VCSEL. Top path represents light entering VCSEL cavity, where OIL rate equations determine output. Bottom path represents reflection off top facet inducing a $\sim\pi$ phase shift	53

Figure 3.11 Vector based representation of OIL reflection model.[78]	54
Figure 3.12 QPSK transmitter using phase-modulated OIL. [78]	54
Figure 3.13 Simulated phase modulation at transition state of OIL VCSEL. [78].....	55
Figure 3.14 8-PSK transmitter based on phase-modulated OIL VCSEL. [78].....	55
Figure 3.15 Interferometry-based experimental setup for phase modulation.	56
Figure 3.16 Phase modulation of OIL-VCSEL using interferometric setup	56
Figure 3.17 Experimental setup for phase modulation of injection locked VCSELs.....	57
Figure 3.18 Amplitude and phase of 10 Gb/s modulated OIL VCSEL for DPSK modulation....	58
Figure 3.19 Output of both ports of DLI with OIL VCSEL modulated at 10 Gb/s and PRBS7 ..	58
Figure 3.20 Experimental setup for 8-PSK combining an OIL VCSEL with two modulators. ...	59
Figure 3.21 8-PSK combing an OIL VCSEL with two phase modulators generating QPSK.	59
Figure 3.22 Step-by-step guide to DMT generation and reception	61
Figure 3.23 Step-by-step guide to DMT generation and reception	62
Figure 3.24 Step-by-step guide to DMT generation and reception	62
Figure 3.25 Test setup for single subcycle modulation of VCSEL	63
Figure 3.26 Constellation diagram of received 16-QAM single subcycle modulation.	64
Figure 3.27 Experimental setup for feedback insensitivity in VCSEL-based PON at orthogonal polarization. [86]	64
Figure 3.28 Optical spectra of upstream and downstream data with downstream DFB spectra superimposed on upstream VCSEL spectra. [86].....	65
Figure 3.29 Bit error rate of each case with downstream and upstream transmission alone shown as reference. [86]	65
Figure 3.30 Bit error rate versus received optical power of upstream VCSEL transmission under different optical feedback powers. Critical feedback occurs at -9 dB. [86]	66
Figure 3.31 Bit error rate of upstream VCSEL transmission at -30.5 dBm received optical power with downstream transmission at various optical feedback powers. Critical feedback is -16 dB. [86].....	67
Figure 3.32 WDM-PON with OIL_VCSELs and 3-dB couplers. The slave VCSEL at each optical network unit (ONU) is injection-locked by the modulated downstream signal transmitted from the master DFB laser at the central office (CO).....	68
Figure 3.33 Experimental Setup for WDM-PON based on OIL VCSEL.....	69
Figure 3.34 Electrical eye diagrams (green) for free running, -27.4 dB injection ratio and - 31.4 dB injection ratio at error-free condition. Optical eye diagrams (yellow) prior to upstream transmission. [91].....	70
Figure 3.35 Upstream BER of 2.5 Gb/s 2^{23} -1 PRBS directly modulated OIL and free running VCSELs for 17 km transmission. [91].....	71

Figure 3.36 Concept of multifunctional generator using optical injection-locked (OIL) VCSEL followed by a delay-line interferometer (DLI). Three unique and reconfigurable functions are generated by utilizing the adjustable-chirp from the OIL-VCSEL and subsequent tunable filtering.[71]	72
Figure 3.37 Time-resolved frequency chirp measurement of OIL-VCSEL under the transition state.[71].....	73
Figure 3.38 (a) Rising-edge detection (b) Falling-edge detection (c) eye diagrams of NRZ and format converted RZ from the rising-edge detection. [71]	74
Figure 3.39 (a) Edge detection of both rising and falling edges. (b) RF spectrum showing the recovered 10-GHz clock and the 0.3 MHz tone spacing.[71].....	74
Figure 3.40 OIL-based NOT gate based on wavelength detuning.....	75
Figure 3.41 OIL-based NOT gate based on injection ratio change	76
Figure 3.42 All-optical NOT gate based on OIL injection ratio change	76
Figure 3.43 Switching of inversion by injection ratio modulation of an OIL VCSEL.....	77
Figure 3.44 Switching of inversion by injection ratio modulation of an OIL VCSEL.....	77
Figure 3.45 All-optical NOT-gate by wavelength detuning of master #2	78
Figure 4.1 Real part of dielectric constant of the metallodielectric metamaterial plotted as a function of wavelength and fill factor for a background dielectric constant of 5.	83
Figure 4.2 Imaginary part of dielectric constant of the metallodielectric metamaterial plotted as a function of wavelength and fill factor for a background dielectric constant of 5.....	83
Figure 4.3 Real part of dielectric constant of the metallodielectric metamaterial plotted as a function of wavelength for different background dielectric constants.	84
Figure 4.4 Imaginary part of dielectric constant of the metallodielectric metamaterial plotted as a function of wavelength for different background dielectric constants.	84
Figure 4.5 Dielectric constant of the metallodielectric quantum dot metamaterial plotted as a function of wavelength for different fill factors (η) at a constant background dielectric constant ($\epsilon=12$)	87
Figure 4.6 Dielectric constant of the metallodielectric quantum dot metamaterial plotted as a function of wavelength for different fill factors (η) at a constant background dielectric constant ($\epsilon=12$).	87
Figure 4.7 Dielectric constant of the metallodielectric with two-level system metamaterial plotted as a function of wavelength for different background dielectric constants at a constant fill factor ($\eta=0.3$).....	88
Figure 4.8 Imaginary part of dielectric constant of the metallodielectric with two-level system metamaterial plotted as a function of wavelength for different background dielectric constants at a constant fill factor ($\eta=0.3$).	88

Figure 4.9 Propagation length for metallodielectric metamaterial surface plasmon waveguide plotted versus $\text{Ag } \epsilon''$ without QDs. As ϵ'' reduces towards 0, the propagation length increases exponentially. 90

Figure 4.10 Confinement for metallodielectric metamaterial surface plasmon waveguide plotted versus $\text{Ag } \epsilon''$ without QDs, Maximum confinement is reached at $\epsilon''=0$, as expected. 91

Figure 4.11 Propagation length plotted against wavelength for optimized metallodielectric metamaterial with QDs. Longer than Ag/SiO₂ surface plasmon waveguide propagation lengths are seen at ~553nm. 91

Figure 4.12 Confinement plotted against wavelength for optimized metallodielectric metamaterial with QDs. Confinement in the “metal” and “dielectric” are shown to be <50nm at the wavelengths of longest propagation (~553nm). 92

LIST OF TABLES

Table 1.1 Parameters for injection locking rate equations.....	5
Table 4.1 Values of macroscopic dielectric constant at 550 nm wavelength, optimized with respect to ε_{MAC}'' , with the condition that $ \varepsilon_{MAC}' $ should be ~ 5 ,	85

ACKNOWLEDGEMENT

I would like to thank my advisor, Professor Connie J. Chang-Hasnain, for her continual support and encouragement during the completion of my dissertation. I have learned from her so much during the past 8 years and I am eternally grateful to her for giving me the opportunity to be part of CCHG. I would also like to thank Professor Ming C. Wu and Junqiao Wu for reviewing this dissertation.

I would like to thank my current and former labmates in CCHG for their helpful suggestions and discussions. Especially, I would like to thank Xiaoxue Zhao, Erwin Lau, Weijian Yang, Peng Guo, Carlos Mateus and Mike Huang, for their help and support. Moreover, I would also like to thank my collaborators Prof. Lars Thylen, Prof. Markus C. Amann, Prof. Fumio Koyama, Prof. Ivan Kaminow, Davide Fortusini, Anthony Ng'Oma, Werner Hofmann, Michael Müller, Bo Zhang, Omer Yilmaz, SeungHun Lee, Roberto Rodes, Thang Pham, Hyuk-Kee Sung, Julian Treu, and Markus Horn for their collaboration as well as many others.

Finally, I would like to thank my parents and my brother for their everlasting help and support.

Chapter 1 Optical Injection Locking of VCSELs

1.1 Introduction

Optical injection locking and its predecessors have been studied for over 400 years. Over time, the underlying physics have been explored and its benefits experimentally verified. In the past 20 years, optical injection locking of VCSELs has brought this technique to a low cost, more efficient platform which provides enhancements for new applications, which will be explored in the following chapters. Moreover, a better physical model for optical injection locking that elucidates the physical phenomena that occur has been created.

1.2 History of Optical Injection Locking

The historical underpinnings of optical injection locking of VCSELs start from the 17th century. Huygens observed “an odd kind of sympathy” between two pendulums swinging from the same bar, where after some period of time both pendulums would synchronize [1]. This coupled oscillation can be thought of as a mutually injection locked system where each oscillator locks the other via the bar until an equilibrium state is reached. In 1966, this phenomenon was demonstrated for injection locking of lasers for the first time, but with the addition of an isolator between the lasers so only one laser is locked [2]. This experimental work with HeNe lasers showed qualitative evidence of locking the secondary laser to the first. In 1980, experimental demonstration of injection locking of semiconductor lasers was shown, with theoretical rate equations of this phenomenon being published a year later [3–5]. This led to further work characterizing device performance improvements in frequency chirp, resonance frequency enhancement and noise reduction by optical injection locking [6–30].

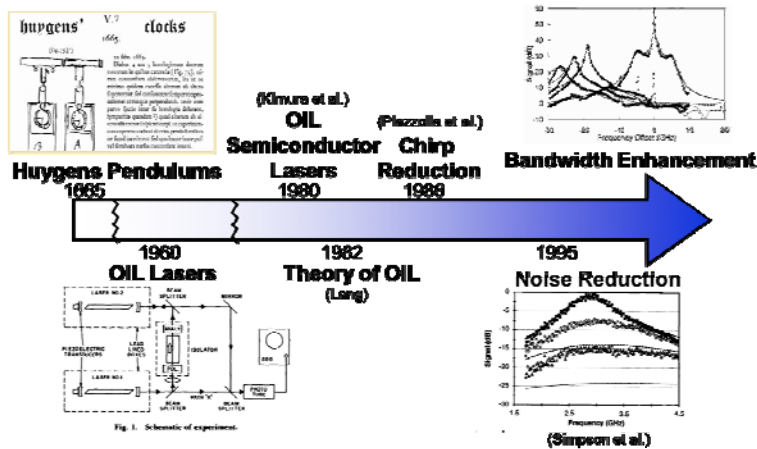


Figure 1.1 Historical timeline of optical injection locking through 1996

In the early 1990s, the first experiments on injection locking of VCSELs were demonstrated, recreating the phenomena seen in other semiconductor lasers, including resonance frequency enhancement and noise reduction [31]. Long wavelength ($> 1.1 \mu\text{m}$) VCSEL injection locking research started in the early 2000s, to bring this phenomenon to a low cost platform that still can be used for longer range fiber communications. Noise reduction, chirp reduction, and a few applications were shown but the main contribution of this work was the record resonance frequency enhancement to over 107 GHz for a semiconductor laser, the highest measured directly modulated laser ever [32–48]. With all these historical achievements on understanding the underlying physics and improving performance in singular areas, this thesis looks at using these to build better systems and applications that exploit these performance improvements.

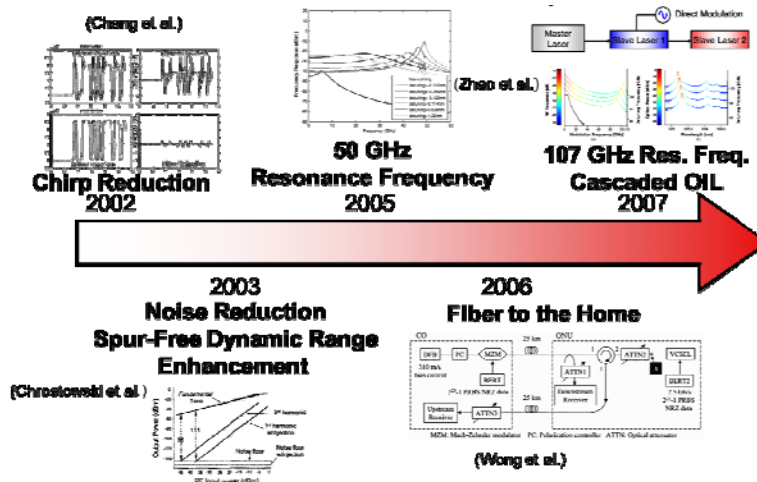


Figure 1.2 Historical timeline of optical injection locking of VCSELs until 2007

1.3 Theory of Optical Injection Locking

1.3.1 Basic Concept and Experimental Setup

The concept of optical injection locking at a cursory level is very simple. One laser oscillator, usually referred to as the master laser, injects its output light into another laser oscillator, referred to as the slave laser, locking the second laser oscillator in phase and frequency to the first. One can then tune either of the lasers to extract performance enhancements or underlying dynamics of the slave laser. Section 1.2 has gone over previous work in this area, while this thesis will cover new theoretical models and experimental results.

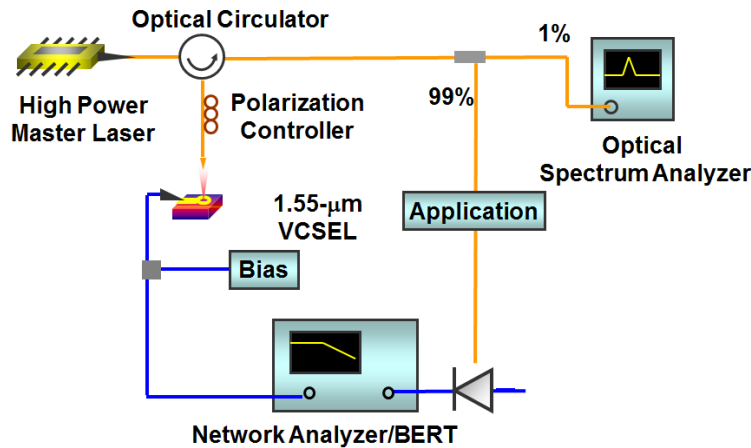


Figure 1.3 Typical experimental setup for optical injection locking of VCSELs. Different subsystems are included within application.

One of the new innovations in optical injection locking and especially of injection locking of VCSELs has been the advancement in the experimental platform. Previously, the majority of injection locking experiments had used free space bulk optics for coupling and isolation, poor thermal control of slave laser temperature, and poor impedance matching to the slave laser. This led to issues with coupling losses limiting the injection ratio, wavelength drift over time, and limited RF performance. In our setup, we have solved these issues by creating a platform where $>90\%$ of the output light of the VCSEL is captured and $>90\%$ of the injected light goes to the VCSEL, while keeping the temperature stable to ± 0.02 $^{\circ}\text{C}$, and impedance matching is limited by the intrinsic VCSEL impedance. A schematic of the basic setup is seen in Figure 1.3 with a picture of an experimental setup seen in Figure 1.4. Figure 1.5 shows a close up of the RF probing and lensed fiber coupling.

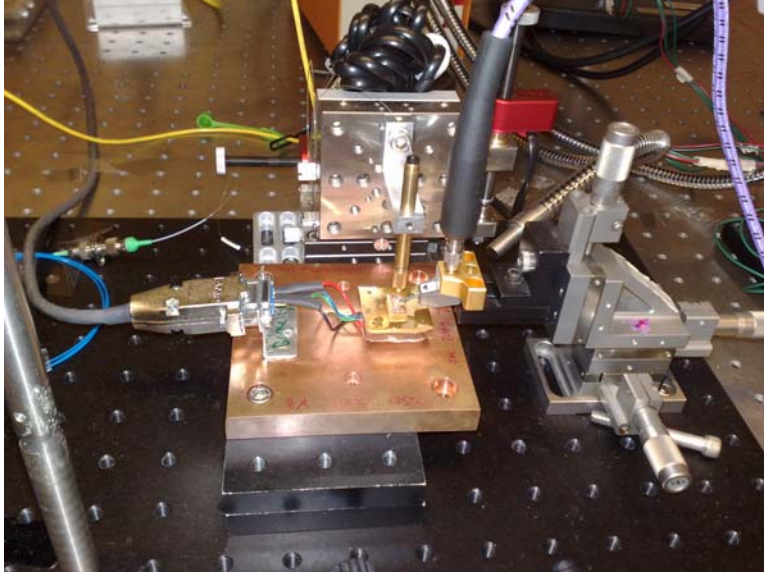


Figure 1.4 Picture of basic experimental setup

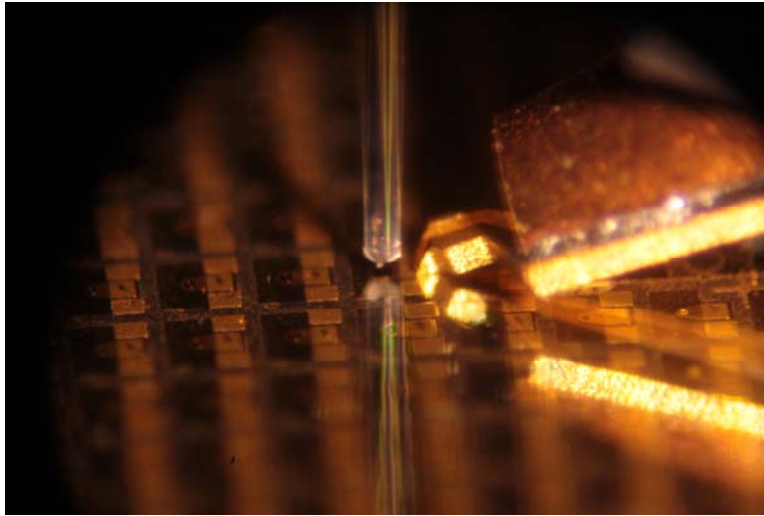


Figure 1.5 Close-up of lensed fiber coupling and RF probing

1.3.2 Classical Rate Equation Model

Starting from the rate equations formulated by Lamb to describe semiconductor lasers, a few simple modifications can be made to describe an optically injection locked semiconductor laser system [49].

$$\frac{dE(t)}{dt} = \frac{1}{2} g [N(t) - N_{th}] E(t) + \kappa E_{inj} \cos \phi(t) \quad (1.1)$$

$$\frac{d\phi(t)}{dt} = \frac{\alpha}{2} g [N(t) - N_{th}] E(t) - \kappa \frac{E_{inj}}{E(t)} \sin \phi(t) - \Delta\omega_{inj} \quad (1.2)$$

$$\frac{dN(t)}{dt} = J - \gamma_N N(t) - \{ \gamma_P + g [N(t) - N_{th}] \} E(t)^2 \quad (1.3)$$

Equations 1.1, 1.2, and 1.3 are the injection locking rate equations that have been thoroughly derived and studied in previous papers [3], [11], [12]. The variables used in these rate equations are described in Table 1.1. The key additional parameters are the injection field, E_{inj} , and the phase between the two laser fields, $\phi(t)$. These additional terms allow for the manipulation of the dynamics of the slave laser, by either changing the injected power or by changing the frequency separation between the two lasers. These terms are commonly referred to as injection ratio and wavelength detuning, respectively.

Variable	Description
$E(t)$	Slave laser field
$E^2(t)$	Square of injected laser field (# of photons $S(t)$)
E_{inj}	Master laser field injected into slave laser
g	Gain coefficient = $\Gamma v_g g_n / V_a$
$N(t)$	# of carriers
N_{th}	Threshold carrier number
$\phi(t)$	Phase difference between master and slave laser field
α	Linewidth enhancement factor
$\Delta\omega$	$\omega_{inj} - \omega_{FR}$
J	Carrier density
γ_N	Carrier recombination rate
γ_P	Photon decay rate
κ	Coupling coefficient = $(v_g/2L)(1-R)^{1/2}$
Γ	Confinement factor of slave laser
v_g	Group velocity of field inside cavity
R	Mirror reflectivity of slave laser
L	Slave laser cavity length
g_n	Differential gain of slave laser
V_a	Volume of the active region of the slave laser

Table 1.1 Parameters for injection locking rate equations

1.3.3 Reflection-based Rate Equation Model

Figure 1.6 shows the schematic of an optically injection locked VCSEL with master reflection accounted for. The master laser field E_{inj} impinges onto the front facet of the VCSEL and is split into transmitted and reflected fields [50]. The transmission interacts with the VCSEL cavity, described by the standard injection locking rate equations. A steady state is reached inside the cavity and its output E_s is phase coherent with E_{inj} , with a phase shift φ_s ranging from -0.5π to $\cot^{-1}\alpha$. φ_s which is determined by the wavelength detuning described earlier [33], [51].

The total output field E_t is the sum of the slave field, E_s and the reflection of the master laser $E_{inj}r$, where r is the reflectivity of the top facet of the VCSEL, with a phase shift φ_r depending on VCSEL's top mirror structure and λ_m . In previous models, only the interaction of

the injected laser field and slave laser field was considered and, therefore, the interference between E_s and $E_{inj}r$ was ignored. The total output power of the steady state can now be written in equation form as,

$$P_t = P_s + P_{inj}r^2 + 2\sqrt{P_s P_{inj}}r \cos(\varphi_s - \varphi_r) \quad (1.4)$$

where P_s and P_{inj} are the optical power corresponding to the electrical fields E_t and E_{inj} respectively. Figure 1.7 shows the output power for a simulated OIL-laser neglecting the master laser reflection. Figure 1.8 shows the output power when the interference effect of master laser reflection is taken into account. The total output power P_t increases with injection ratio (defined as $10 \cdot \log_{10}(P_{inj}/P_{fr})$, where P_{fr} is the slave laser free running output power), which is the same in both cases. With the inclusion of reflection (Figure 1.8), however, P_t decreases with detuning. This is because φ_s increases from -0.5π to $\cot^{-1}\alpha$, leading to a more destructive interference and therefore a lower total output power.

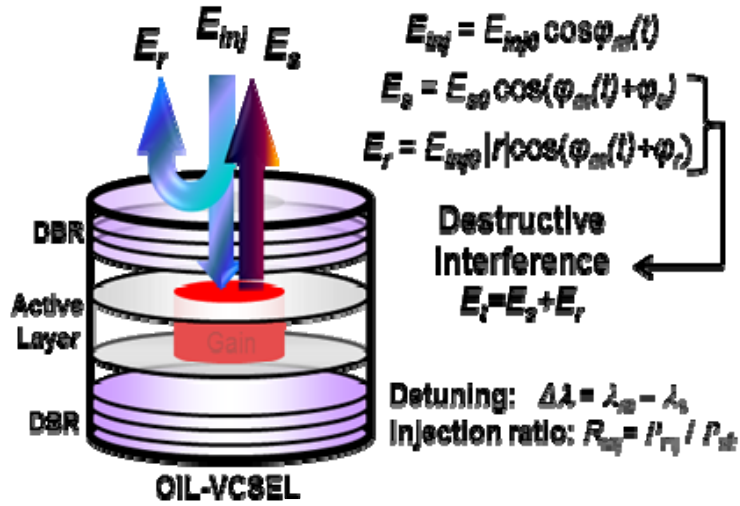


Figure 1.6 OIL-VCSEL model with the interference effect. Total output field $E_t = E_s + E_r$. [50]

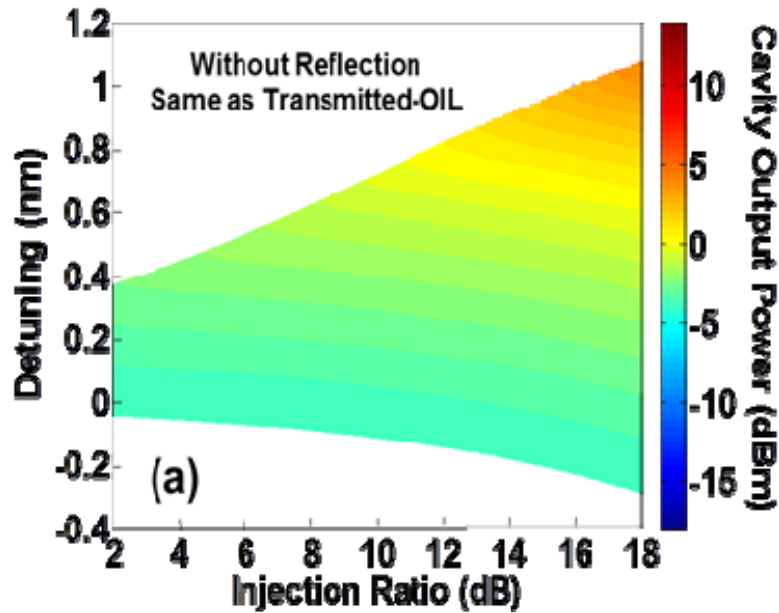


Figure 1.7 OIL-VCSEL total output power where master laser's reflection is ignored [50]

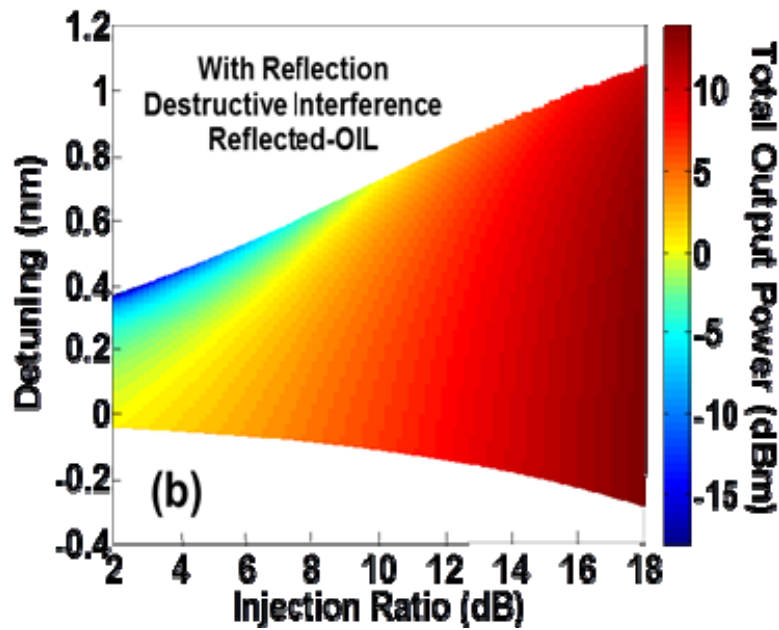


Figure 1.8 OIL-VCSEL total output power where master laser's reflection is considered [50]

Small signal analysis is then simulated based on the injection locking rate equations with the master reflection now accounted for [3], [18], [33], [51]. Under modulation the output power of the slave laser and its phase both experience a perturbation, which can be represented as ΔP_s and $\Delta \varphi_s$ respectively. Now based on Equation 1.4 the total output power can be represented as

$$P_t + \Delta P_t = (P_s + \Delta P_s) + P_{inj} r^2 + 2\sqrt{(P_s + \Delta P_s)P_{inj}} r \cos(\varphi_s + \Delta\varphi_s - \varphi_r) \quad (1.3)$$

Figure 1.9 shows the small-signal frequency response of ΔP_t for different detunings, with the magnitude referenced to the free running case. As the master laser is detuned from blue (shorter wavelength) to red (longer wavelength), a low frequency/DC suppression is seen in the magnitude response. The DC-suppression is caused by a π phase change in the phase response, which displays itself as a pattern inversion under large signal modulation (Figure 1.10). Furthermore, this DC suppression condition is the exact state that the transition (between inversion and normal pattern) state occurs at under large signal modulation. This DC suppression can be attributed to the destructive interference between the OIL-VCSEL internal output field, E_s , and the master laser reflection light, E_r , off the top facet. Also, by increasing the detuning, the DC-suppression vanishes and a large RF gain is obtained at low frequencies, which can also be attributed to the interference effect. Therefore, once can predict the polarity and qualitative magnitude of large signal-modulation from the small-signal magnitude and phase response.

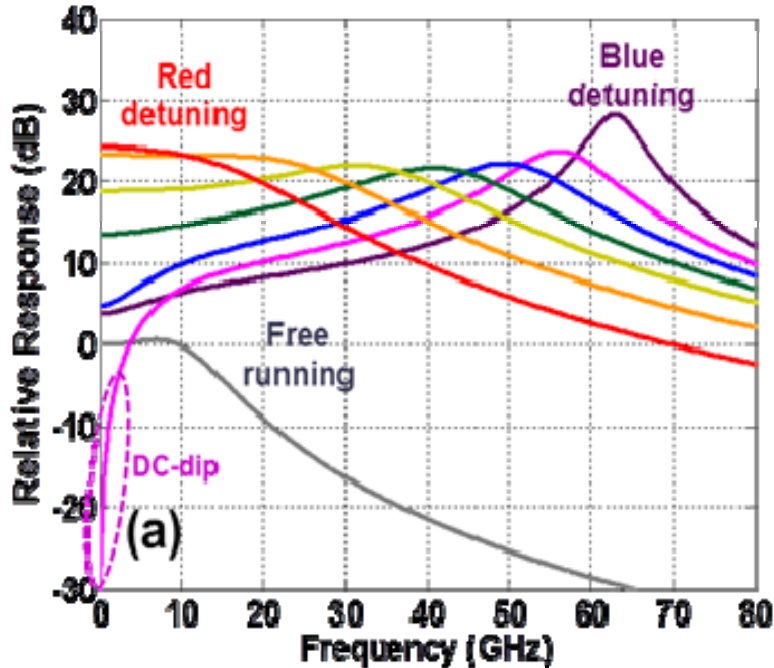


Figure 1.9 Relative magnitude response simulation for OIL-VCSEL small-signal frequency response curves for different detunings, compared with the free running case.[50]

To simulate large signal on-off keying (OOK) an ODE solver was used to simulate the data pattern. We then define extinction ratio $r_e = 10\log_{10}(P_{t1}/P_{t2})$, where P_{t1} and P_{t2} are the output powers corresponding to the high and low level of the modulation current, therefore negative extinction ratio indicates data pattern inversion. In Figure 1.11 we show the simulated 1 Gb/s data pattern for different detunings. Note that average total output power is decreasing with detuning as predicted by Figure 1.8. When detuning is increased, the data pattern changes from

normal to the transition state, and then to an inverted state. Figures 1.12 and 1.13 show the RF magnitude response and the extinction ratio of the data pattern on the same locking map. From the figure it is clear that the DC-suppression matches to the transition state, the condition where the extinction ratio is zero. The arrow on Figure 1.13 indicates the injection ratio condition for which the data pattern in Fig. 1.11 is simulated.

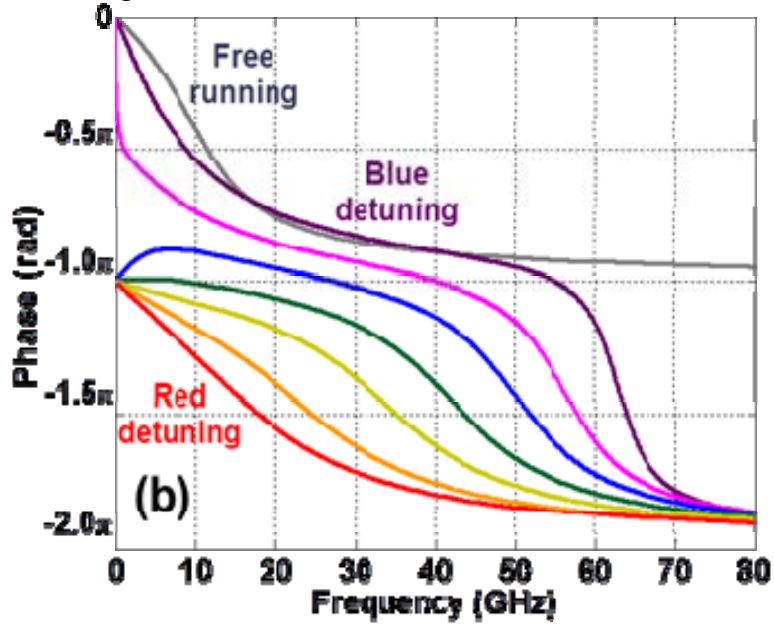


Figure 1.10 Phase response for OIL-VCSEL small-signal frequency response curves for different detunings, compared with the free running case. [50]

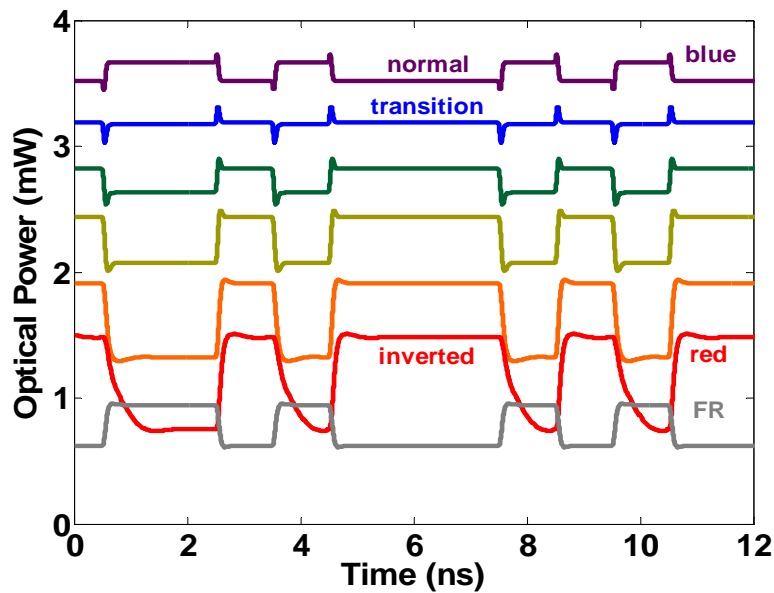


Figure 1.11 Simulation results for 1 Gb/s data pattern for different detunings. [50]

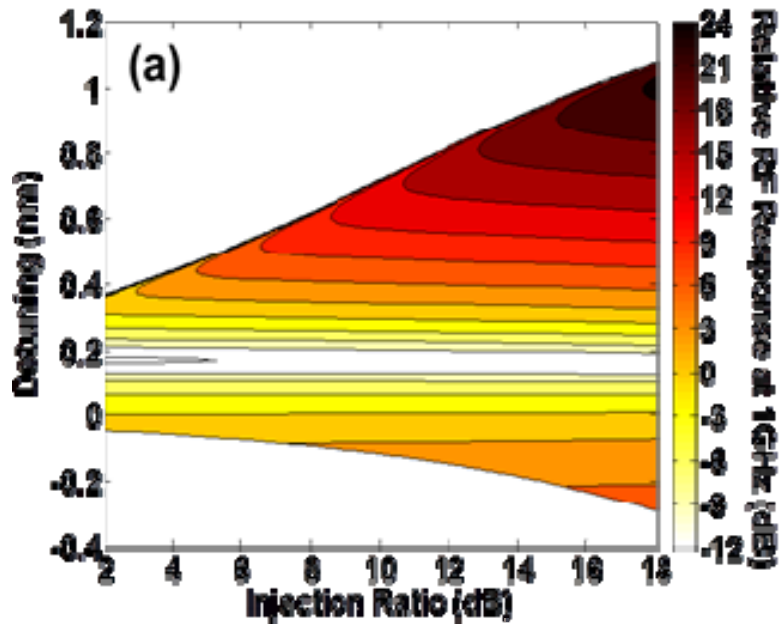


Figure 1.12 . Simulation results for the RF response of the small-signal analysis at 1 GHz of the 1 Gb/s OOK large-signal modulation on the same locking map. [50]

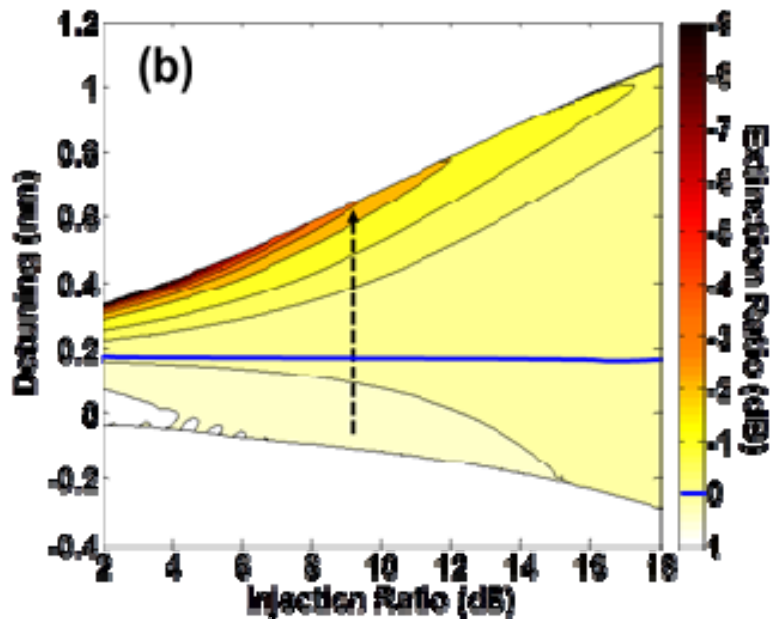


Figure 1.13 . Simulation results for the extinction ratio of the 1 Gb/s OOK large-signal modulation on the same locking map. The blue line indicates the conditions where $r_e=0$. [50]

1.3.4 Experiment

Verification of the simulations results was carried out using the experimental setup described in Section 1.3.1 with a network analyzer used for small-signal frequency response and wide-bandwidth oscilloscope to monitor the large signal data patterns. The VCSEL was biased at 4 mA with approximately 0.5 mW output power [52]. With a fixed injection ratio of 11 dB, both the frequency response of the OIL-VCSEL under small-signal modulation and the data pattern at 1 Gb/s OOK large-signal modulation were measured for different detunings, shown in Figures 1.14-1.16. The phase response was distorted above 24 GHz, due the low RF response for the free running VCSEL (Figure 1.15). For blue detunings, the damping was small and the data pattern was the same polarity compared with the free running case. Setting the detuning to 0.134 nm, a large DC-suppression was observed, corresponding to the transition state of the large-signal modulation. Further detuning to the red, the DC-suppression vanished, with a π phase shift and data pattern inversion. Continued detuning to the red resulted in higher RF gain at low frequencies.

Detuning and Injection ratio were then swept across the locking map with the VCSEL biased at 5 mA. The RF magnitude response and the extinction ratio of the 1 Gb/s OOK modulation was compared on the same locking map, as shown in Figures 1.17 and 1.18. Large-signal modulation locking range was smaller than the locking range of the small-signal modulation due to the larger perturbation of the large-signal modulation. The DC-suppression condition in Figure 1.17 and the transition state line in Figure 1.18 are in the same position on the locking map, indicating that they are the same condition but under different modulation strengths.

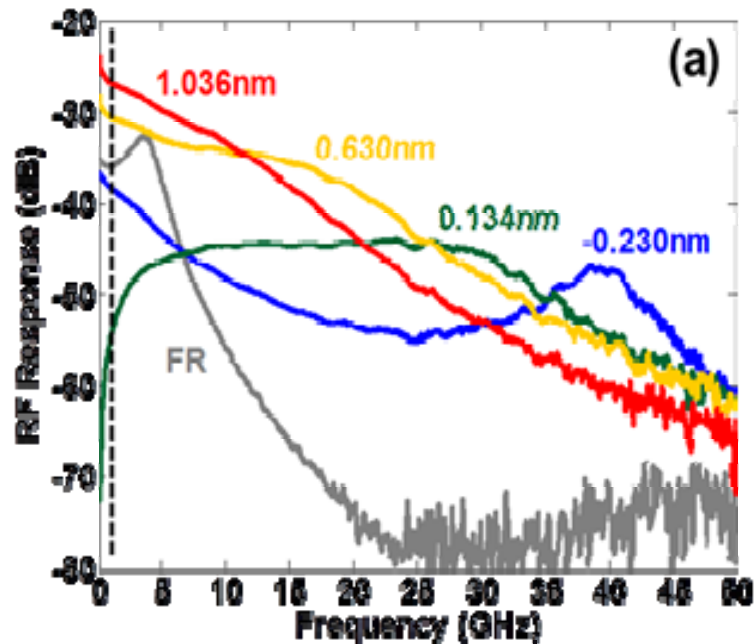


Figure 1.14 Magnitude RF response of the small-signal modulation of the OIL-VCSEL for different detunings (at a fixed injection ratio). [50]

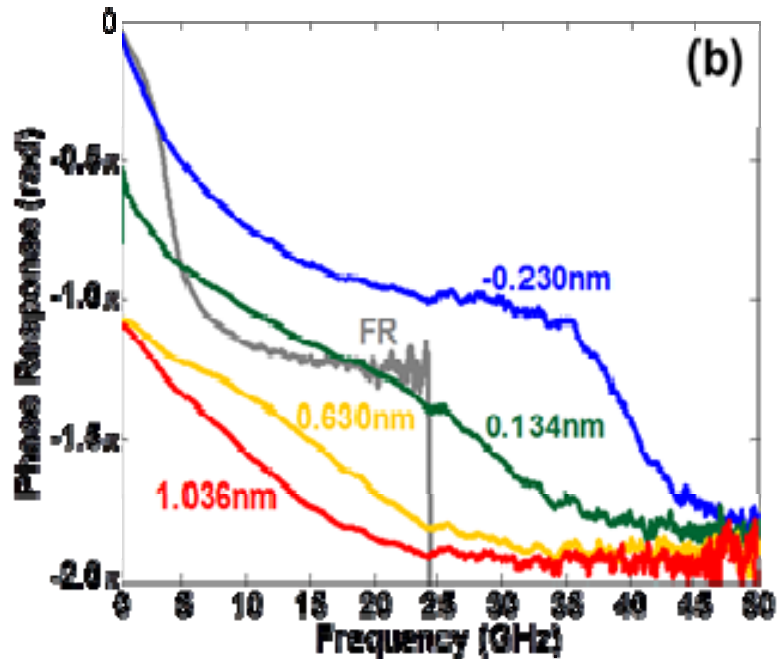


Figure 1.15 Phase RF response of the small-signal modulation of the OIL-VCSEL for different detunings (at a fixed injection ratio). [50]

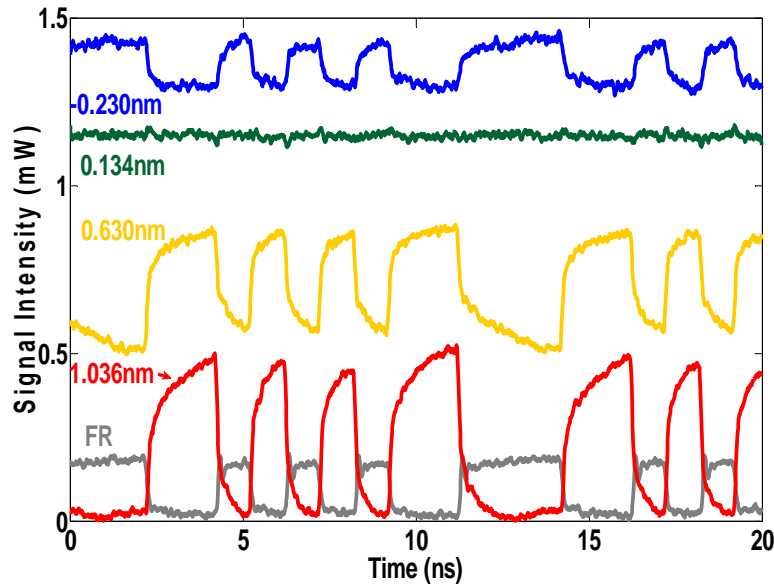


Figure 1.16 Simulation results for 1 Gb/s data pattern for different detunings. [50]

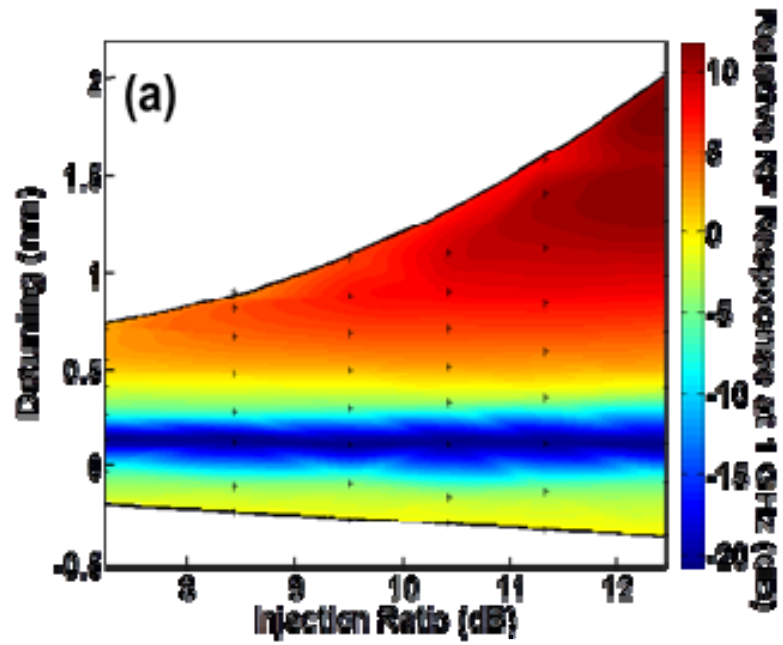


Figure 1.17 RF response of the small-signal modulation at 1 GHz [50]

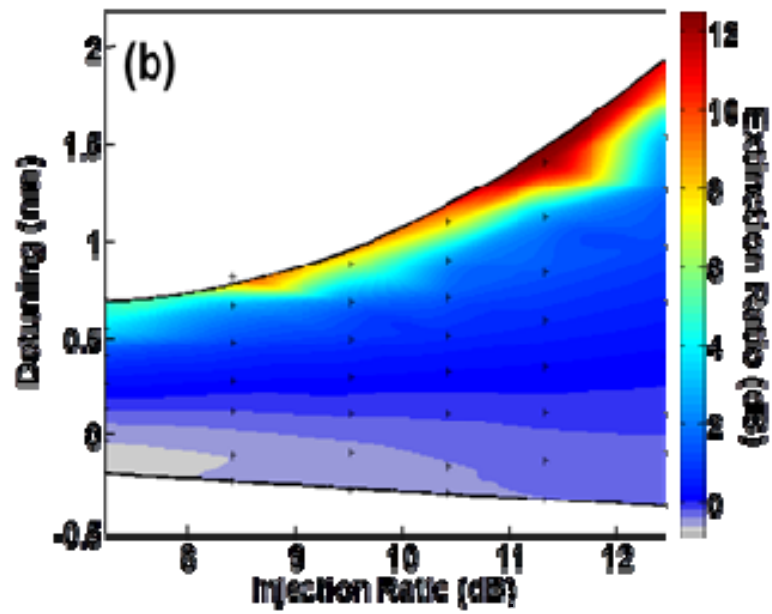


Figure 1.18 Extinction ratio of the 1 Gb/s OOK large-signal modulation on the locking map.[50]

1.4 Summary

In this chapter, we have described the history and theory of optical injection locking of semiconductor lasers. Over the years, optical injection locking has transformed from a laboratory physics experiment into a practical performance enhancer for telecommunications. Moreover, its underlying theory of operation has become more robust and provides more intuitive understanding of its performance enhancements.

Chapter 2 Analog Applications of Optically Injection Locked VCSELs

2.1 Motivation

Analog fiber optic communications have provided numerous benefits over the years from cable TV to cellular backhaul. However, performance limitations especially in bandwidth hamper its adoption in many other applications. Optical injection locking of VCSELs provides a solution for this by extending the usable bandwidth of a low cost optical transmitter as well as improving other figures of merits. In this chapter, the bandwidth extension as well as applications based on this phenomenon will be explored.

2.2 Resonance Frequency Enhancement

2.2.1 Single Transverse Mode VCSEL

Resonance frequency enhancement of directly modulated lasers is one of many enhancements that OIL has demonstrated, and it has been independently verified by numerous groups. Previous systematic studies have been done on 1.55- μm VCSELs in the ultra-high injection regime, showing resonance frequency enhancement into the millimeter-wave range. However, these experiments have been equipment-limited in their measurement technique. Therefore, a larger range of injection ratios and detuning were not explored. In the following section we extend this systematic study to show > 100 GHz resonance frequency and >80 GHz 3-dB bandwidth [45], [53].

The experimental setup is shown in Figure 1.3. An off-the-shelf commercial DFB laser is used for the master laser with a specified maximum output power of 40 mW. The slave laser is a buried tunnel junction (BTJ) 1550 nm single transverse mode VCSEL with a 3-dB bandwidth of over 10 GHz, threshold current of 0.6 mA and maximum output power of > 1 mW [52]. Temperature control of the VCSEL is provided via the control scheme described in Section

1.3.1. Output light from the VCSEL is coupled via a lensed fiber and then coupled to a circulator to allow for unidirectional injection locking. Polarization is matched between the master and slave laser using a polarization controller to achieve the maximum injected power. The VCSEL is biased and modulated through a 1-mm coaxial cable and bias tee connected to a 110 GHz mm-wave probe for on-chip measurements. To view the optical spectra a 99/1 coupler is placed after the circulator. For measurement a 110 GHz network analyzer is used to provide the test signal which is converted back to the electrical domain by a photodetector with a 3-dB bandwidth of 84 GHz and then processed by the network analyzer. Resonance frequency enhancement due to wavelength detuning was tested first by keeping the injection ratio constant and varying the wavelength of the master wavelength. Figure 2.1 shows the small-signal frequency response and Figure 2.2 shows the optical spectra of the VCSEL at various detuning values under a constant external light injection of 16 dB with the free-running response shown as a reference. The VCSEL was biased at 2 mA with 0.43 mW light output power and 6-GHz free running resonance frequency. The master laser was tuned across detuning values from -0.748 nm to -0.906 nm, resulting in the resonance frequency peak increasing from 92 GHz to 107 GHz, which is a record for directly modulated semiconductor lasers. However, this is not a device limitation but an instrumentation limitation still.

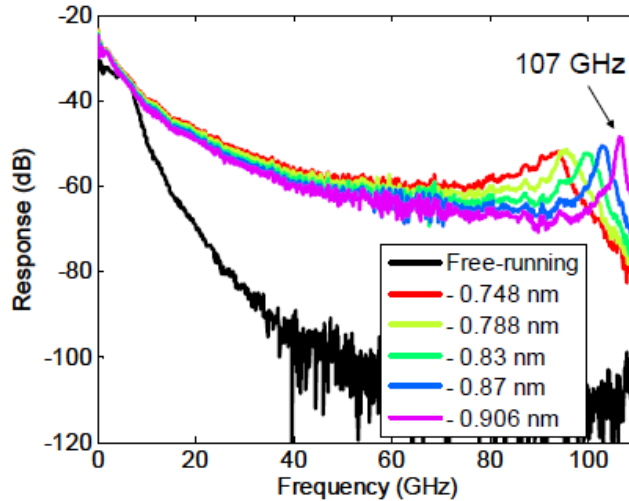


Figure 2.1 Frequency response of an OIL VCSEL at various detuning values. A record resonance frequency of 107 GHz is shown. [53]

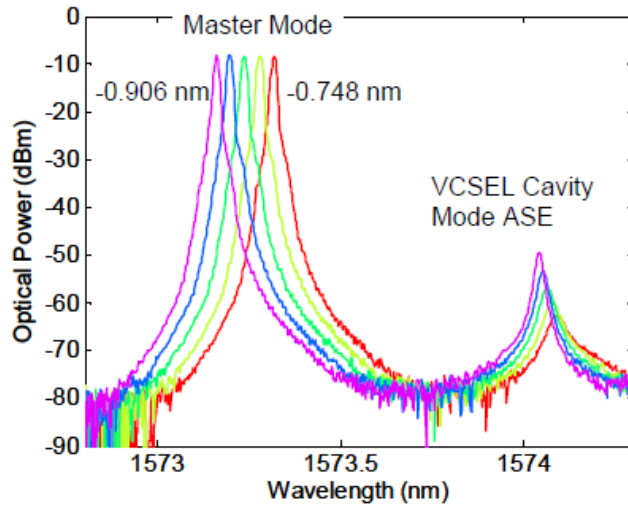


Figure 2.2 Optical spectra of an OIL VCSEL at various detuning values. [53]

Besides wavelength detuning, the resonance frequency enhancement can be obtained by varying the master laser power. Figure 2.3 shows the magnitude frequency response and optical spectra of the OIL VCSEL at different injection ratios, with the resonance frequency increasing with higher injection ratios. The corresponding optical spectra is shown in Figure 2.4. From these two parameters, it can be seen that increasing injection ratio and detuning to the blue will provide the highest resonance frequency enhancement.

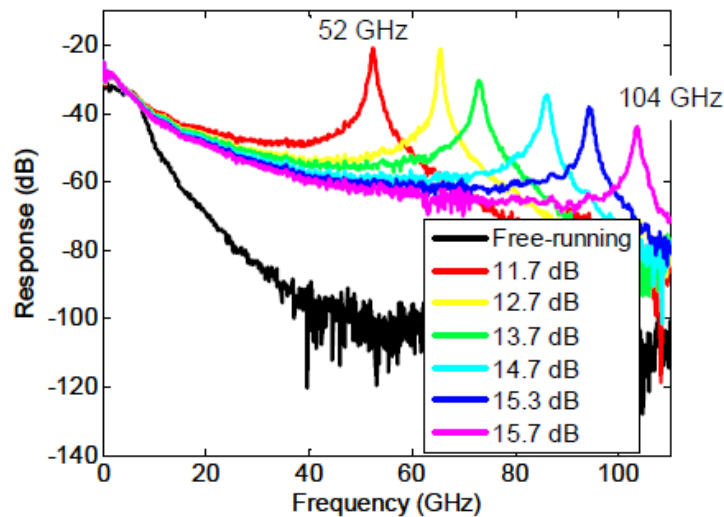


Figure 2.3 Frequency response of an OIL VCSEL under various injection ratio levels. The detuning is adjusted to result in a resonance peak with ~ 20 dB gain for all the cases. [53]

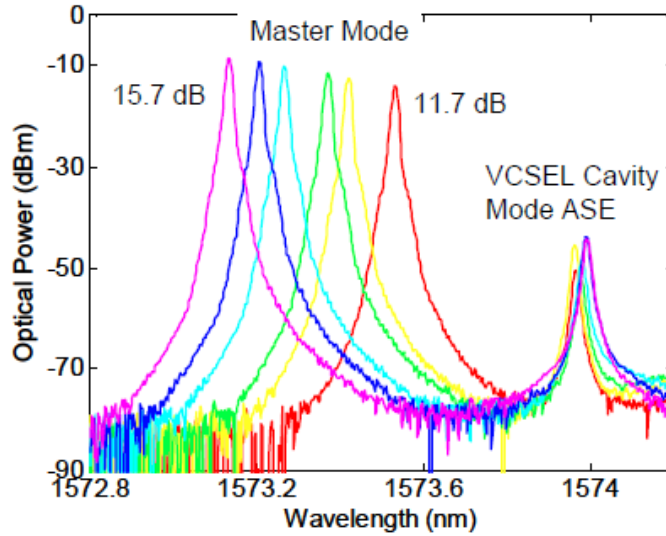


Figure 2.4 Optical spectra of an OIL VCSEL under various injection ratio levels. Both the power and the wavelength of the master laser are tuned. [53]

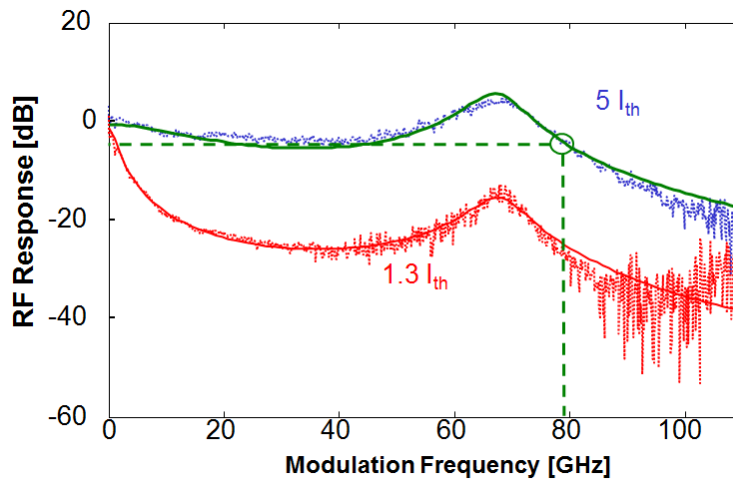


Figure 2.5 3-dB frequency response enhancement of an OIL VCSEL to 80 GHz. [53]

2.2.2 Multi-Transverse Mode VCSEL

Optical injection locking (OIL) of single-mode (SM) VCSELs has previously been demonstrated to improve both modulation speed and transmission distance [34], [39], [54]. 107 GHz resonance frequency and 80 GHz intrinsic 3-dB bandwidth for an OIL SM VCSEL has been experimentally demonstrated [53]. Injection locking of multi longitudinal-mode Fabry-Perot (FP) lasers has also been shown to increase the 3-dB bandwidth by a factor of 2 [55]. However, further improvement of multi longitudinal-mode FP lasers is limited by the spacing between the adjacent longitudinal modes, which limits the locking range thus the bandwidth of the frequency

response. Previous work has also studied MM VCSELs under weak optical injection showing higher-order mode suppression and polarization switching, however no frequency response enhancement was shown [56], [57].

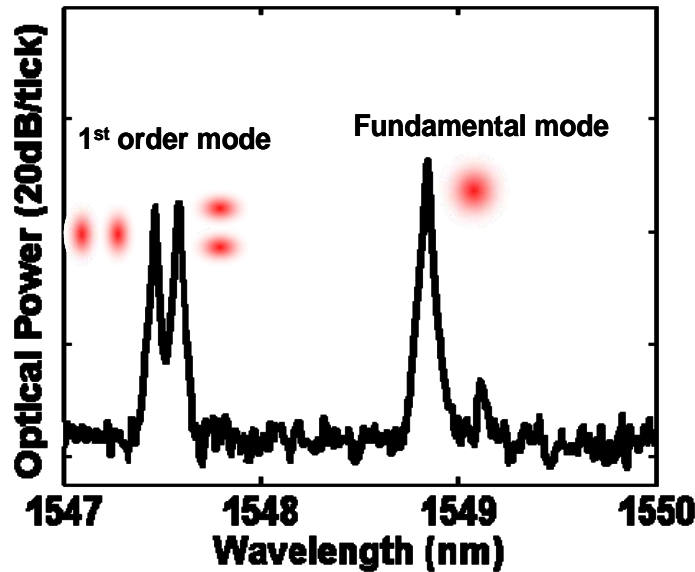


Figure 2.6 Optical spectra of 10 μm MM VCSEL. The transverse modes are spectrally and spatially distinct.[58]

In this section, we investigate optical injection locking of MM VCSELs to improve device performance under direct modulation. We show a 54 GHz resonance frequency and 38 GHz 3-dB bandwidth for an OIL MM VCSEL with a free running bandwidth of 3 GHz. Leveraging the spectrally and spatially well separated transverse modes of MM VCSELs (Figure 2.6) we also show a tailorable frequency response. We believe that this result can provide an excellent solution for low-cost upgrades of existing short-reach optical networks.

2.2.3 Resonance Frequency and 3-dB Bandwidth Enhancement

The experimental setup, Figure 2.7, is similar to previous single-mode optical injection locking experiments with the single-mode slave laser being replaced by a MM VCSEL. We use a commercial off-the-shelf CW DFB laser with a maximum output power of ~80 mW as the master laser. A MM VCSEL designed with a buried tunnel junction (BTJ) structure to confine both current and light is employed as the slave laser. The MM VCSEL has a 10 μm aperture, 6 mA lasing threshold and a maximum output power of ~ 5 mW at 25-mA bias [52]. Output of the MM VCSEL is coupled via a cleaved SM fiber with a coupling loss of ~ 5 dB. Through the optical circulator and polarization controller the master laser injection locks the slave laser. Modulation is then directly imposed on the MM VCSEL by means of a high-speed RF probe. The output of the circulator is split to an optical spectrum analyzer to record the optical spectra and to a photodetector so small-signal frequency response (Agilent E8361A) can be tested. To achieve high injection power ratio, $P_{\text{Master}}/P_{\text{Slave}}$, while still maintaining multimode behavior, the VCSEL was biased at 10 mA with 1.2 mW output power. As seen in Figure 2.6 (black trace), the

VCSEL emits a fundamental mode, the longer wavelength mode, and a first-order mode, which has degenerate polarization modes.

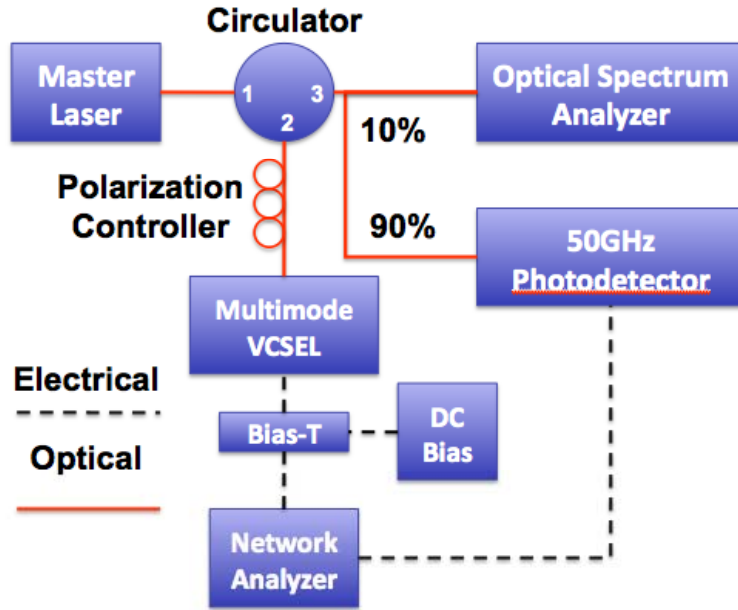


Figure 2.7 Schematic of MM OIL resonance frequency enhancement experimental setup

In the first experiment, we investigate resonance frequency enhancement of the MM VCSEL with respect to the free running case. As the fundamental mode has similar spatial characteristics to the injected light and a single dominant polarization mode, it is selected for this experiment. Similarly to the single-mode case, to get resonance frequency enhancement the master laser wavelength is shorter than the slave laser wavelength ($\Delta\lambda = \lambda_{\text{Master}} - \lambda_{\text{Slave}}$ is negative). Figure 2.8 shows the optical spectra for various detuning values when the master laser is detuned to wavelengths shorter than the slave laser wavelength while the injection power ratio (~ 8.1 dB) is held constant. The higher-order mode is suppressed under strong optical injection locking, effectively making it a single-mode laser. The side mode suppression ratio are 49.4, 37.2, 28.1, and 24.4 dB, for -0.245, -0.293, -0.341, and -0.365 nm detuning values, respectively. Figure 2.9 shows the resulting small signal modulation responses. The resonance frequency enhancement is significant comparing to the free running (black trace) case MM-VCSEL. Note that the data shown in Fig. 2b include the VCSEL device parasitics (estimated to be 10 GHz), and the measurement system parasitics such as the electric probe (40 GHz), photo-detector (50 GHz) and the bias tee (50 GHz). The ripples in the frequency response are caused by reflections off of the cleaved fiber, and can be reduced by switching to a lensed fiber. The 54 GHz resonance frequency is a record value achieved for directly modulated MM VCSEL, to the best of our knowledge.

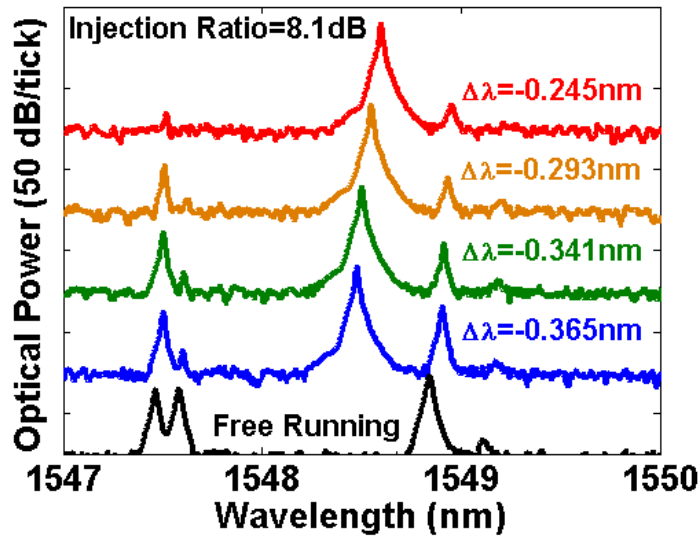


Figure 2.8 Optical spectra of 10 um 1550-nm multimode VCSEL under optical injection with constant injection ratio (~ 8.1 dB) and negative detuning. [58]

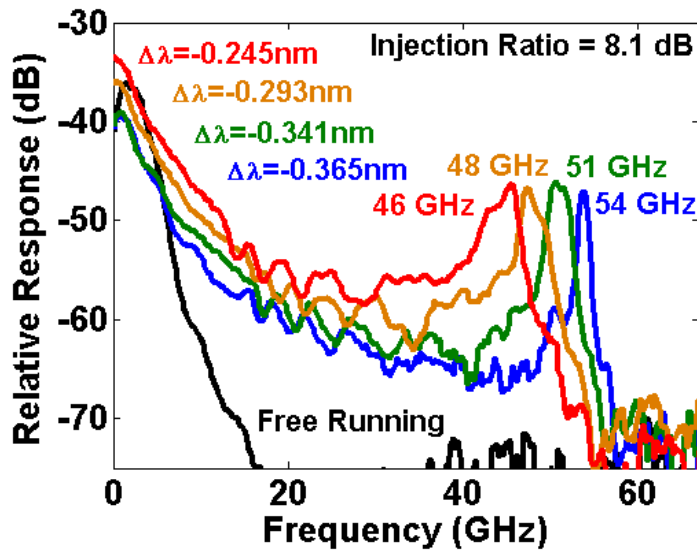


Figure 2.9 Frequency response of 10 um 1550-nm multimode VCSEL under optical injection with constant injection ratio (~ 8.1 dB) and negative detuning. [58]

For the case when the master laser wavelength is detuned to a longer wavelength ($\Delta\lambda$ is positive) than the slave laser fundamental mode, a flat frequency response can be achieved with a large 3-dB bandwidth enhancement. Figure 2.10 shows the optical spectra for such cases. The injection power is again held constant (9.03 dB) and the master laser is detuned to longer wavelengths than the slave laser. The higher order mode is suppressed in this case also with a

side mode suppression ratios of >70dB for detuning values of 0.208, 0.582, and 0.778nm. Corresponding frequency responses are shown in Figure 2.11, with a record 38 GHz 3-dB bandwidth at $\Delta\lambda = 0.21\text{nm}$. Note again that the data shown in Figure 2.11 includes the system parasitics and has rippling due to the cleaved fiber similarly to Fig. 2.9.

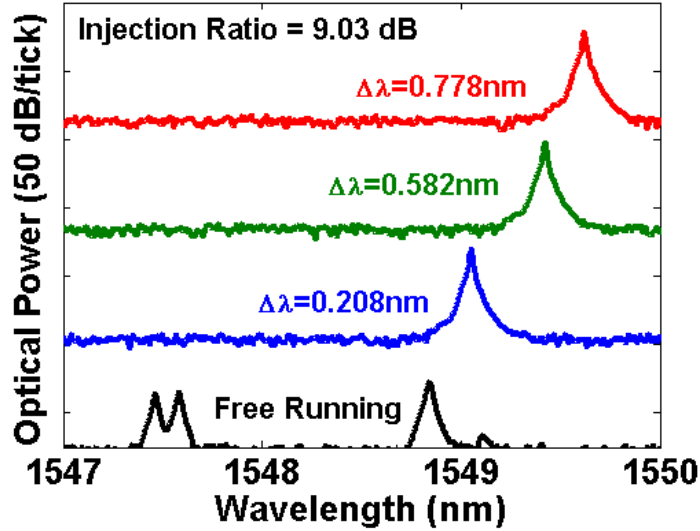


Figure 2.10 Optical spectra of 10 μm 1550-nm multimode VCSEL under optical injection with constant injection ratio (~9.03 dB) and positive detuning. Black trace is free running MM VCSEL. [58]

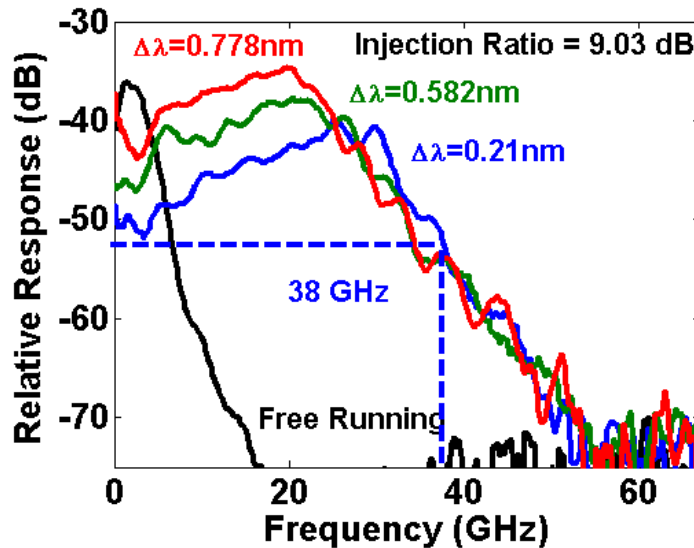


Figure 2.11 Frequency response of 10 μm 1550-nm multimode VCSEL under optical injection with constant injection ratio (~9.03 dB) and positive detuning. Black trace is free running MM VCSEL. [58]

2.2.4 Spatial Detuning

In the previous section we explored optically injection locking the fundamental mode due to its spatial mode profile being similar to the single-mode case. In this section we investigate injection locking of higher order transverse modes and spatial detuning to preferentially select modes. A 15 μm aperture MM VCSEL biased at 12 mA with 1 mW output power and a lensed SM fiber are used for this experiment to provide a highly multimode slave laser and to provide better selective coupling respectively. Additionally, the master laser was replaced with an external cavity tunable laser with an erbium-doped fiber amplifier (EDFA) to achieve high injection ratios due to the large coupling loss. In Figure 2.12 we see the optical spectra for the MM VCSEL where output coupling is optimized (~ 12 dB coupling loss). The first order mode is the dominant mode in this case. Optically injection locking to achieve resonant frequency enhancement on this mode results in a double peaked frequency response due to the degeneracy of the polarization modes (Figure 2.13).

Spatially scanning the lensed fiber across the aperture of the VCSEL to make the fundamental mode the dominant mode, results in the data shown in Figure 2.14 (black trace). Optically injection locking the dominant (fundamental) mode now results in the single peak resonance frequency enhancement. 30 GHz resonance frequency is achieved at a detuning of -0.136nm with 40 dB higher-order mode suppression (Figure 2.14). This result shows that performance enhancement is possible by spatially selecting preferable spectral characteristics of the MM VCSEL

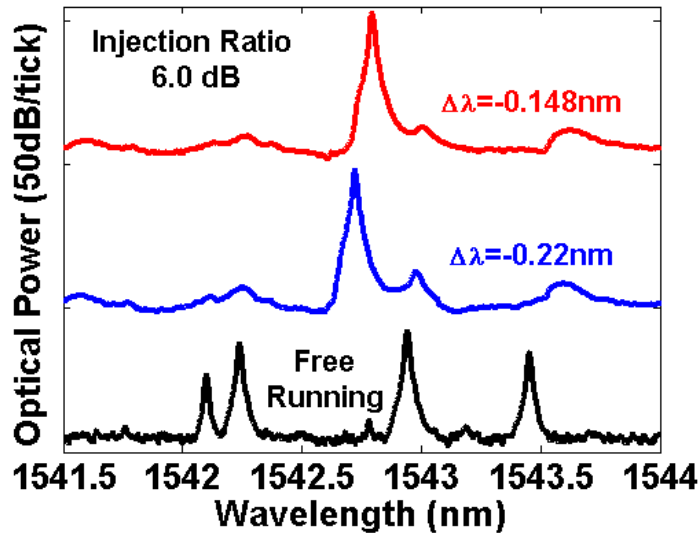


Figure 2.12 Optical spectra of 15um 1550-nm multimode VCSEL under optical injection with constant injection ratio (~ 6 dB) and negative detuning with 1st order mode selected as the dominant mode. [58]

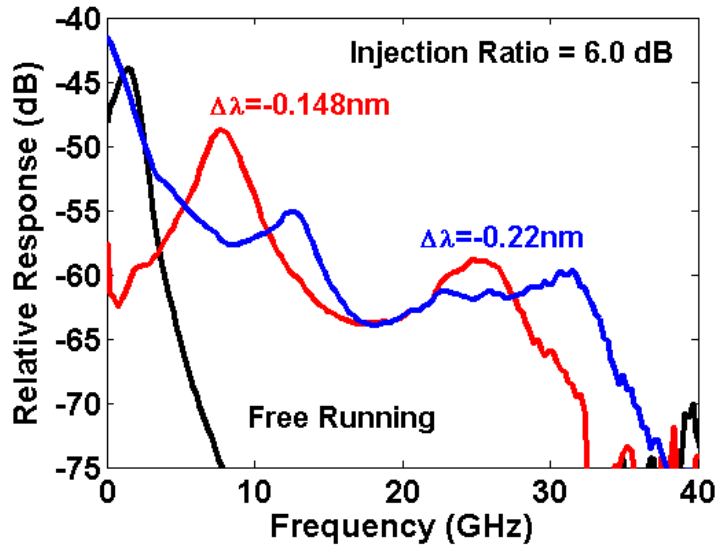


Figure 2.13 Frequency response of 15µm 1550-nm multimode VCSEL under optical injection with constant injection ratio (~6 dB) and negative detuning with 1st order mode selected as the dominant mode. Dual peak in frequency response is due to dual polarization modes of the 1st order mode. Black trace is the free running MM VCSEL. [58]

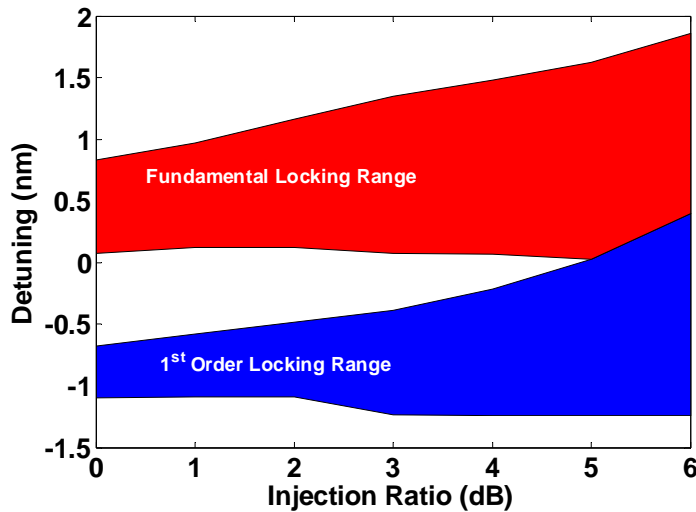


Figure 2.14 Locking range for MM VCSEL with two transverse modes, optimized for locking on fundamental mode. [58]

Figure 2.14 plots the experimental locking range of the multimode VCSEL across different detunings and injection ratios. Two distinct locking regions can be seen (red and blue) corresponding to the two transverse modes. Asymmetry of the locking range with respect to the original mode can be seen and attributed to the linewidth enhancement factor of the VCSEL.

2.2.5 Resonance Frequency Enhancement in Large Aperture VCSELs

In this section, we investigate optical injection locking of large ($> 15 \mu\text{m}$) aperture devices using a single mode CW master laser. Optical injection locking of a $20 \mu\text{m}$ aperture device shows a 7X improvement in 3-dB bandwidth and resonance frequency, while for a $30 \mu\text{m}$ aperture VCSEL we achieved 30 GHz 3-dB bandwidth and 28 GHz resonance frequency enhancement from a free running 3-dB bandwidth of 2 GHz. We believe this result will allow high power extremely large aperture OIL VCSELs to be used in FTTx and metro networks.

The experimental setup is shown in Figure 1.3. An 80 mW commercial DFB laser is used as the master laser. Buried tunnel junction 1550 nm VCSELs with aperture sizes of 20 and $30 \mu\text{m}$ are used as the slave laser. The $20 \mu\text{m}$ aperture VCSEL has a threshold of 40 mA and $>1 \text{ mW}$ output power at 45mA, while the $30 \mu\text{m}$ aperture VCSEL has a threshold of 55 mA and output power of $>5\text{mW}$ at 60 mA. Light emission is coupled into a single mode lensed fiber with a $5 \mu\text{m}$ spot size with $\sim 12 \text{ dB}$ coupling loss for the $20 \mu\text{m}$ and $\sim 16 \text{ dB}$ for the $30 \mu\text{m}$. The VCSEL is optically injection-locked by the master through a circulator and polarization controller. Modulation is then directly applied to the VCSEL by an RF probe (65 GHz) and small-signal frequency response is measured using an Agilent E8361A.

In the first experiment the $20 \mu\text{m}$ VCSEL is biased at 45 mA where it exhibits a 3-dB bandwidth of 2 GHz and a multimode spectra Figures 2.15 and 2.16 (black trace). Optically injection locking the VCSEL we obtain a flat response with 3-dB bandwidth of 15 GHz when the master laser is detuned -0.59 nm from the slave laser (Figures 2.15 and 2.16 (red curve)). An enhanced resonance frequency of 12 GHz is obtained at a detuning of 0.41 nm (Figures 2.15 and 2.16 (blue curve)). Side mode suppression ratios of 57.45 dB and 65.65 dB were achieved respectively. Further enhancement was not seen due to device failure. Also note the data is raw data including VCSEL RC parasitic and measurement system parasitics.

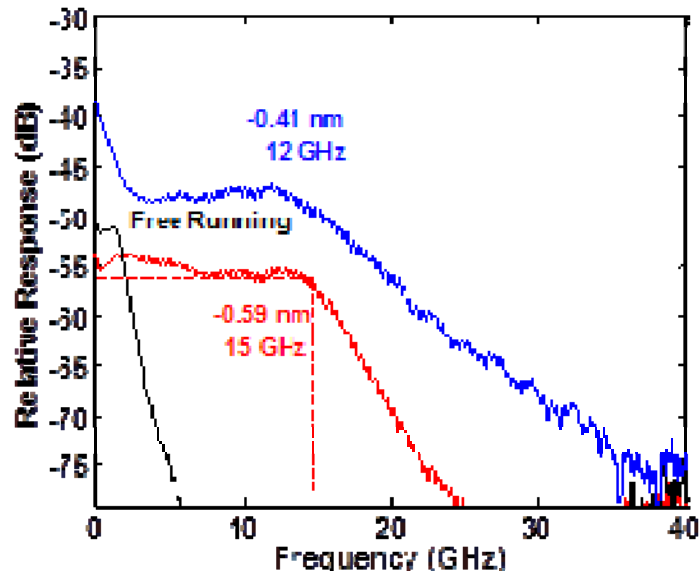


Figure 2.15 Small-signal frequency response for a $20 \mu\text{m}$ aperture VCSEL. Resonance frequency increases from 2 GHz up to 12 GHz and 3-dB bandwidth of 15 GHz is obtained.

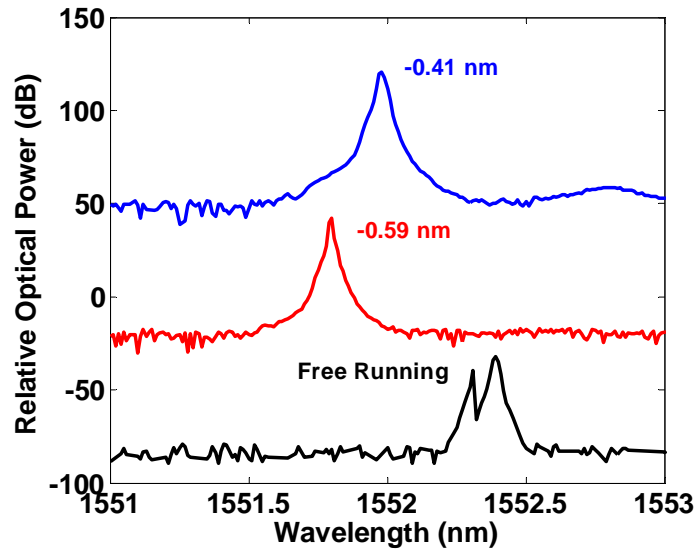


Figure 2.16 Optical spectra for 20 μm aperture VCSEL. OIL occurs on the fundamental mode. The higher-order transverse modes and spontaneous emission are suppressed under external light injection

Figures 2.17 and 2.18 show the small signal frequency response and optical spectra of the OIL 30 μm aperture VCSEL. The free running laser behaves similarly to a single mode laser, likely due to the higher order transverse modes not lying within the spot of the lensed fiber. Optically injection locking at -0.19 and -0.22 nm at an injection ratio of 0.8 dB we see the characteristic resonance frequency enhancements to 20 and 28 GHz with optical side mode suppression ratios of 52.8 and 53.87 dB respectively. At a detuning of -0.06 nm and injection ratio of 0.8 dB a 3-dB bandwidth of 30 GHz is achieved with a side mode suppression ratio of 53.41 dB.

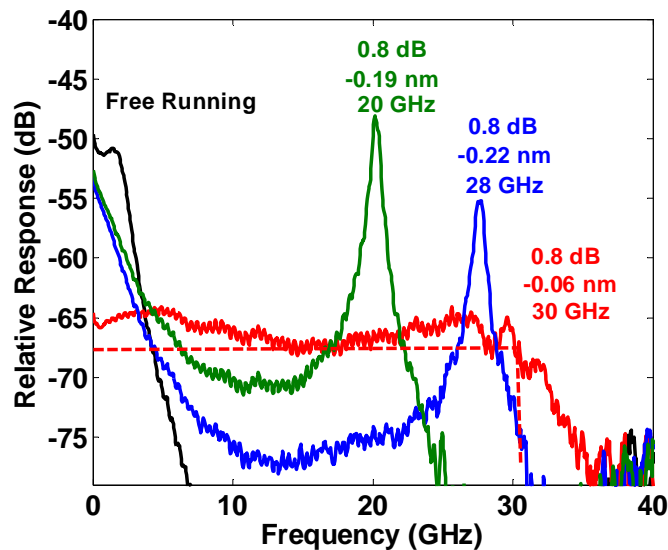


Figure 2.17 Small-signal frequency response for 30 μm aperture VCSEL. Resonance frequency increases from 2 GHz up to 28 GHz and 3-dB bandwidth of 30 GHz is obtained.

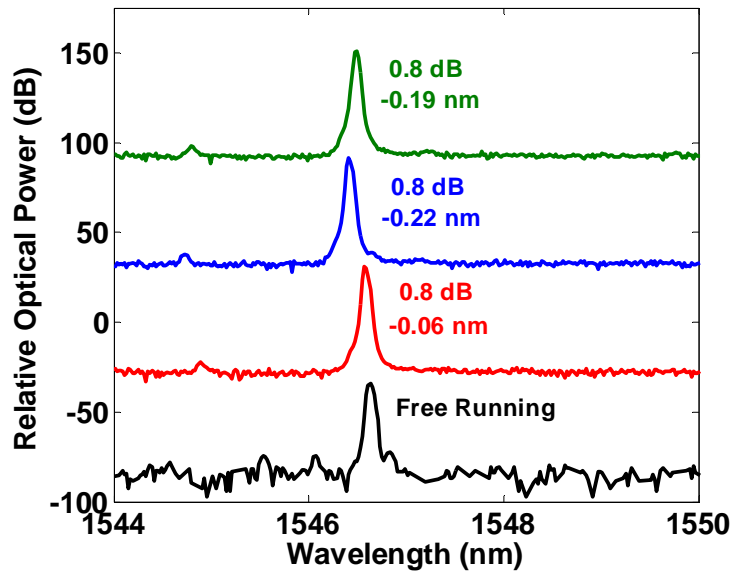


Figure 2.18 Optical spectra for 30 μm aperture VCSEL. OIL occurs on the fundamental mode. The higher-order transverse modes and spontaneous emission are suppressed under external light injection.

2.2.6 Locking Range of Multimode VCSELs

The experimental setup consists of a commercial CW DFB laser (master) with $\sim 80\text{mW}$ maximum output power and a 1550nm buried tunnel junction MM VCSEL (slave) with a 15- μm aperture size. The lasing threshold of the MM VCSEL is 10 mA and maximum output power is $\sim 6\text{ mW}$ at bias of 35 mA. Master light is injected into the MM VCSEL by means of a 3-port circulator with port 2 coupled to a polarization controller to maximize injection ratio and then coupled to the VCSEL by a lensed fiber with 12-dB coupling loss (optimized). The output of port 3 of the circulator is then split 90/10 to a photodetector and optical spectrum analyzer, respectively. Modulation is directly applied onto the VCSEL via a high-speed probe (40 GHz). Small-signal frequency response is tested using Agilent E8361A network analyzer

In this experiment, the VCSEL is biased at 14 mA ($1.4 \times I_{\text{th}}$) with $\sim 1\text{mW}$ output power to maximize injection power ratio, $P_{\text{Master}} / P_{\text{Slave}}$, while still maintaining multimode behavior. At this bias the VCSEL emits three distinct transverse modes separated by $\sim 0.8\text{nm}$ (Figure 2.19 black trace). The 2nd order (shortest wavelength) mode is the dominant mode, followed by the 1st order mode and the fundamental (longest wavelength) mode. When optically injection locked, each of the three modes has a distinct locking range with unlocked regimes between the modes. Injection locking is first applied to the 2nd order mode, with an injection ratio of -2.97 dB (Figure 2.19 blue trace). As the master is tuned towards the longer wavelength the 2nd order mode becomes unlocked when detuning ($\Delta\lambda = \lambda_{\text{Master}} - \lambda_{\text{Slave}(\text{fundamental})}$) $\Delta\lambda = -1.436\text{ nm}$ until the master is detuned near the 1st order mode ($\Delta\lambda = -1.018\text{ nm}$) and becomes locked again (Figure 2.19). Detuning the master to even higher wavelengths causes the laser to unlock again ($\Delta\lambda = -0.368\text{nm}$) and then relocks onto the fundamental mode ($\Delta\lambda = -0.05\text{ nm}$). In these three distinct locking regions we see improved frequency response, i.e. enhanced resonance frequency.

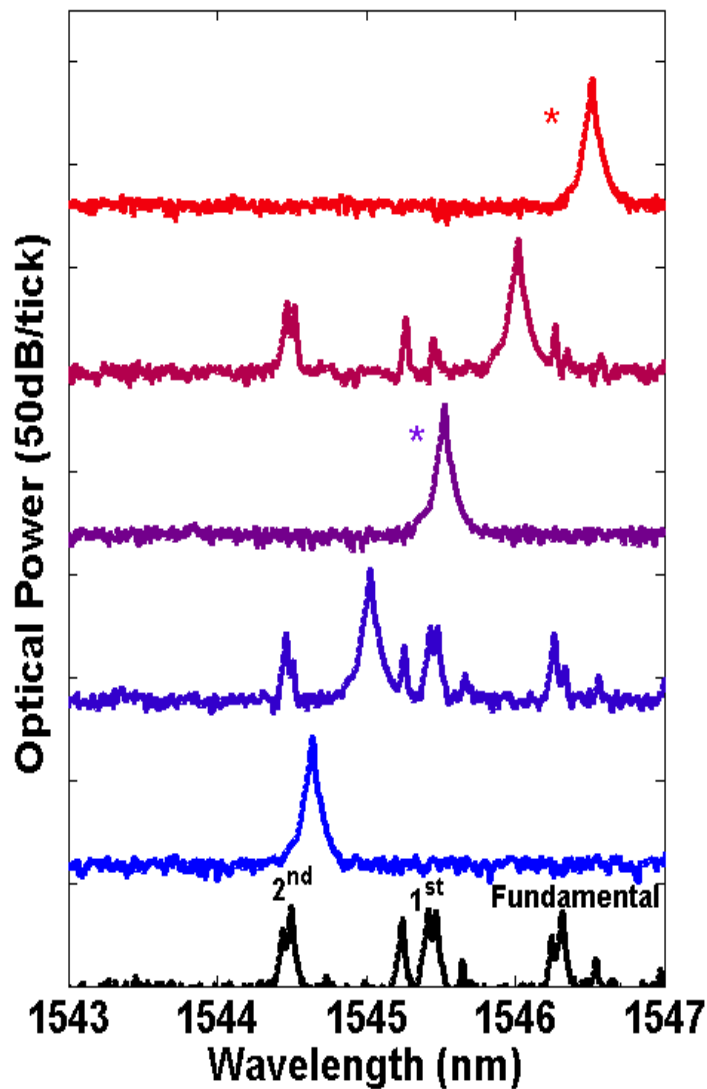


Figure 2.19 Optical spectra of MM VCSEL under optical injection at various detunings showing different locking regions of each transverse mode. Black trace is free running MM VCSEL[59]

2.2.7 Conclusion

Record resonance frequency and 3-dB bandwidth enhancement are shown for a directly modulated multimode 1550-nm VCSEL under optical injection locking. Spectral detuning for transverse mode selection was also shown to improve performance and provide tenability of frequency response. Results are limited only by system parasitics and maximum master laser output power, which if alleviated will result in performance similar to a single-mode OIL VCSEL. Furthermore, this technique will also improve performance for 850 nm and 980 nm MM VCSELs.

2.1 Millimeter-Wave Radio over Fiber Transmission

2.1.1 Motivation

As the demand for high-data rate wireless applications increases (HDTV, Wireless HD, etc.), the bandwidth of distribution networks needs to keep pace with their explosive growth. Millimeter-wave (mm-wave) wireless communications have attracted interest to solve this problem due to 7-GHz of unlicensed spectrum (57-64 GHz) in this band, but high atmospheric loss limits its propagation to very short distances. To extend the reach at these mm-wave frequencies, Radio-over-fiber (RoF) has been proposed as a promising solution due to optical fiber's extremely large bandwidth and low transmission loss.

Various schemes have been demonstrated for 60 GHz RoF using external modulators with double sideband (DSB) modulation. However, most modulators have bandwidths of less than 40 GHz and require frequency multiplication to achieve 60 GHz and beyond [60–62]. Secondly, the DSB modulation scheme suffers from dispersion-induced fading as the two sidebands walk off from each other in phase. Furthermore, the DSB dispersion precludes advanced modulation formats from being used, limiting transmission to spectrally inefficient ASK [63].

In this section, we demonstrate the efficacy of a directly modulated optically injection locked (OIL) VCSEL as a 60 GHz RoF transmitter. By using an OIL VCSEL the transmitter can be greatly simplified, as OIL VCSELs have been shown to support frequencies up to 107 GHz. Moreover, since modulation of an OIL VCSEL is inherently single sideband (SSB), the effects of dispersion-induced fading are greatly reduced. These features allow us to demonstrate transmission of 4 Gbps amplitude shift key (ASK) modulated data and 2 Gbps quadrature phase shift key (QPSK) subcarrier modulated data at 60 GHz over 20 km of standard single transverse mode fiber (SSMF) followed by 3 m of wireless transmission.

2.1.2 Optical Injection Locking for RoF

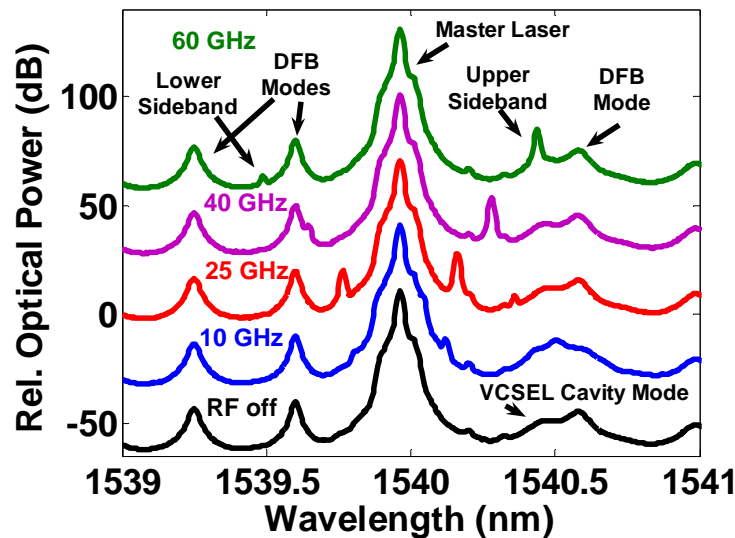


Figure 2.20 Optical spectra of OIL VCSEL with single RF tone applied at different frequencies. Single sideband behavior is seen as frequency approaches cavity mode.

Injecting the output of a continuous-wave (CW) master laser into a slave VCSEL (biased above threshold) locks the VCSEL wavelength to the master wavelength and red-shifts the VCSEL cavity mode. Using this phenomenon we have previously demonstrated enhanced resonance frequency (107 GHz) and intrinsic 3-dB bandwidth (80 GHz). Additionally, we have shown reduced chirp and extended transmission distance with OIL VCSELs.

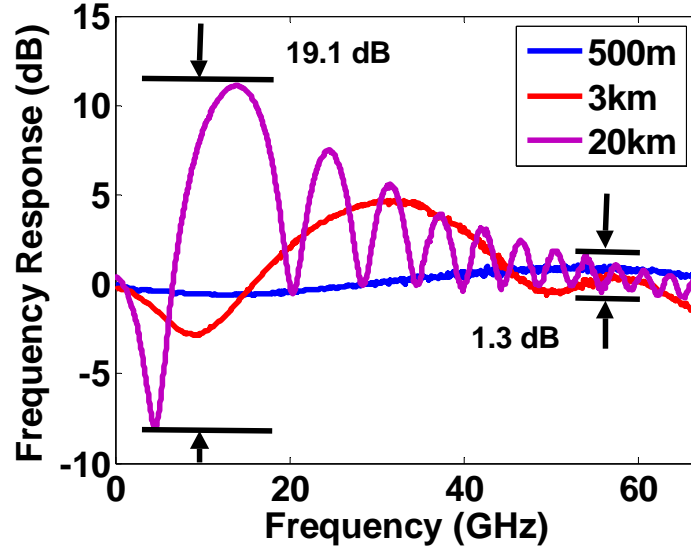


Figure 2.21 Frequency response of different fiber lengths measured with the OIL VCSEL transmitter ($f_R=64$ GHz). Amplitude fluctuations lessen at 60 GHz, indicating less dispersion-induced fading for SSB modulation

The key to these results is that under modulation an optically injection locked VCSEL, only amplifies the upper modulation sideband since the VCSEL cavity mode is red-shifted, while the lower sideband is attenuated making the VCSEL a SSB transmitter [64]. Figure 2.20 illustrates this in the optical domain. As the frequency of the single RF tone modulation of the OIL VCSEL is increased the upper modulation sideband to lower sideband optical power ratio increases from 7.75 dB at 25 GHz to 21.36 dB at 60 GHz. Large chirping of the cavity mode is also only observed for modulation below 10 GHz, indicating that the system is no longer limited by the dynamics of the free running VCSEL. To confirm this SSB behavior, we also performed the fiber-transfer-function-method (FTFM) to measure fiber dispersion [65]. In Figure 2.21, the OIL VCSEL small-signal frequency response after propagation across different fiber lengths is shown normalized to the back-to-back (B2B) frequency response. Fiber launch power is kept constant for all distances to 5.4 dBm. At low frequencies a large amplitude swing of 19.1 dB after 20 km of SSMF propagation is seen as the two modulation sidebands disperse in phase and interfere with each other. As the modulation frequency approaches the offset frequency of the VCSEL cavity mode, the amplitude fluctuation reduces to 1.3 dB after 20 km of SSMF propagation, indicating less dispersion impairment and that the OIL VCSEL has transitioned to being a SSB transmitter in agreement with the optical spectra data. Based on the spacing of the amplitude dips, the chirp factor (αH) was calculated to be 3.08 with a fiber dispersion of 16.69 ps/nm*km. Positive frequency response at lower frequencies is due to frequency to intensity modulation (FM-IM) conversion of the chirp of the OIL VCSEL over the dispersive fiber [66].

2.1.3 60 GHz RoF without Master Laser Suppression

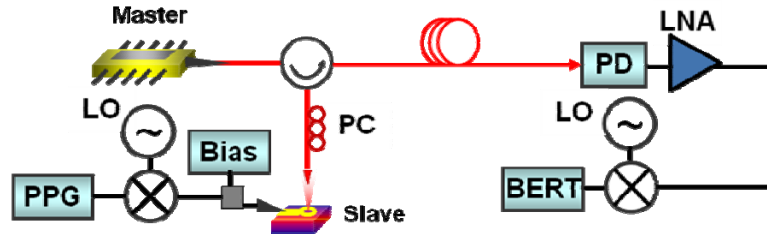


Figure 2.22 Experimental setup of OIL VCSEL RoF transmission system

Figure 2.22 shows a schematic of the experimental setup. A 60 GHz electronic local oscillator (LO) is mixed with a baseband signal generated by a pulse pattern generator (PPG) and then connected via bias-T to the VCSEL. The VCSEL is a 1540 nm single transverse mode buried tunnel junction (BTJ) VCSEL with maximum output power of ~ 3 mW and $\sim 70\%$ coupling efficiency to lensed fiber, acts as the slave laser. A high power CW distributed feedback master laser then injects into the VCSEL via a circulator. A polarization controller (PC) is used to maximize injection ratio efficiency by matching the master laser polarization to that of the slave VCSEL. The output of the circulator is then sent over various lengths of SSMF. A 70 GHz photodiode is then used to detect the signal and then amplified by a low noise amplifier and sent to a mixer with the same LO signal for downconversion. Following, downconversion the baseband signal is sent to a bit error rate tester (BERT).

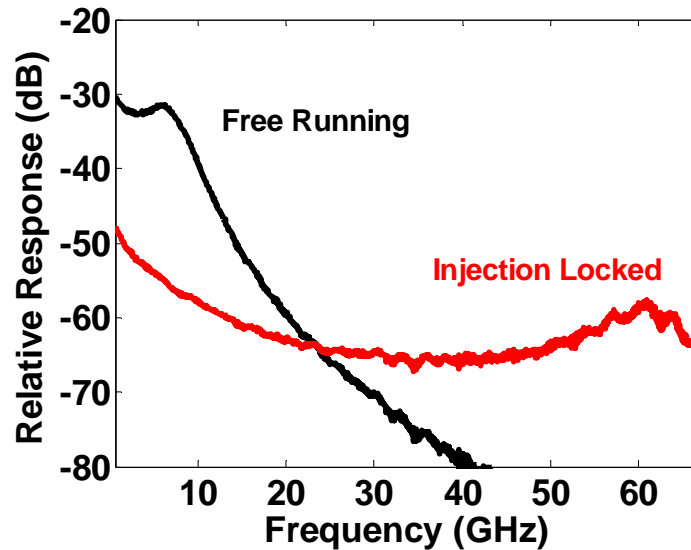


Figure 2.23 Small-signal frequency response with resonance frequency at 60 GHz after injection locking. Free running VCSEL response shown for comparison

By adjusting the injection ratio ($R=P_{\text{Master}}/P_{\text{Slave}}$) and wavelength detuning ($\Delta\lambda=\lambda_{\text{Master}}-\lambda_{\text{Slave}}$), a wide bandwidth mm-wave transmitter can be created with the desired frequency response. VCSEL bias was set to at 4.7 mA with ~ 1 mW output power and the master laser was biased at 218.9 mA with output power of 40.7 mW. In this case, we have negatively detuned the master laser with respect to the VCSEL to optimize the resonance frequency for 61 GHz and to use the slope of the resonance to compensate electrical losses and nonlinearities. Operating near resonance is typically associated with high relative intensity noise (RIN) for directly modulated lasers; however, since this VCSEL is injection locked the RIN is suppressed even at resonance. Figure 2.23 shows the small-signal frequency response for the free running VCSEL and for the OIL VCSEL. The free running VCSEL has a bandwidth of 8 GHz while the OIL VCSEL has response at mm-wave frequencies with 3-dB bandwidth of 8 GHz centered at 61 GHz. However, there is a 25 dB drop in resonance frequency peak response requiring higher gain electrical amplifiers at the receiver.

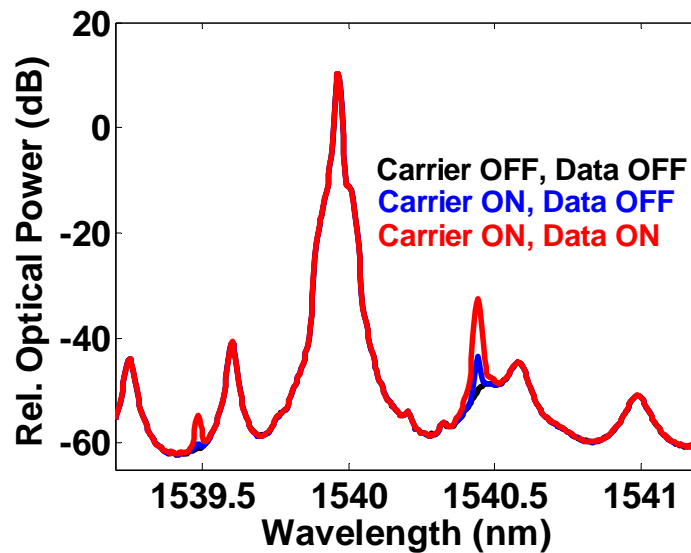


Figure 2.24 Optical spectra of OIL VCSEL ROF link without modulation (black), with 60 GHz carrier (blue), and with 60 GHz carrier and ASK modulation.

In Figure 2.24, the optical spectra are shown for the OIL VCSEL with the 60 GHz carrier and ASK data in various states. For the OIL case with no modulation, the optical carrier (master laser mode) to upper sideband power, in this case cavity mode suppression ratio (CSR) is 58.85 dB. With the LO carrier on the CSR ratio improves to 53.7 dB, and improves to 42.71 dB once the ASK modulation is added. This large ratio between the modes contributes to poor modulation efficiency requiring high fiber launch powers to achieve reasonable response amplitude or extinction ratio for digital data. The CSR for the lower sideband were 70.31 dB for carrier on without data and 64.92 dB for carrier and data both on, again confirming the SSB nature of the OIL VCSEL system.

Baseband ASK modulation was tested at a bit rate of 2 Gb/s with pseudo-random bit sequence (PRBS) of length $2^{31}-1$. This data was directly modulated onto the VCSEL after mixing with a 60.5 GHz carrier. Fiber launch power was set to 9.5 dBm, to maximize response

and achieve partially open eyes of the 60 GHz signal, due to the large CSR. Bit error rate versus received optical power curves for propagation over 0.5, and 1 km of SSMF are shown in Figure 2.25. For the 500 m and 1 km case we observe slight improvement in the bit error rate compared to the B2B case at the same received power before flooring occurs at $BER < 10^{-8}$. This floor is a result of the poor extinction ratio caused by the high CSR thus requiring high fiber launch powers limiting its usefulness for practical systems.

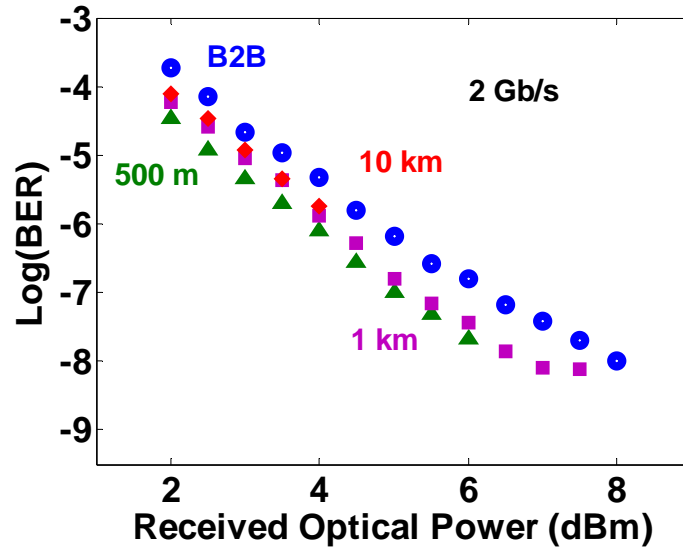


Figure 2.25 BER curves for 2 Gb/s ASK baseband modulation of 60 GHz OIL VCSEL RoF link for B2B, 500 m and 1 km fiber.

2.1.4 60 GHz RoF with Master Laser Suppression

To alleviate the small extinction ratio, we modified the experimental setup (Figure 2.26) to suppress the master laser mode. This was accomplished by using narrow bandwidth optical filters after the circulator adjusted so the master was attenuated and the cavity mode and 60 GHz carrier were located in the passband. Another EDFA was also added to compensate for the insertion loss of the bandpass filters. Figure 2.27 shows the resulting optical spectra with filters and added EDFA. The CSR ratio is now 18.21 dB without the 60 GHz carrier or ASK modulation, 12.4 dB with the carrier on, and 1.58 dB with both carrier and data on. This equalization of the master to the sideband alleviates the need for high fiber launch power and improves the extinction ratio [67].

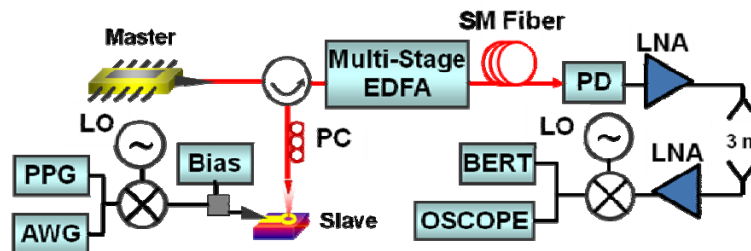


Figure 2.26 Experimental setup of OIL VCSEL RoF transmission system with wireless transmission

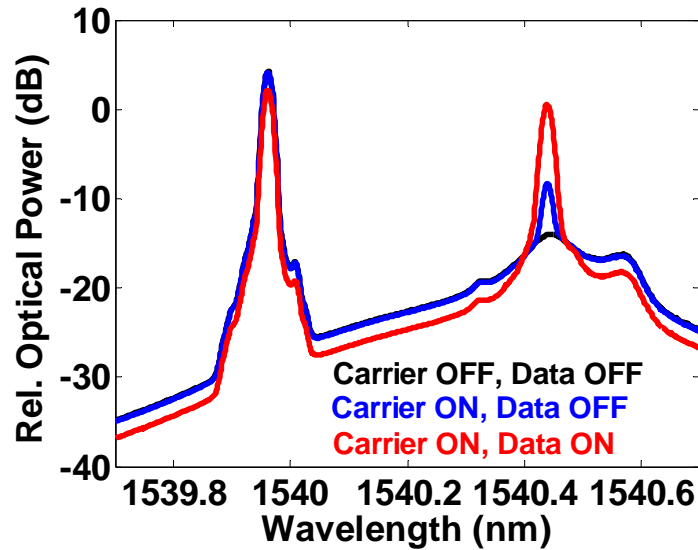


Figure 2.27 Optical spectra of OIL VCSEL RoF link with filters and EDFAs and without modulation (black), with 60 GHz carrier (blue), and with 60 GHz carrier and ASK modulation.

Figure 2.28 shows the small-signal frequency response for the free running VCSEL and for the OIL VCSEL after passing through the filters and EDFAs. The free running VCSEL has a distorted response as low frequency components are attenuated and higher frequency components are amplified. The OIL VCSEL has still has poor response at sub-mm-wave frequencies but at 60 GHz the amplitude of the response has been increased by 13 dB. A 3-dB bandwidth of 18 GHz is centered at 57 GHz for the OIL VCSEL.

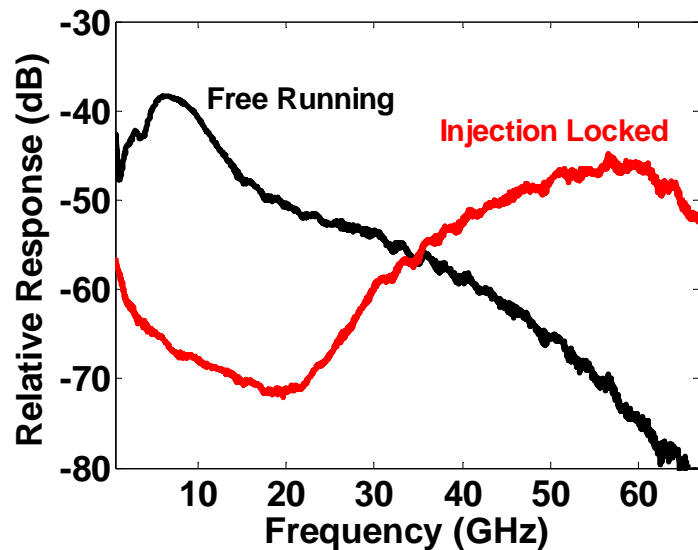


Figure 2.28 EVM versus received optical power for 1 and 2 Gb/s subcarrier modulated QPSK signals on 60 GHz OIL VCSEL RoF link for B2B and 20 km fiber and 3 m wireless transmission.

With this improvement in CSR, a wireless link was set up after the photodetector, with an LNA feeding a standard horn antenna transmitting 3 meters to another standard horn antenna amplified by another LNA and then downconverted back to baseband (Figure 2.26). Additionally, the bit rate for ASK modulation was run at 2 and 3 Gb/s. Bias conditions of the VCSEL and DFB were kept the same as before. These biases again gave the flattest response over the 60 GHz band of interest and low RIN due to OIL. Figure 2.29 shows the BER curves for 2 and 3 Gb/s with length $2^{31}-1$ pseudorandom bit sequences (PRBS) for back to back (B2B) transmission and for 20 km fiber transmission (5.4 dBm optical power after the EDFA), both followed by 3 m of wireless transmission. Compared to the B2B case, both 2 and 3 Gb/s data have an improvement in receiver sensitivity in the 20 km case, the cause of which is under investigation. A slight 0.5 dB power penalty is seen between 2 and 3 Gb/s. In Figure 2.30, the eye diagrams are shown both for 2 Gb/s (with -9.5 dBm optical power at the receiver for B2B, and -10.5 dBm for 20 km) and 3 Gb/s (-9 dBm for B2B, and -10 dBm for 20 km).

The VCSEL was also modulated by 4 Gb/s ASK data, with length $2^{31}-1$ PRBS for B2B and for 10 km fiber transmission, both followed by 3 m of wireless transmission. Figure 2.31 shows the BER curves. The BER curve appears to have flooring at around 10^{-5} . Likely cause of the flooring is limited bandwidth devices in the RF transmitter/receiver path. Nevertheless, these results have already satisfied the FEC limit and could possibly be further improved by using feed-forward equalization (FFE) [63].

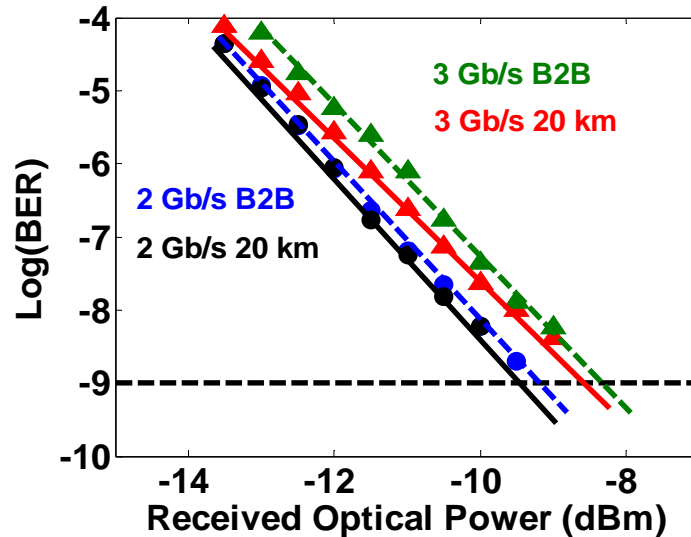


Figure 2.29 BER curves for 2 and 3 Gb/s ASK baseband modulation of 60 GHz OIL VCSEL RoF link for B2B (dashed) and 20km fiber, and 3 m wireless transmission.

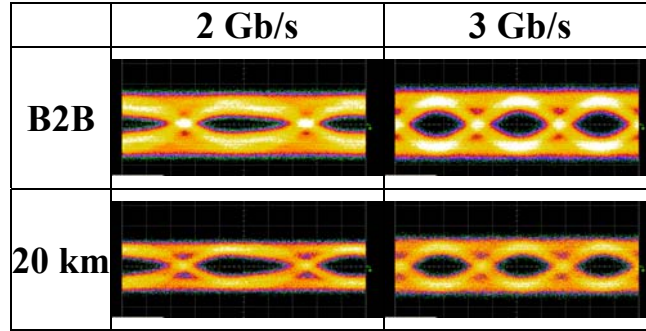


Figure 2.30 Eye diagrams of 2 and 3 Gb/s ASK baseband modulation after 60 GHz OIL VCSEL RoF link for B2B (-9.5 dBm 2 Gb/s/-9 dBm 3 Gb/s) and 20km (10.5 dBm 2 Gb/s /-10 dBm 3 Gb/s) fiber and 3 m wireless transmission

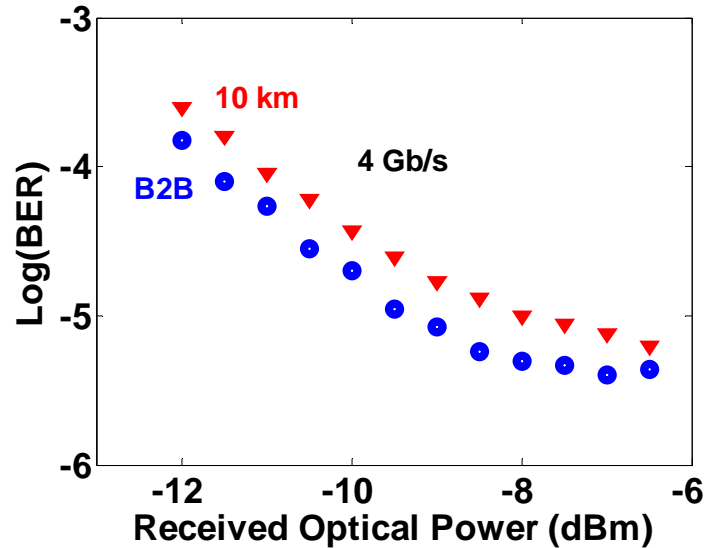


Figure 2.31 BER curves for 4 Gb/s ASK baseband modulation of 60 GHz OIL VCSEL RoF link for B2B and 10km fiber, and 3 m wireless transmission.

In addition to the ASK baseband modulation, QPSK subcarrier modulation of 1 and 2 Gb/s with PRBS length 2^9-1 was created by the AWG and measurements were taken for B2B and 20 km fiber transmission (5.7 dBm optical power after the EDFA) with 3 m wireless transmission. Biasing conditions were kept the same from the ASK modulation experiment. For the 1 Gb/s case, the subcarrier was 1 GHz away from the RF carrier (Figure 2.32), while for 2 Gb/s the subcarrier was located 1.5 GHz away from the 60.5 GHz carrier. Figure 2.33 shows the constellation diagram of the 1 and 2 Gb/s QPSK signals at 15 and 10(1 Gb/s)/-8(2 Gb/s) dBm received optical power for the B2B case.

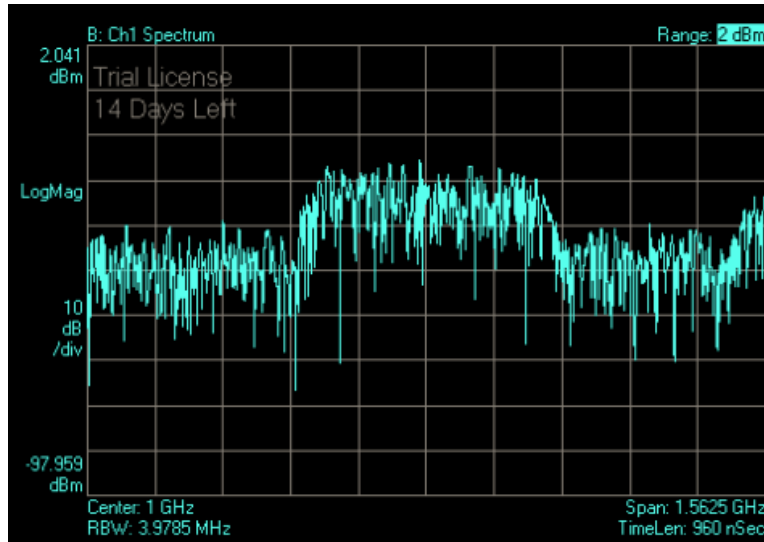


Figure 2.32 RF spectrum of 1Gb/s QPSK subcarrier located 1 GHz away from the 60 GHz carrier after propagation over 20 km SSMF and 3 m wireless.

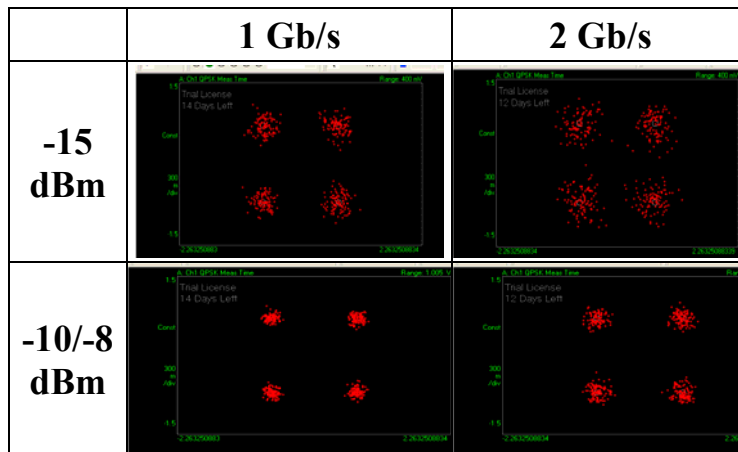


Figure 2.33 Constellation diagrams for 1 and 2 Gb/s subcarrier modulated QPSK signals on 60 GHz OIL VCSEL RoF link after for B2B fiber and 3 m wireless transmission at different received powers (-15 dBm for 1 and 2 Gb/s, -10 dBm for 1 Gb/s and -8 dBm for 2 Gb/s).

Figure 2.34 and 2.35 shows the error vector magnitude (EVM) and signal to noise (SNR) ratio for the QPSK signal versus received optical power for the two bit rates; no power penalty is seen between the B2B and 20 km fiber transmission at either bit rate. Figure 10 shows the constellation diagram of the 1 and 2 Gb/s QPSK signals at 15 and 10(1 Gb/s)/-8(2 Gb/s) dBm received optical power for the B2B case.

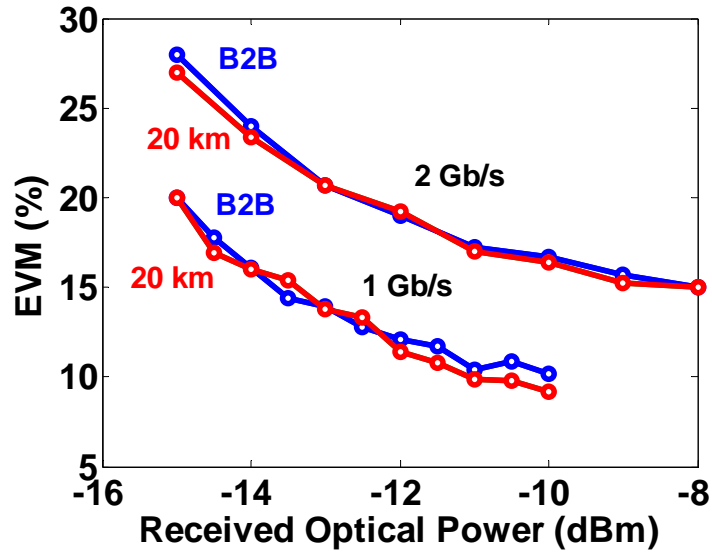


Figure 2.34 EVM versus received optical power for 1 and 2 Gb/s subcarrier modulated QPSK signals on 60 GHz OIL VCSEL RoF link for B2B and 20 km fiber and 3 m wireless transmission.

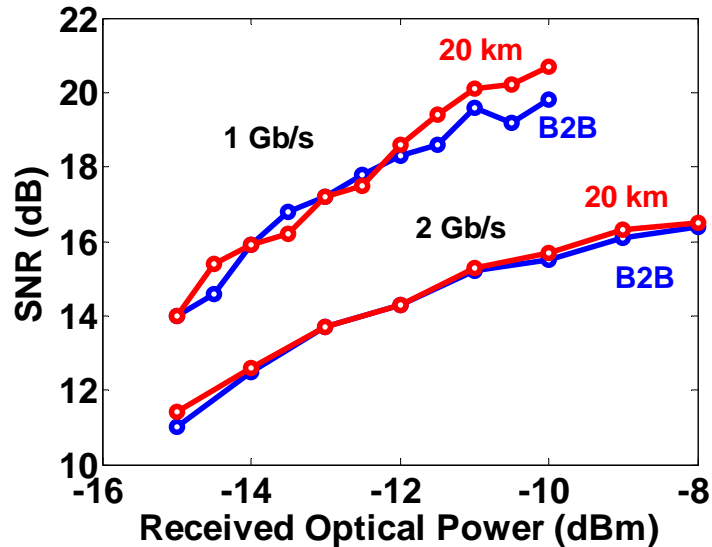


Figure 2.35 SNR versus received optical power for 1 and 2 Gb/s subcarrier modulated QPSK signals on 60 GHz OIL VCSEL RoF link for B2B and 20 km fiber and 3 m wireless transmission.

2.1.5 Conclusion

We have experimentally demonstrated a directly modulated 60 GHz RoF transmitter capable of transmitting up to 3 Gb/s ASK and 2 Gb/s subcarrier QPSK signals using an OIL VCSEL. This demonstration shows the viability of using a directly modulated OIL VCSEL to transport

broadband signals in the 60 GHz band for future wireless access networks. Current work is under way to increase the bit rate and use more spectrally efficient modulation formats. Lastly, the versatility of OIL VCSELs makes them ideal candidates for any sub-THz carrier frequency RoF transmission.

2.2 Optoelectronic Oscillator

The generation of low phase noise signal frequencies in the radio frequency (RF) band is critical for applications such as radars, RF photonics, frequency standards and optical signal processing [68]. One way of generating these signal is through an optoelectronic oscillator (OEO) demonstrated in [69], using a narrow linewidth CW laser, high speed external modulator, long fiber loop, and a high speed photodetector. These components are put into a loop configuration whereby the CW laser feeds the external modulator, after which the light travels through the fiber loop, detected by the photodetector and then the electrical signal is fed back into the laser after amplification. With enough amplification, the loop will oscillate with high spectral purity due to the long almost lossless cavity provided by the fiber loop. However, to reach the oscillation threshold, high RF gain is needed, additionally the bandwidth of the RF amplifiers and external modulator restrict the upper limit of the generated RF frequency. As described in Section 2.1 optically injection-locked VCSELs have been demonstrated to exhibit high speed frequency response (> 100 GHz) and wide tunability of the resonance peak under direct modulation. Moreover, the cavity mode of the OIL VCSEL amplifies the modulation sideband, which greatly enhances the modulation efficiency at the resonance frequency. In this section, a novel OIL OEO leveraging the high frequency and high gain resonance peak of an OIL VCSEL is demonstrated with a spectrally pure RF tone at 20 GHz with phase noise performance 20 dB better than a commercial RF generator.

The experimental setup is shown in Figure 2.36. The optical injection portion of the experiment is similar to that described in Section 1.3 with majority (99%) output going to the 17 km fiber loop after which it is detected by the photodetector. The electrical signal is then filtered with a bandpass filter centered at 20 GHz, and then amplified by an RF amplifier with 45 dB of gain. The signal is then fed back into the VCSEL through a bias tee completing the loop, with some power tapped off via a pickoff tee to measure the generated signal. The whole setup is thermally isolated via insulation and Plexiglas (Figure 2.37).

Once the OIL VCSEL is tuned so the resonance frequency matches the filter passband, the loop is closed to generate the RF signal. Figure 2.38 shows the open- and closed-loop optical spectra of the OEO, where the cavity mode is significantly enhanced after the loop is closed indicating that oscillation is occurring. A comparison between the OIL VCSEL OEO and HP 83650B signal generator is shown in Figure 2.39 and 2.40. Comparing with a 20-GHz signal generated by the signal generator, the phase noise of the OIL VCSEL OEO is 23 dB lower at 3-kHz offset and 21 dB lower at 5-kHz offset.

As phase noise is inversely proportional to the square of the loop length, we chose a 17 km fiber loop, however, this in turn leads to small free spectral range as can be seen at the 10 kHz offset in the phase noise. The RF bandpass filter mitigates the mode competition by limiting by having a bandpass of only 20 MHz at 20 GHz center frequency, but also limits the tunability to RF oscillation. These two undesirable experimental situations can be mitigated by operating closer to the injection locking stability edge where the RF gain and Q of the resonance are maximized, which also reduces the amount of gain required for the RF amplifier.

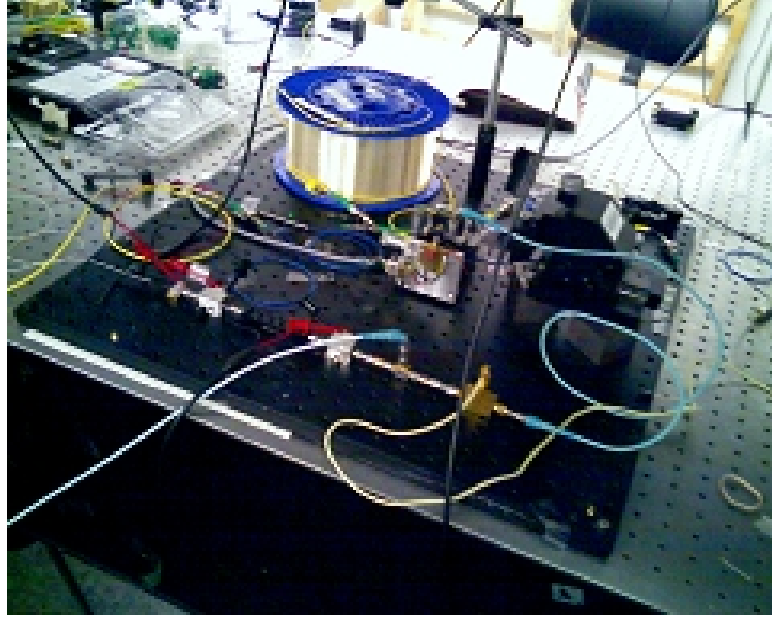


Figure 2.36 Experimental of OIL-based OEO showing DFB based experimental setup

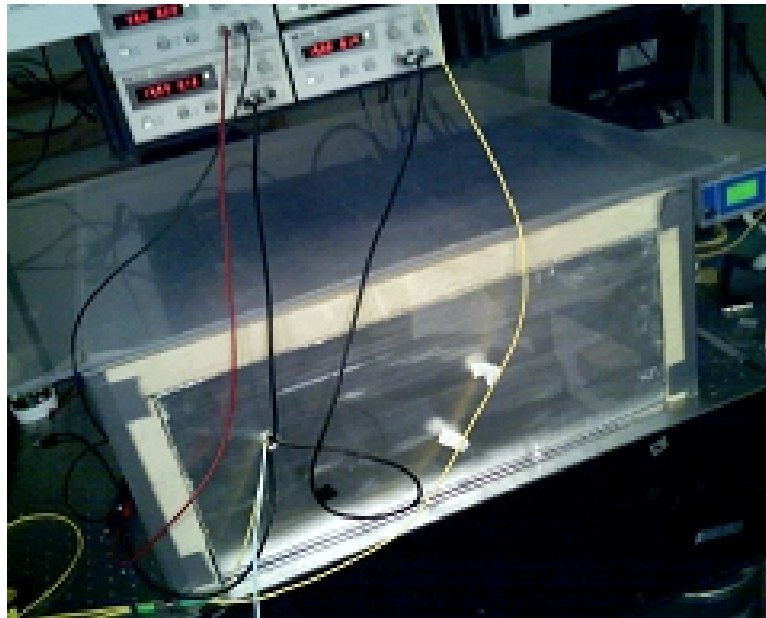


Figure 2.37 Thermal isolation of OIL-based OEO experimental setup using insulation and Plexiglas

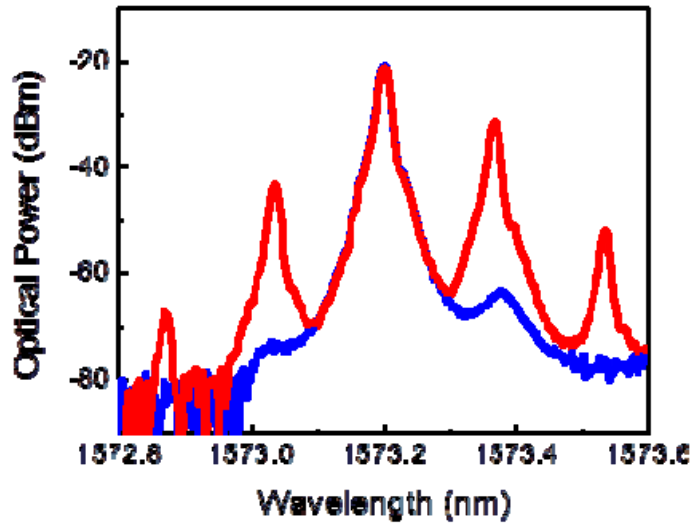


Figure 2.38 Open loop (blue) versus closed loop (red) operation of OEO. Enhancement of the cavity mode is seen in closed loop operation.[70]

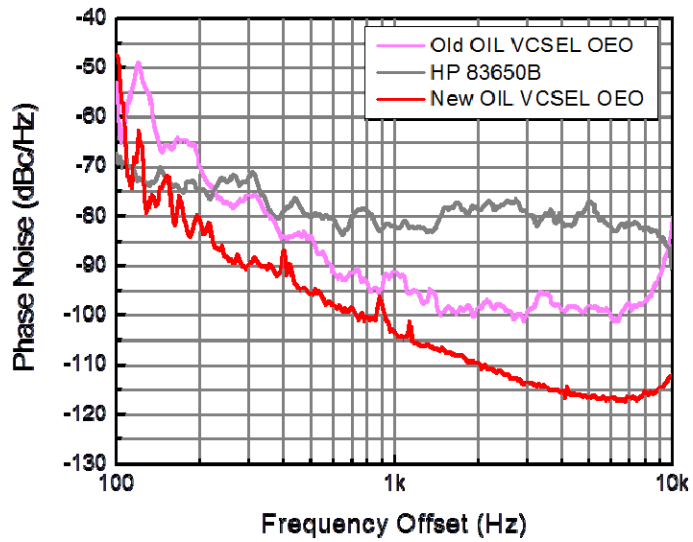


Figure 2.39 Phase noise spectra of OIL VCSEL OEO versus a HP 83650 signal generator.[70]

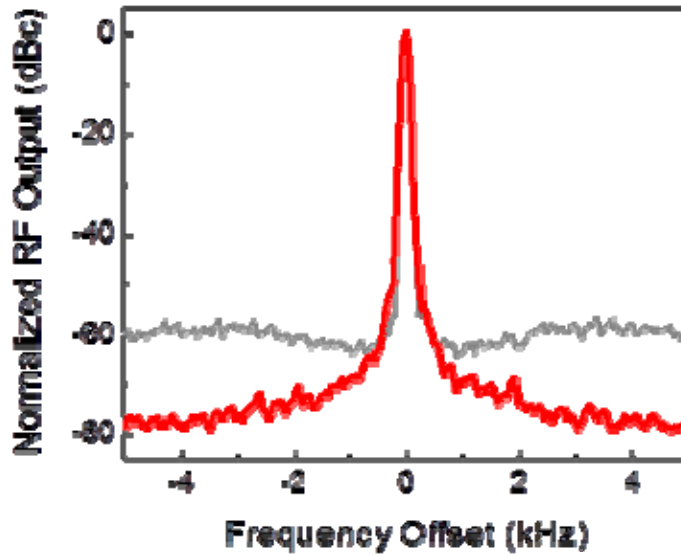


Figure 2.40 RF spectrum of OIL VCSEL-OEO at 20 GHz (red) versus an HP signal generator (grey).[70]

2.3 Polarity-Switchable UWB-Monocycle Generation

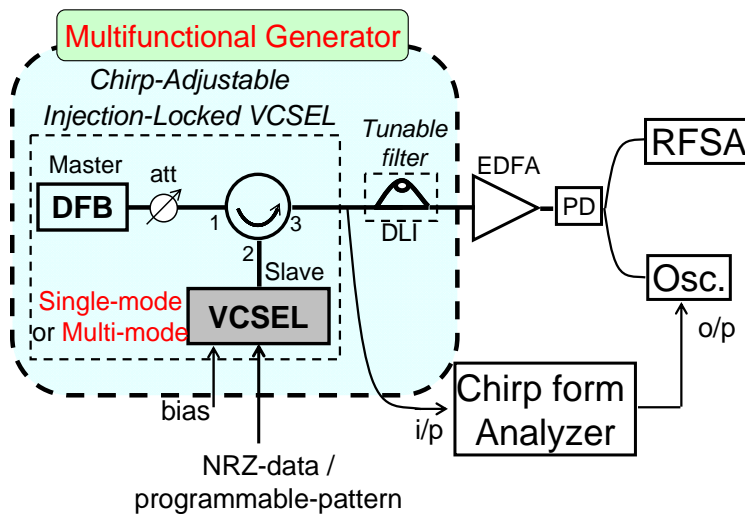


Figure 2.41 Experimental setup of multifunctional generator using a chirp adjustable injection-locked VCSEL followed by a tunable interferometer. [71]

The OIL transition condition as explained in Section 2.3 is critical for the generation of UWB-monocycles. Fig. 2.42 (a) and (b) are the 10-Gb/s NRZ input data pattern and the OIL transition state signal, respectively. By detuning the DLI such that the OIL signal is on either the positive

or negative linear slopes of the filter selecting either the blue or red chirp and attenuates the other, polarity switchable differentiators are generated as shown in Fig. 2.42 (c) and (d).

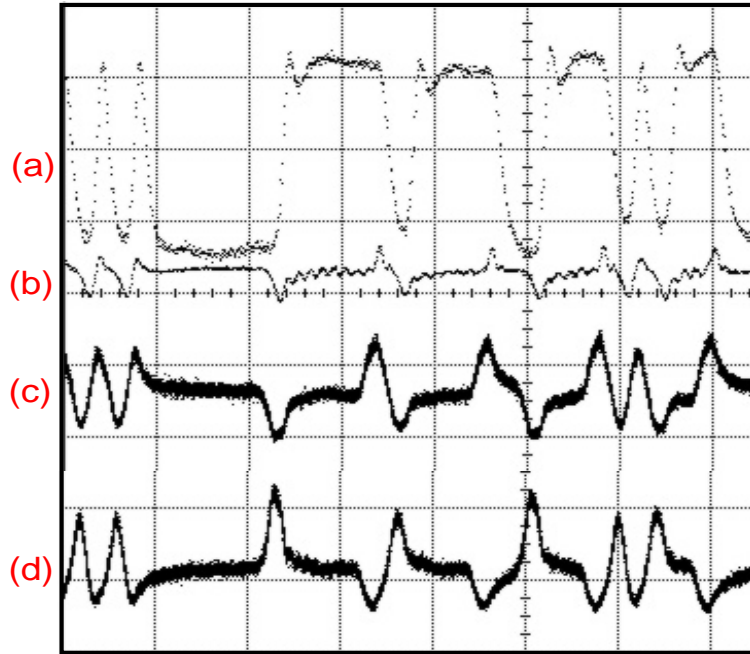


Figure 2.42 Polarity-switchable differentiator from positive and negative slope of DLI. [71]

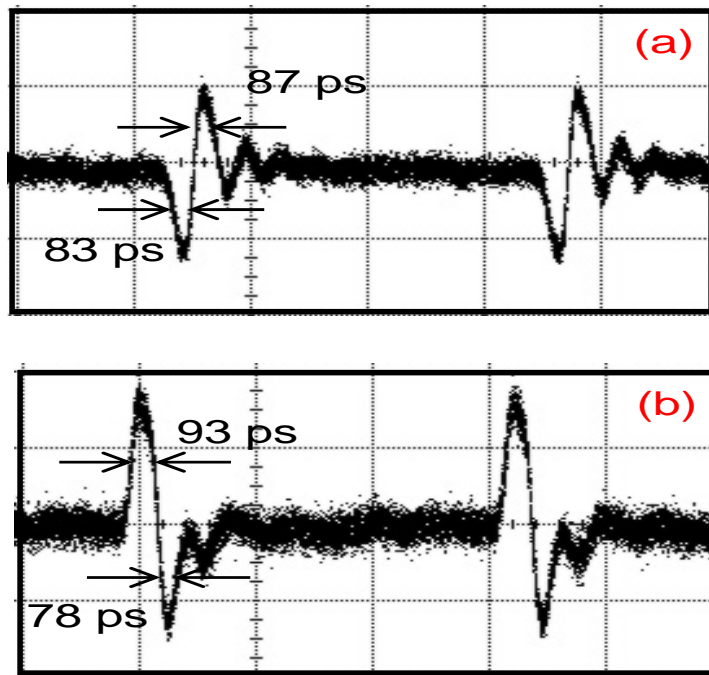


Figure 2.43 Measured UWB-monocycles using multi-mode VCSEL under OIL. [71]

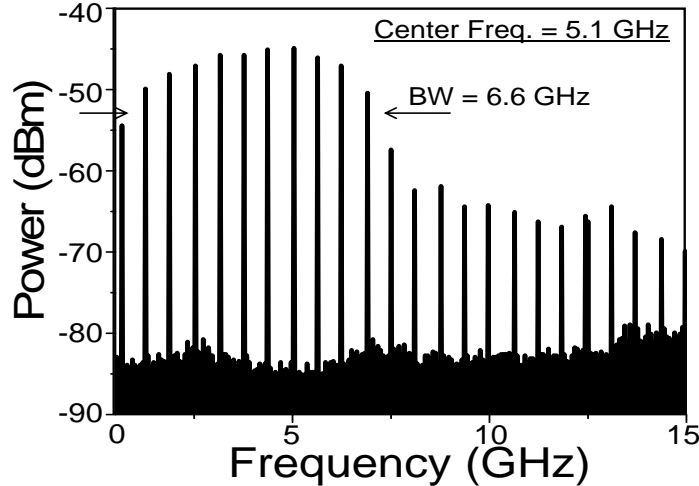


Figure 2.44 RF spectrum of the UWB-monocycle of Figure 2.37 showing 129% fractional bandwidth at 5.1 GHz. [71]

Since multi-transverse mode VCSELs become single mode after optical injection, we chose to use a 10 μm aperture VCSEL with three transverse modes for the experiment to demonstrate UWB-monocycle generation, by using a cost-effective multi-mode VCSEL. To generate the UWB signal, the pattern generator is programmed to output a data pattern of “1000000000000000” or one “1” bit every 16 bits, this creates one polarity of the UWB-monocycle in Figure 1 when the DLI is blue shifted 0.04 nm relative to the center frequency of the OIL signal. The upper half of the UWB-monocycle has FWHM of 87 ps with the lower half of the monocycle having a FWHM of 83 ps. When the DLI is red shifted by 0.04 nm, we obtain the other polarity of the UWB-monocycle. This monocycle has a 93 ps upper half FWHM and 78 ps lower half FWHM, a larger asymmetry than the other polarity due to the asymmetry in the frequency chirp. The RF spectrum of the monocycle corresponding to Figure 3 is seen in Figure 7. The center frequency is 5.1 GHz with a 10 dB bandwidth of approximately 6.6 GHz (from 0.8 GHz to 7.4 GHz). This results in a generated monocycle pulse with a fractional bandwidth of 129%, which meets the FCC definition for UWB signals. Also, it can be noted that the frequency tone spacing is 0.625 GHz which is the same as the input repetition rate (10/16 Gbps).

2.4 Summary

In conclusion, we have demonstrated that optical injection locking of VCSELs can improve performance in analog communication systems. Resonance frequency for both single and multi-transverse mode VCSELs can be enhanced well into the millimeter-wave range. This enhancement allows for radio over fiber at 60 GHz where we demonstrated a 4 Gb/s data stream over fiber and wireless. Moreover, an optoelectronic oscillator was demonstrated showing better phase noise performance at 20 GHz than commercial signal generators.

Chapter 3 Digital Applications of Optically Injection Locked VCSELs

3.1 Motivation

Digital fiber optic communications have become the workhorse of today's wireline communication systems. However, performance limitations especially in bandwidth hamper its adoption in many applications. Optical injection locking of VCSELs provides a solution for this by modifying the dynamics of the VCSEL and thus improves performance. In this chapter, the different applications and performance enhancements for digital fiber communications by optical injection locking are explored.

3.2 Adjustable Pattern Inversion

3.2.1 Single Transverse Mode VCSEL

The experimental setup is the same as that described in Section 1.3.1. A VCSEL with a threshold of 0.6 mA and maximum output power of ~ 1.5 mW biased at 10 mA was used with a CW DFB master laser with maximum output power of 40 mW. A Bit Error Rate test set is used to modulate the VCSEL at 10 Gb/s with PRBS15. Fiber spools of various lengths were then added after the circulator to simulate transmission and dispersion characteristics.

The experimental results are shown in Figure 3.1, where the error-free power penalty is plotted against the SSMF transmission distance for a 10 Gbps PRBS15 modulation of the VCSEL. The power penalty is referenced to the free-running back-to-back condition for the OIL VCSEL. At 25 km an optimal transmission distance is achieved where the negative chirp of the OIL VCSEL compensates the chromatic dispersion of the fiber. In practical systems, a fixed power penalty is used to compare transmission distances while varying the experimental parameters, in this case we choose a power penalty of 4 dB for comparison. For a directly modulated VCSEL, the large positive chirp severely limits the transmission distance and the 4

dB power penalty distance is less than 10 km. In the case of OIL, for B2B, the system experiences a 3 dB power penalty, which decreases to 0 dB at 25 km and then slowly increases again to 4 dB at 120 km, a whole order of magnitude larger than the free running case. This phenomenon indicates the existence of negative chirp, which compensates the chromatic dispersion of the fiber. In [], this phenomenon is expounded upon further. Pulse compression can also be clearly seen in the eye diagrams for 25 and 100 km compared to the B2B case again indicating negative chirp.

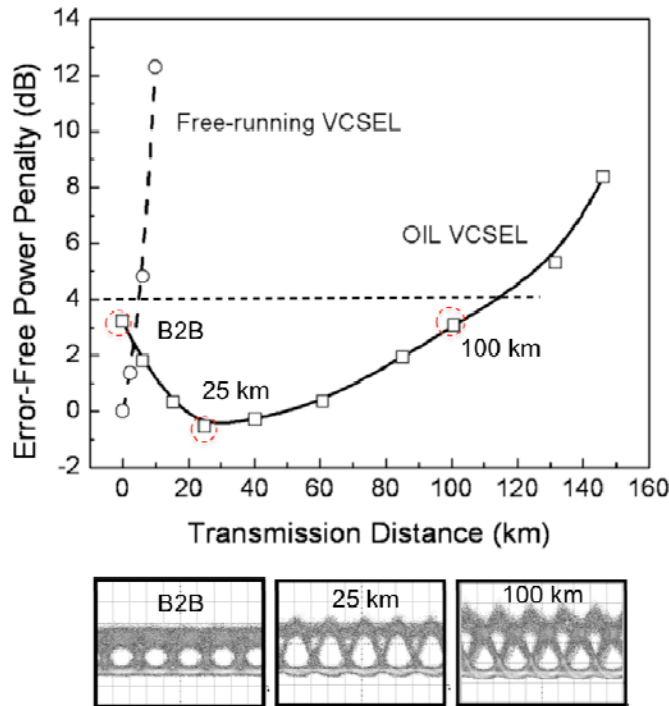


Figure 3.1 Transmission measurements demonstrating distance enhancement of a direct-modulated OIL VCSEL with negative chirp at 10 Gb/s. Eye diagrams for OIL VCSEL at back-to-back (B2B), after 25-km and 100-km transmission are shown.[72]

3.2.2 Multi-Transverse Mode VCSEL

Directly modulated, multi-transverse mode vertical cavity surface emitting lasers (MM VCSELs) are extensively used in local and storage area networks due to their low cost and wide bandwidth [73]. However, modal and chromatic dispersion prevent them from being used for longer reach networks. Frequency chirp reduction and spectral narrowing must be realized for MM VCSELs to achieve longer distance transmission over standard single mode fiber (SSMF). Previously, it has been demonstrated that optical injection locking (OIL) of a multi-transverse mode VCSEL can effectively convert it into a single transverse mode device thus mitigating modal dispersion [58]. Moreover, frequency chirp reduction and inversion resulting in transmission distance enhancement has been observed for OIL single transverse mode VCSELs [34].

In this section, we present adjustable chirp in a multi-transverse mode VCSEL using optical injection locking. By adjusting the frequency chirp polarity using OIL, the chirp of the VCSEL can be changed from positive to negative frequency chirp. This negative chirp compensates for chromatic dispersion thereby extending transmission distance. We demonstrate a transmission distance enhancement for a 1550 nm 10 μm aperture multi-transverse mode VCSEL from 1 km to 90 km at 10 Gb/s. Similarly, for larger aperture (15 μm) devices the transmission distance can be extended from 2 km to 32 km by chirp reduction using OIL. Moreover as an all-optical technique, OIL can be applied to various modulation formats, bit rates, or fiber types and can be applied post-deployment to VCSEL-based transmission systems.

3.2.3 Background

Frequency chirp of a VCSEL is determined by the change in carrier density with respect to current modulation. When the carrier density is increased or decreased a frequency transient (transient chirp) occurs after which the frequency of the laser settles to a new shifted value (adiabatic chirp) [74], [75]. For an increasing drive current, the VCSEL carrier density also increases, leading to an increase in the gain. From the Kramers-Krönig relation, this increase in the gain corresponds to a decrease in the real part of the refractive index, which increases the laser frequency. So, a positive transient chirp is observed on the rising edge of an optical pulse, while negative transient chirp is seen on the falling edge. This positive transient chirp, and to a lesser degree the adiabatic chirp, results in pulse spreading due to the positive dispersion of SSMF, where higher frequency components of the pulse travel faster than lower frequency components. Inter-symbol interference (ISI) then results once the pulse has spread beyond one bit period. Optical injection locking has previously been shown to reduce the adiabatic chirp as the frequency of the VCSEL is locked to that of the master laser [19], [36]. More recently, we reported an inversion of transient chirp for single transverse mode OIL VCSELs modulated at 10 Gbps, and the resulting extension of SSMF transmission distance from 10 km to 120 km with a 4 dB power penalty. In the following, we demonstrate the greatly enhanced transmission distance of a directly-modulated multimode VCSEL by combining the spectral narrowing and the data inversion phenomena in optical injection locking.

3.2.4 Experimental Setup

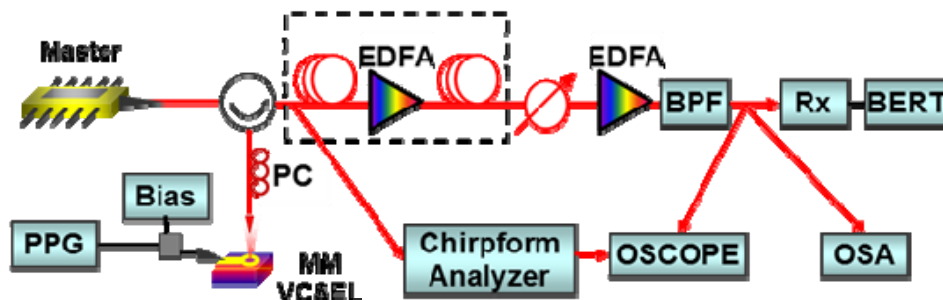


Figure 3.2 Schematic of experimental setup for frequency chirp study

Figure 3.2 shows the experimental setup. The multimode 1550 nm BTJ VCSEL is directly

modulated at 10 Gb/s by a pulse pattern generator (PPG) with its output coupled to a single mode lensed fiber. The master laser is a high power distributed feedback (DFB) laser, which is coupled to port 1 of a circulator and then injects into the VCSEL located at port 2. To maximize injection ratio ($R=P_{inj}/P_{VCSEL}$), a polarization controller is inserted between port 2 and the lensed fiber to match the polarization of the master laser to the VCSEL. The circulator can be replaced with a 3-dB power splitter to lower the cost with a tradeoff in higher master laser output power and negligible performance degradation. From the output of the circulator the data is transmitted over various lengths of SSMF after which it goes to a bit error rate tester, optical spectrum analyzer (OSA), and oscilloscope. Additionally, the output of the circulator is split to a chirpform analyzer, which measures the chirp of the laser in comparison to the modulation pattern.

3.2.5 Results

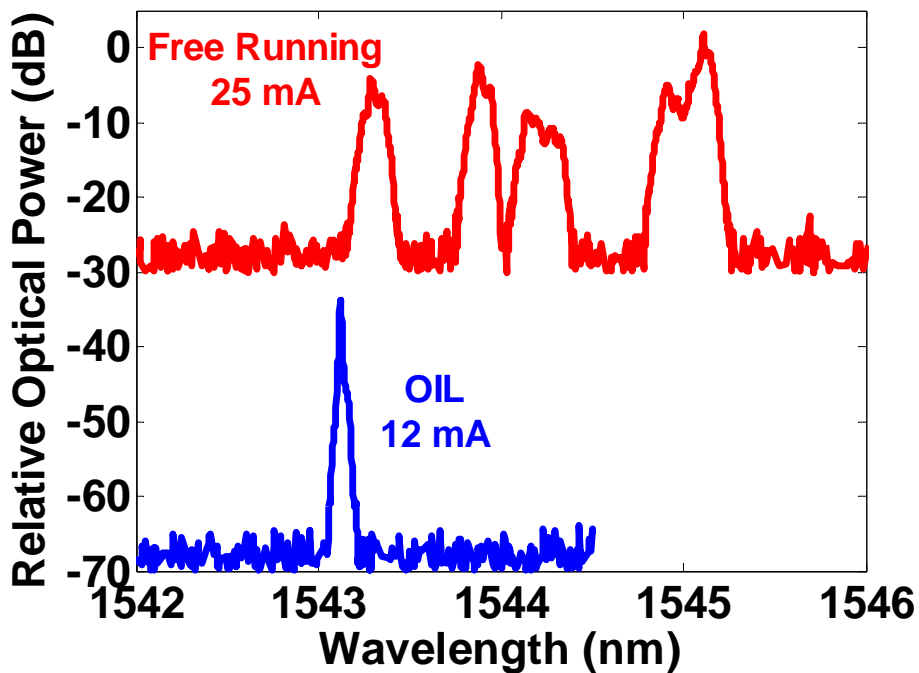


Figure 3.3 Optical spectra of the same 15 μm MM VCSEL modulated at 10 Gb/s free-running (top) and under injection locking (bottom). VCSEL bias is shown for each.[76]

Figure 3.3 shows the optical spectra of a typical MM VCSEL at 10 Gb/s modulation. Multiple modes spanning 2.5 nm can be seen for the free running case contributing to modal and chromatic dispersion. Under optical injection locking the number of modes is reduced to one and the spectrum is narrowed to under 0.3 nm, effectively making the MM VCSEL a single-mode transmitter.

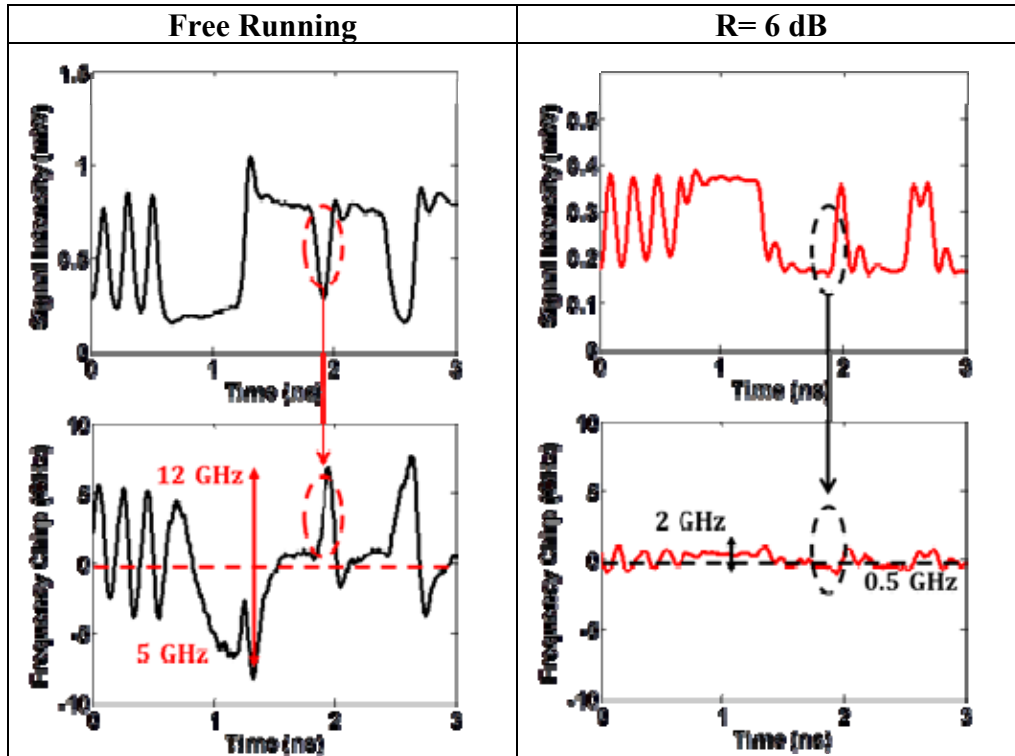


Figure 3.4 Measured intensity and chirp waveforms for free-running and R=6 dB optically injection-locked 10 μm aperture MM VCSELs. The peak-to-peak transient (above line) and adiabatic (below line) chirp are reduced by a factor of 6 through injection locking. [76]

Figure 3.4 shows a 10 Gb/s modulated bit pattern and chirp waveform for a free running 10 μm aperture multimode BTJ VCSEL with a threshold of 4.6 mA and maximum output power of ~ 5 mW biased at 27 mA. Biased at 24 mA with a $2^{11}-1$ PRBS at $1.1 V_{p-p}$, the VCSEL has a transient chirp of 12 GHz, adiabatic chirp of 5 GHz, and extinction ratio of 4.9 dB. To improve performance, the VCSEL was then injection locked by a high power CW distributed feedback (DFB) master laser with maximum output power of 80 mW at 375 mA. With a 6 dB injection ratio, VCSEL now biased at 10 mA, the transient chirp is reduced to 2 GHz and adiabatic chirp to 0.5 GHz, with the extinction ratio of 2 dB. However, the bit pattern is now inverted with respect to the drive modulation making the transient chirp negative.

Chirp measurements were also performed for a free running 15 μm aperture multimode BTJ VCSEL with a threshold of 10 mA and maximum output power of 6 mW at 35 mA bias. We modulated the MM VCSEL at 10 Gb/s and injection locked at two different injection ratios (Fig. 3.5). The free running VCSEL biased at 12.2 mA has a transient chirp of 11 GHz and adiabatic

chirp of 2 GHz with 4.2 dB extinction ratio. With 3 dB injection ratio the transient and adiabatic chirp is reduced to 7 GHz and 1 GHz, respectively, while extinction ratio remains constant at 4.2 dB. At 6 dB injection ratio the transient chirp is reduced further to 4 GHz and adiabatic chirp to 0.5 GHz, with the extinction ratio reducing to 3.5 dB due to master reflection light. Inversion was not observed for this 15 μm OIL MM VCSEL, due to the limited locking range and poor optical injection efficiency compared to the 10 μm MM VCSEL.

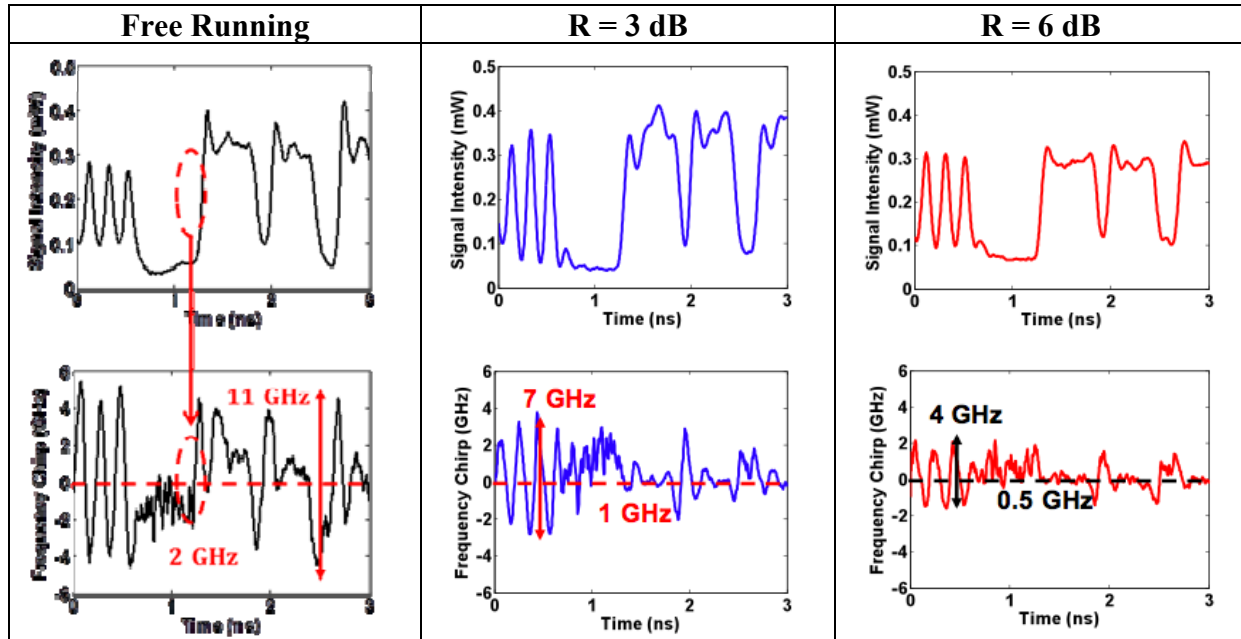


Figure 3.5 Measured intensity and chirp waveforms for free-running, R=3 dB, and R=6 dB optically injection-locked 15 μm aperture MM VCSELs. The peak-to-peak transient (above line) and adiabatic (below line) chirp are reduced by almost a factor of 3 through injection locking.[76]

Applying this chirp reduction and inversion to a transmission link, extended transmission distance can be achieved by dispersion compensation. Figure 3.6 shows the power penalty versus SSMF transmission distance for the 10 μm MM VCSEL, where power penalty is referred to the additional required optical power to reach error-free ($\text{BER} < 10^{-9}$) as comparing to the free-running VCSEL, 0 km transmission case. For the free-running case the transmission over SSMF is problematic due to large modal and chromatic dispersion resulting in ~ 1 km of transmission with 4 dB of power penalty. When injection locked with an injection ratio R=6 dB, the negative chirp causes the bits to compress after propagation over 25 km of SSMF, resulting in a decrease in the needed received optical power to achieve error-free performance or a negative value in power penalty. After longer distance, ~ 25 km as shown here, the bits begin to disperse again and hence the power penalty increases. For this case, it takes 90 km fiber distance to reach the same 4-dB power penalty point. This is nearly two orders of magnitude increase in transmission distance compared to the free-running case. Error-free eye diagrams of the OIL VCSEL at the different transmission distances are also shown in Fig. 3.7.

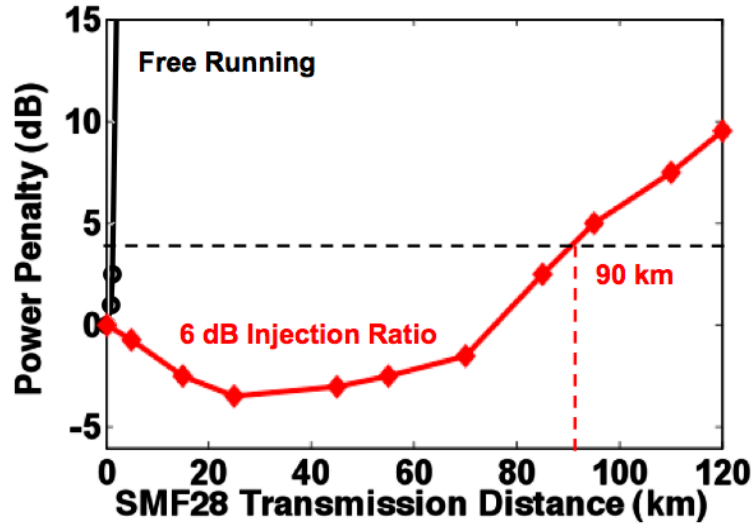


Figure 3.6 Transmission measurements demonstrating distance enhancement of a direct-modulated OIL 10 μm aperture MM VCSEL with negative chirp at 10 Gb/s. [76]

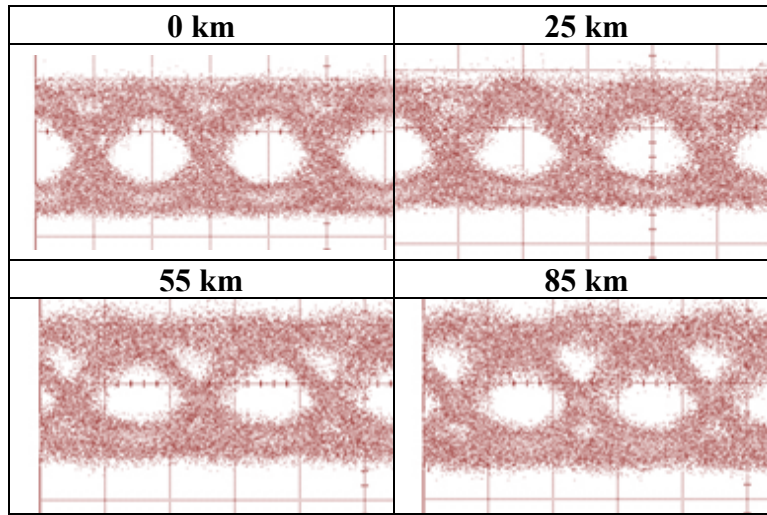


Figure 3.7 Optical eye diagrams for OIL VCSEL at 0 km, after 25, 55 and 85-km transmission are shown. [76]

This transmission distance improvement can also be seen for the 15 μm aperture MM VCSEL (Figure 3.8). At 10 Gb/s, the free-running VCSEL achieves error-free transmission at -21 dBm received optical power. For the 0 km case, the R=3 dB OIL case suffers a 1.5 dB power penalty due to the distortions in the pattern, however at 6 dB there is a 2.5 dB improvement in received optical power as the distortion is removed and the overshoot is suppressed. Transmission distance for the free-running MM VCSEL is 2 km with a 4 dB power penalty. The R=3 dB case can propagate for 8 km before experiencing the same power penalty. At R=6 dB, transmission distance is extended to ~ 32 km. This extension is a 16x improvement over the free

running MM VCSEL and 2x better than any free-running SM VCSEL or DFB DML reported [77]. Eye diagrams are shown in Figure 3.9.

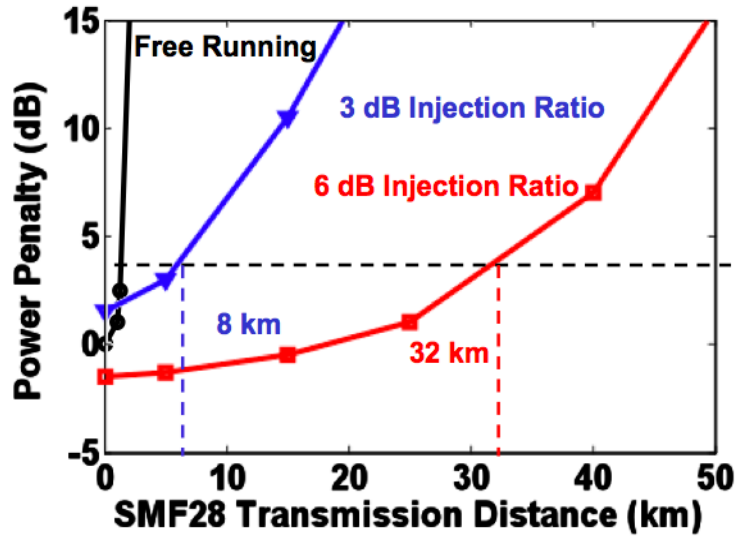


Figure 3.8 Transmission measurements demonstrating distance enhancement of a directly-modulated OIL 15 μm aperture MM VCSEL at R=3 and 6 dB at 10 Gb/s. [76]

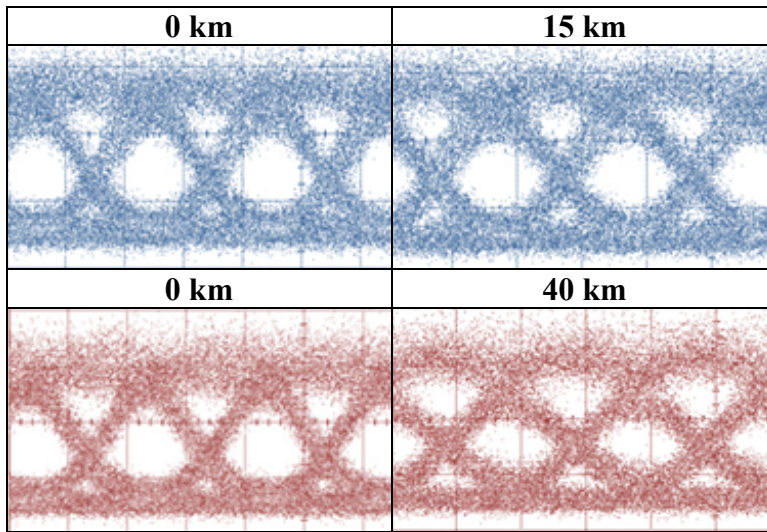


Figure 3.9 Eye diagrams for OIL VCSEL at 0 km and after fiber transmission are shown. [76]

3.2.6 Discussion

An explanation of the data pattern inversion phenomenon reported for single mode OIL VCSEL was provided in Section 1.3. We should point out that the same explanation applies to the case

reported here, i.e. the directly modulated MM VCSEL under injection locking. As a VCSEL is injection-locked, the light from the master laser impinges on the top DBR where the majority (>99.5%) of the light is reflected and a small portion (~0.5%) injects into the VCSEL cavity, schematically depicted by Fig. 3.10. The light entering the cavity reduces the threshold cavity gain needed to achieve lasing at the master wavelength, which results in an increase of the real part of the refractive index due to the KK relation. This red-shifts the VCSEL transverse modes to longer wavelengths as amplified spontaneous emission peaks. This phenomenon has enabled OIL MM VCSELs to achieve an extended resonance frequency of 54 GHz and 3-dB bandwidth of 38 GHz. In addition, the output light of the VCSEL experiences a phase shift (Φ_S) of between $-\pi/2$ and $\cot^{-1}(\alpha)$, and a change in output power, as dictated by the OIL rate equations. This output then destructively interferes with the reflected master light (with a π phase shift). This phenomenon allows for inverting the optical data pattern of the modulated VCSEL in relation to the applied electrical data pattern. Additionally, since the carrier dynamics are governed by OIL rate equations, the magnitude of the frequency chirp (adiabatic and transient) can be adjusted by varying the injection ratio of the master laser into the slave measured at the top facet of the VCSEL or the wavelength detuning between master laser and VCSEL. This makes the technique very powerful and, indeed, with great flexibility for optimization.

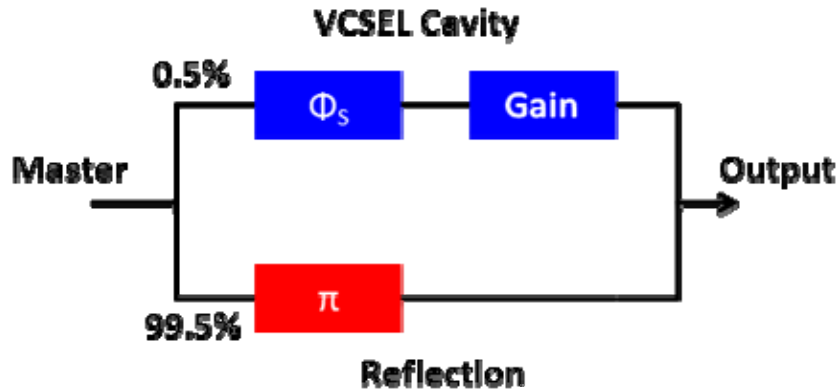


Figure 3.10 Interferometric model of optically injection locked VCSEL. Top path represents light entering VCSEL cavity, where OIL rate equations determine output. Bottom path represents reflection off top facet inducing a $\sim\pi$ phase shift

3.2.7 Conclusion

In summary, we have demonstrated extending the transmission distance of a 10 Gb/s MM VCSEL to 90 km over standard single-mode fiber using OIL. By combining two phenomena of OIL-VCSEL, data pattern inversion and chirp reduction, we are able to reduce transient chirp by 6x and adiabatic chirp by 10x while inverting the data pattern with respect to the drive current modulation. OIL of larger aperture VCSELs was also demonstrated with SSMF transmission distance extension of 16 times to 32 km. These results make an optically injection-locked MM VCSEL a strong candidate for future high-speed optical communications.

3.3 Phase Modulation of Injection Locked VCSELs

3.3.1 Theoretical modeling and simulation

Figure 1.3 shows the reflection model schematic of an OIL-VCSEL. The physics behind this are explained in Section 1.3.3. The output E_s from the cavity is calculated using standard OIL rate equations and the phase shift range is from -0.5π to $\cot^{-1}\alpha$. Fig. 3.11 shows an intuitive diagram based on vectors of the reflection model.

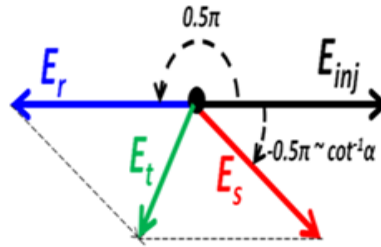


Figure 3.11 Vector based representation of OIL reflection model.[78]

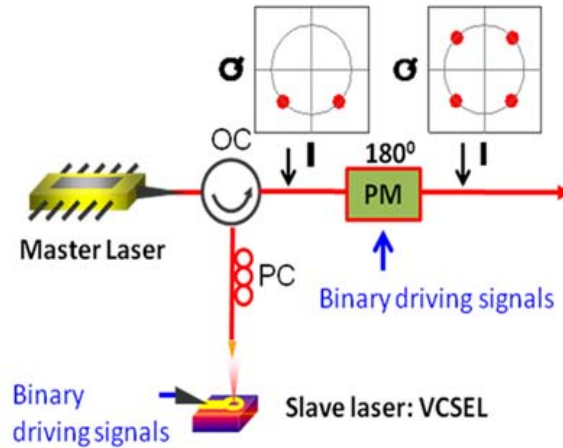


Figure 3.12 QPSK transmitter using phase-modulated OIL. [78]

Under direct modulation of the OIL VCSEL, both amplitude and phase of E_t change. However, using the destructive interference with E_r , the total output E_t can be adjusted so that only phase modulation exists, i.e. the transition state. Figure 3.12 shows a proposed QPSK transmitter based on an OIL-VCSEL. Based on simulation, when an OIL-VCSEL is modulated by an OOK signal under certain condition (wavelength detuning= 0.7 nm, injection ratio=9.0 dB), the output is $\pi/2$ PSK. Adding another π phase modulator, a QPSK transmitter is obtained. Even if the OIL VCSEL in the transition state is modulated by a multi-level drive signal, the amplitude of the VCSEL will be negligible as shown in Figure 3.13. Adjusting the current of this four-level modulation, the output signal can be considered a 4-PSK optical signal. Figure 3.14 shows a schematic for converting this system into an 8PSK transmitter by adding another π phase modulator.

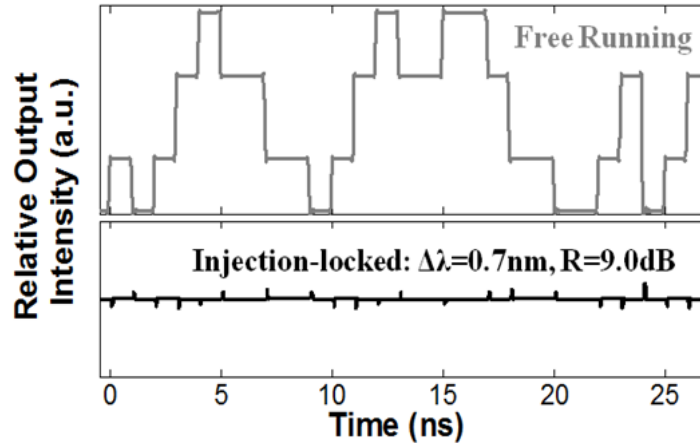


Figure 3.13 Simulated phase modulation at transition state of OIL VCSEL. [78]

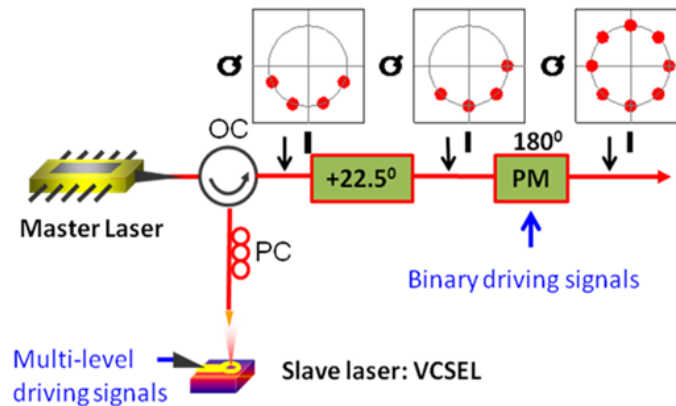


Figure 3.14 8-PSK transmitter based on phase-modulated OIL VCSEL. [78]

3.3.2 Direct Detection Experiment

An experimental setup was created to demonstrate that an OIL VCSEL can generate phase modulation with minimal amplitude modulation (Figure 3.15). To achieve this, an interference arm is added to coherently detect the output optical signal. The OIL setup is similar to that described in Section 1.3 with the VCSEL biased at 7 mA and 2 dBm output power and a CW DFB laser as the master laser. Injection ratio and wavelength detuning are fixed at 10.2 dB and 0.15 nm, respectively and a variable optical attenuator (VOA) and polarization controller (PC) are used on the interference arm to control the magnitude and polarization of the reference light from the master laser.

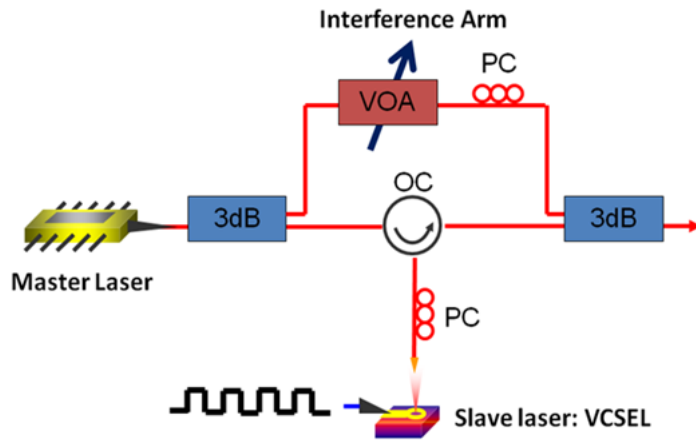


Figure 3.15 Interferometry-based experimental setup for phase modulation.

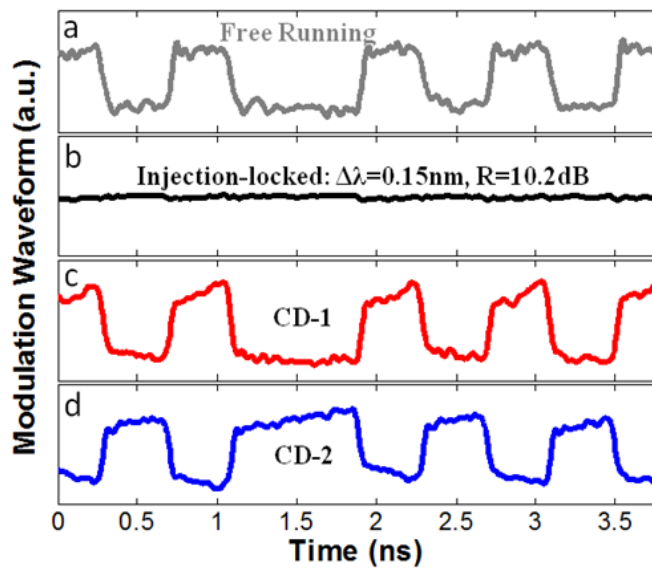


Figure 3.16 Phase modulation of OIL-VCSEL using interferometric setup

Under large signal OOK modulation, the gray curve (a) in Figure 3.16 is the free-running output waveform. When the VOA is set to the blocking state (high attenuation), the output waveform of the OIL VCSEL is the black curve ((b) in Figure 3.16). VOA attenuation is changed to 1.5 dB for coherent detection on the output port, and by adjusting the phase difference between the two arms, we observe the two polarity-switched waveforms (Figure 3.16 (c) and (d)). These results confirm that an OIL-VCSEL can act as a phase modulator. Though the bit rate demonstrated is only 2.5 Gbps, this is only an instrument limitation.

3.3.3 Coherent Demodulation Experiment

Figure 3.17 shows the experimental setup with a master laser injecting into a lensed fiber coupled 1550 nm VCSEL via a circulator. The VCSEL is biased above threshold and modulated at 10 Gb/s by a pulse pattern generator. We analyze the output by using a high-resolution optical spectrum analyzer (OSA). This OSA allows us to directly extract the magnitude and phase information of the modulated signal from the optical spectra via an inverse Fourier transform. Additionally, we also send the output to a delay line interferometer (DLI) to demodulate the signal and view the output on an oscilloscope.

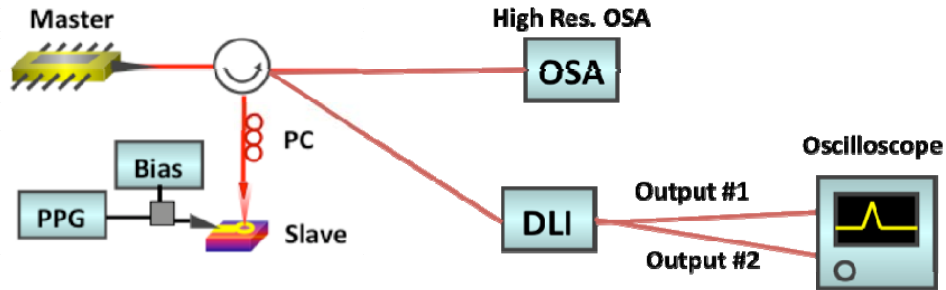


Figure 3.17 Experimental setup for phase modulation of injection locked VCSELs

3.3.4 Results

In a directly modulated optically injection locked VCSEL under large signal modulation both amplitude and phase are modulated. However, by adjusting the injection ratio and wavelength detuning, the destructive interference can effectively suppress the amplitude modulation leaving only phase modulation. By then adjusting the drive voltage the amount of phase swing can then be set. In Figure 3.18 we achieve a phase swing of $\sim 135^\circ$ with a drive voltage of $\sim 1.5 V_{p-p}$ and PRBS7, though not 180° this still allows for DPSK demodulation with a DLI, as shown in Figure 3.19. Open eyes are seen for both ports with observed alternate mark inversion (AMI) and duobinary patterns. Distortions in the phase are caused by polarization switching in the VCSEL which are device-dependent.

By combining this OIL VCSEL phase swing with lithium niobate phase modulators, more advanced modulation formats can be achieved. In Figure 3.20, we combine a phase swing of 45° from the OIL combined with a 90° phase modulator and 180° phase modulator, i.e. a QPSK modulator, to create 8-PSK extending the capabilities of the OIL VCSEL to more spectrally efficient modulation formats. Figure 3.21 shows the resultant phase swing obtained from the high resolution OSA showing 8 phase states as predicted.

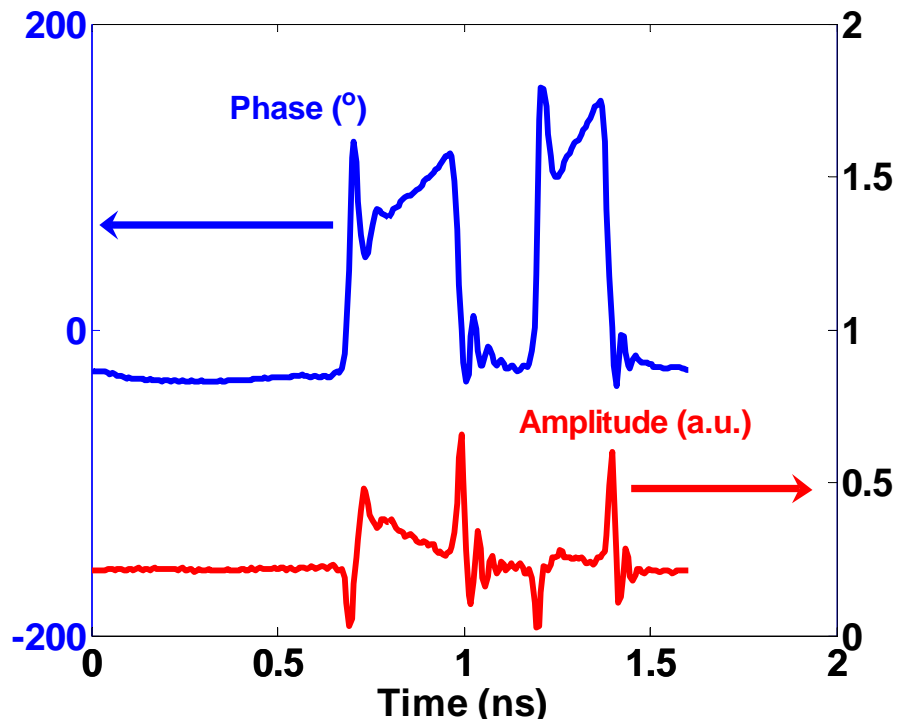


Figure 3.18 Amplitude and phase of 10 Gb/s modulated OIL VCSEL for DPSK modulation

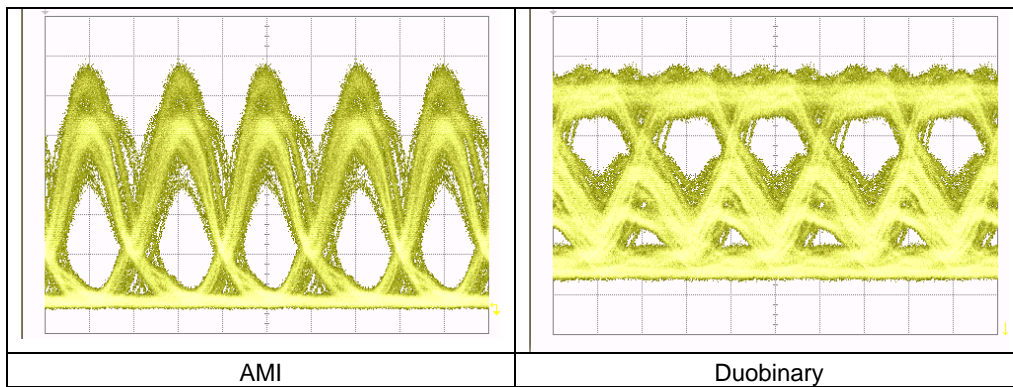


Figure 3.19 Output of both ports of DLI with OIL VCSEL modulated at 10 Gb/s and PRBS7

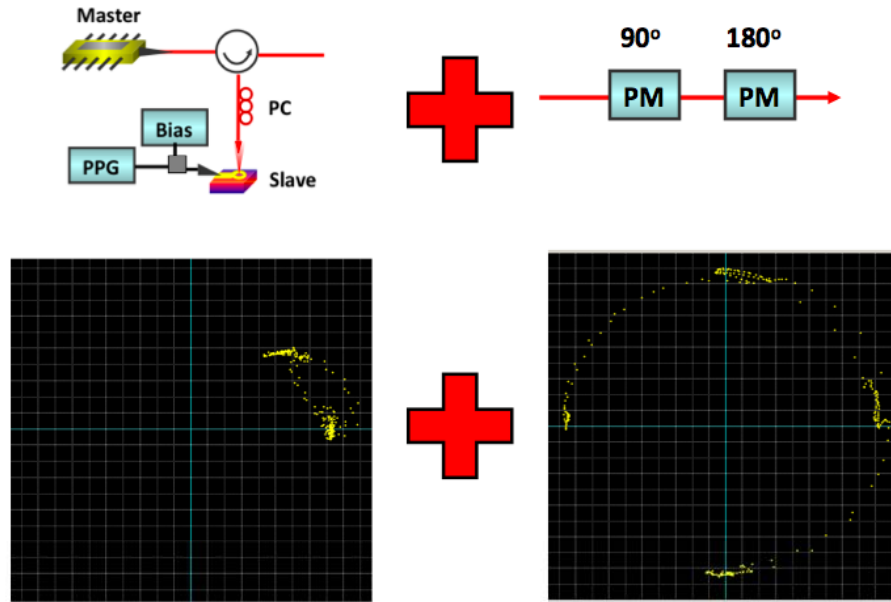


Figure 3.20 Experimental setup for 8-PSK combining an OIL VCSEL with two modulators.

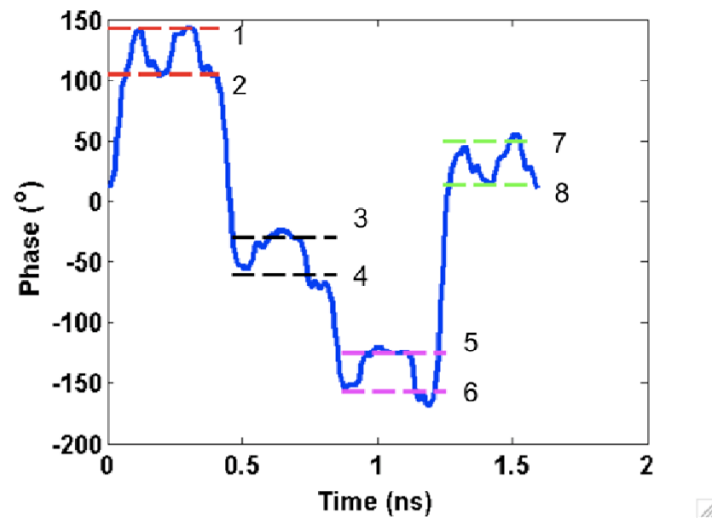


Figure 3.21 8-PSK combining an OIL VCSEL with two phase modulators generating QPSK.

3.3.5 Conclusions

We have experimentally demonstrated phase modulation of an optically injection locked VCSEL. DPSK modulation was achieved by the OIL VCSEL itself and 8-PSK modulation

observed with a QPSK modulator added. OIL VCSELs as phase modulators are a promising directly modulated transmitter for spectrally efficient fiber transmission.

3.4 Advanced Modulation Formats

The rise of datacenters and enterprise LAN has rapidly increased the demand for high-capacity low-cost optical links. However, the bandwidth of directly modulated lasers is unable to keep up with the pace using spectrally inefficient on-off keying (OOK). Previous research has looked at increasing the speed over MMF [79–85], but these use exotic components or external modulation, which are not practical, and are limited by the modal dispersion of the MMF. By using multi-carrier transmission or radio over fiber techniques over SMF, one can overcome these limitations. Moreover, due to advanced modulation formats like quadrature amplitude modulation (QAM), the available bandwidth can be utilized more efficiently.

In this section, we demonstrate 10-Gb/s transmission over SMF using direct modulation of a 1550 nm VCSEL directly directed with a PIN photodetector using spectrally efficient modulation formats. One method uses discrete multi-tone modulation (DMT) in a limited frequency band of achieving a spectral efficiency of >2 bit/s/Hz. DMT is a multi-carrier modulation technique that is already widely used in DSL systems, thus allowing for simple implementation with existing directly modulated transceivers. Another method is single subcycle modulation, where the data is carried at a RF carrier frequency equal to its bandwidth. This allows for higher order modulation formats to be employed to increase the data rate. Both of these solutions show promise in increasing the speed of directly modulated lasers beyond their OOK bandwidth.

3.4.1 Discrete Multi-tone Modulation

DMT is a subset of orthogonal frequency division multiplexing (OFDM) where the modulation output contains only real values without the need for IQ-modulation onto a RF carrier, thereby reducing system complexity and cost by eliminating broadband RF components. A step-by-step guide to generating DMT is shown in Figure 3.22. First, a binary data stream is divided into N parallel sub-carrier streams. Next, every sub-carrier stream is mapped to complex values C_n based on an M -symbol mapping algorithm according to the signal to noise ratio for each subcarrier. C_n is then appended with C_n^* , complex conjugate of C_n , so that the IFFT of the N subcarriers is real. The real output is then converted into a serial stream and then modulated onto the VCSEL. For the receive side the steps are reversed in a complementary fashion.

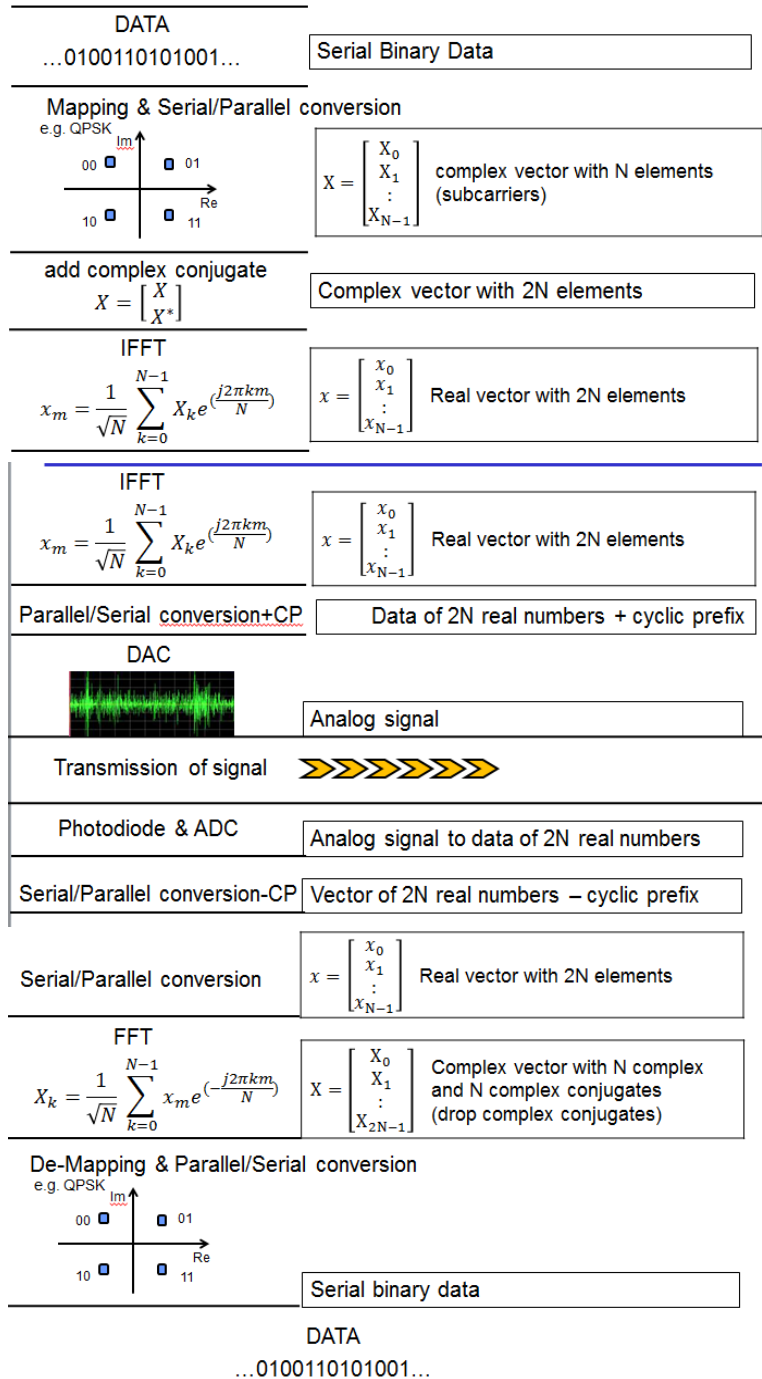


Figure 3.22 Step-by-step guide to DMT generation and reception

Reference [84] shows the experimental setup of our DMT system replacing the 850 nm VCSEL with a 1550 nm VCSEL and MMF with SMF. We use MATLAB to generate the DMT symbol, which is then loaded on the arbitrary waveform generator (AWG). 512 carriers are used with each carrier carrying a 16-QAM signal resulting in 2048 bits per DMT symbol and IFFT length of 1024. The AWG then outputs the points at a rate of 5 GS/s which corresponds to a

time of 204.8 ns per DMT symbol and a transmission speed of $2048/204.8 \text{ ns} = 10 \text{ Gb/s}$. Deducting 7% forward error correction (FEC) and 1% for cyclic prefix results in an aggregate bit rate of 9.2 Gb/s.

The output DMT symbol is then used to directly modulate a 1550-nm single transverse mode VCSEL which is directly coupled to a 10 Gb/s PIN+TIA via a lensed fiber. The electrical signal was then captured by an Agilent Infiniium DSA70804B real-time digital sampling oscilloscope at a sampling rate of 25 GS/s. The 5 times oversampling is necessary since there is no phase locked loop (PLL) for recovery. After capture, the symbols were then converted back into a serial stream in MATLAB using a software-based DMT receiver.

Fig. 3.23 shows the transmitted DMT symbol and constellation diagram for one carrier, while Figure 3.24 shows the received symbol and carrier constellation diagram. The total BER for all 1000 received DMT symbols equals 8.3×10^{-4} .

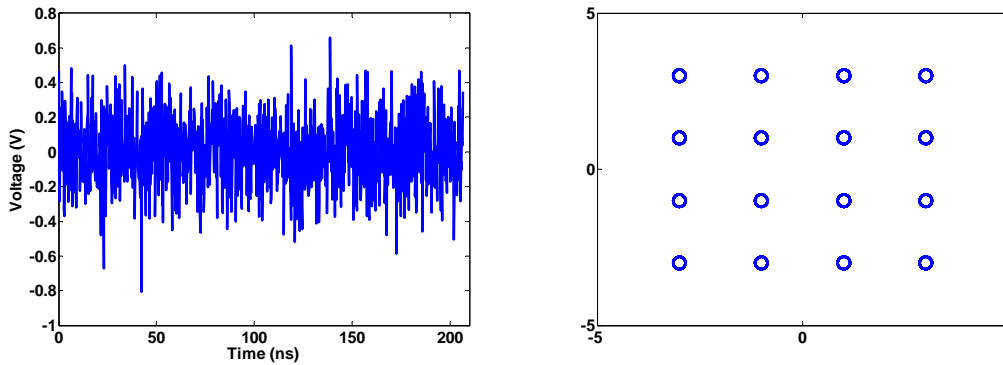


Figure 3.23 Step-by-step guide to DMT generation and reception

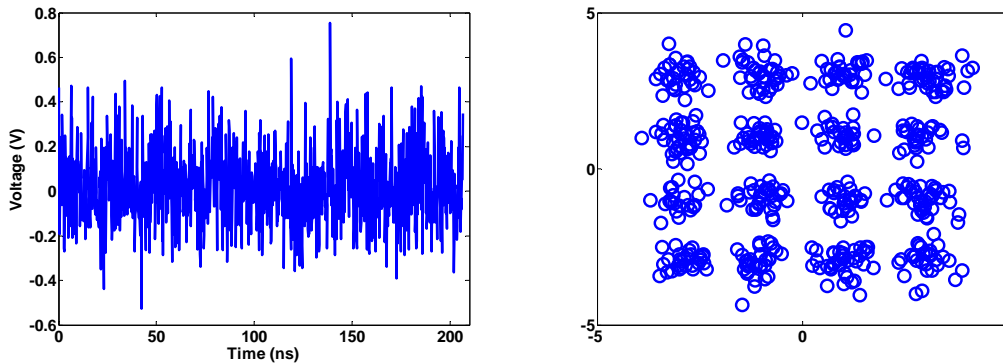


Figure 3.24 Step-by-step guide to DMT generation and reception

Discrete Multi-tone Modulation is experimentally demonstrated using a 1550-nm VCSEL over a back-to-back link. The achieved transmission speed is 10 Gb/s (including 1% of cyclic prefix and 7 % of FEC) in a bandwidth of <5 GHz, thereby achieving a spectral efficiency of >2 bit/s/Hz. This demonstrates that DMT is a promising solution for low-cost next-generation high-capacity links operating beyond 10 Gb/s that can further be increased using WDM.

3.4.2 Single Subcycle Modulation

In recent years, there has been a significant interest in the short range high-capacity optical links. Vertical cavity surface emitting lasers (VCSELs) are often proposed for these systems due to their low cost and good performance. Moreover, long-wavelength versions can be wavelength division multiplexed to save on fiber and increase capacity. Recently, a 40 Gb/s OOK long wavelength VCSEL was demonstrated operating at 1550 nm, but due to dispersion of the single mode fiber was only demonstrated for back-to-back. Therefore, more spectrally efficient modulation formats have to be implemented to deal with the dispersion. Discrete multi-tone modulation, described in section 3.4.1, while promising as far as spectral efficiency and dispersion, requires heavy demands of electronics (i.e. analog to digital (ADC) and digital to analog (DAC) converters). Though, there have been recent improvements the analog bandwidth of DACs is still lower than the best VCSELs, so these lasers cannot be fully utilized. Moreover, DMT suffers from other issues like low power efficiency, high peak-to-average power ratio (PAPR), and heavy computational processing requirements which prevent practical real time implementations.

In this section, we report transmission of 10 Gbps over back-to back singlemode fiber using 16-QAM on a single subcarrier in 10 GHz modulation bandwidth. The VCSEL used was a 1550 nm BTJ VCSEL with 10 GHz 3-dB bandwidth. Figure 3.24 shows the experimental setup for the single subcycle modulation. The advantage of this method is the ready availability of components such as a digital logic gate (XOR) to generate the QAM signal without needing DAC/ADCs. For the receiver side, we use an offline DSP with equalization.

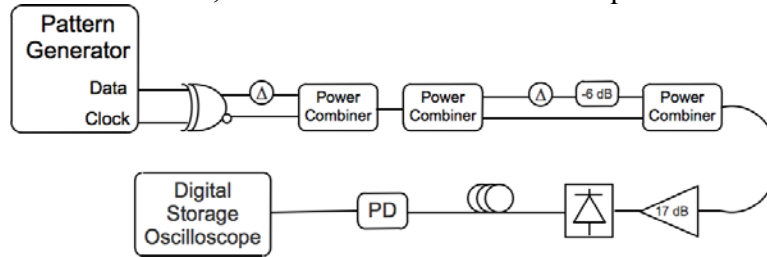


Figure 3.25 Test setup for single subcycle modulation of VCSEL

Fig. 3.25 shows the test setup. The transmitter consists of a VCSEL with a 10 GHz modulation bandwidth driven by a real time 16-QAM single cycle sub-carrier modulator. We use a single sub-carrier at a frequency of 2.5 GHz, and symbol rate of 2.5 GBaud with 16-QAM, yielding 4 bits/symbol and an aggregate bit rate of 10 Gbps. A clock signal of 2.5 GHz is applied to one input of a single XOR gate, while the second input is supplied with OOK data at 2.5 Gbps, to create BPSK. To create QPSK, the two outputs of the XOR gate are combined delayed in phase by 90 degrees. 16-QAM is then generated by splitting the QPSK signal and attenuating one output by 6 dB and recombining. This signal was then combined with bias and applied to the VCSEL. The VCSEL was coupled to a SMF via a lensed fiber and then to a photoreceiver with a 3 dB electrical bandwidth of ~ 7 GHz followed by a DSO80804B oscilloscope. The demodulation, equalization, and error calculation were implemented in MATLAB and done offline. Since offline processing cannot process sufficient bits within the storage of the oscilloscope an FEC with 7% overhead is assumed. A BER of $\sim 2 \cdot 10^{-3}$ was obtained

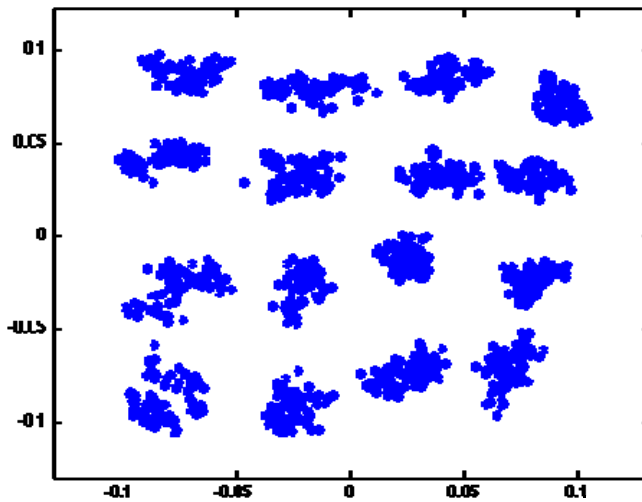


Figure 3.26 Constellation diagram of received 16-QAM single subcycle modulation.

3.5 Wavelength-Division Multiplexed Passive Optical Networks

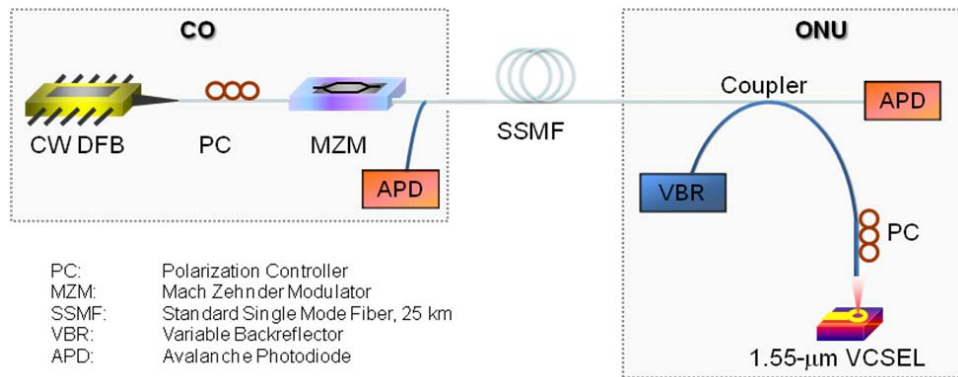


Figure 3.27 Experimental setup for feedback insensitivity in VCSEL-based PON at orthogonal polarization. [86]

Fig. 1 shows the schematic of the experimental setup. For the downstream transmitter at the central office (CO) a commercial CW DFB laser followed by a Mach-Zehnder modulator (MZM) is coupled to one port of a 1x2 3 dB power coupler with the other 3 dB port connected to a 2.5 Gb/s avalanche photo diode (APD) (upstream receiver). The coupled port is then attached to a 25 km standard single mode fiber (SSMF) after which at the optical network unit (ONU), it is connected to a 2x2 3 dB coupler. One output is another 2.5 Gb/s APD (downstream receiver) with the other output connected to a polarization controller followed by the VCSEL (upstream

transmitter). The VCSEL is a 1550-nm single-mode buried tunnel junction (BTJ) structure device with maximum output power of ~ 3 mW. Light emission is coupled by means of a lensed fiber with ~ 3 dB loss. On the last port of the ONU coupler, a variable back reflector is attached to simulate spurious reflection from the fiber system. For the series of experiments, the VCSEL is biased at 8 mA with 2 mW output power modulated at 2.5 Gb/s with NRZ 2^{23} -1 PRBS with a drive voltage of $0.7 V_{pp}$. The extinction ratio at the output of the VCSEL is 5 dB. The MZM is modulated at 2.5 GB/s 2^{31} -1 PRBS with a drive voltage of $\sim 6 V_{pp}$ with extinction ratio of 14 dB.

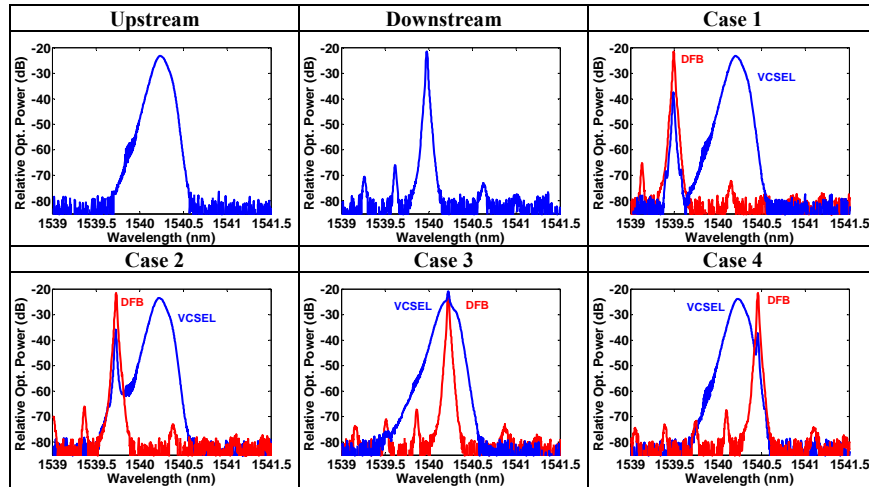


Figure 3.28 Optical spectra of upstream and downstream data with downstream DFB spectra superimposed on upstream VCSEL spectra. [86]

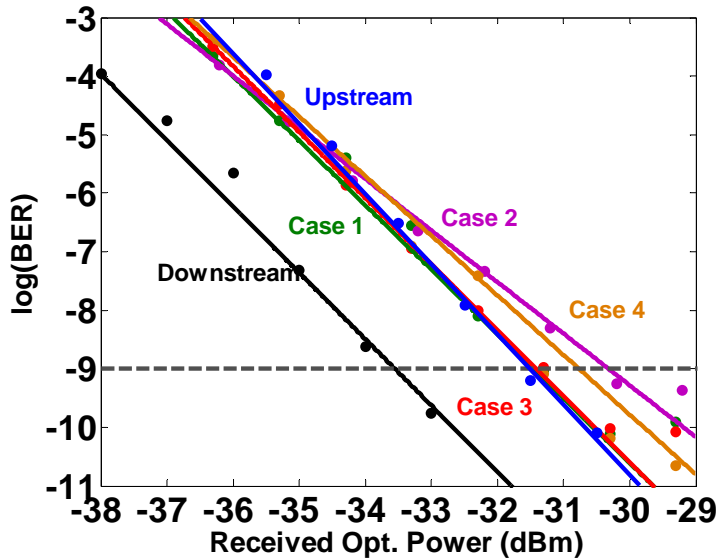


Figure 3.29 Bit error rate of each case with downstream and upstream transmission alone shown as reference. [86]

First, we set the optical feedback to -56 dB and tested the upstream data with downstream data detuned to different wavelengths with respect to the upstream wavelength. The downstream wavelength is adjusted from the blue to red side of the upstream wavelength with optical spectra shown in Fig. 2 and their corresponding bit error rate (BER) in Fig. 3. Light at the VCSEL port of the ONU couple is measured to be -18.4 dBm orthogonally polarized to the VCSEL light. Less than 1 dB of power penalty at the error-free condition ($BER < 10^{-9}$) is seen for the different downstream wavelengths, showing that the VCSEL is robust against orthogonally polarized light at different wavelengths. To test the VCSEL's intrinsic optical feedback robustness we removed the downstream data and adjusted the variable back reflector. For low optical feedback (< -15 dB) we observe there is little to no power penalty at the error-free condition compared to the no feedback case. At a feedback level of -9 dB, we experience a catastrophic reduction in bit error rate with flooring at $BER=10^{-7}$. Lastly, we combined the previous two experiments with both upstream and downstream data and adjusted the optical feedback power keeping the same detuning condition as case 2. Received power was kept constant at -18.4 dBm and BER measured at a constant optical received power of -30.5 dBm. At -16 dB backreflection the upstream data is unable to achieve error-free transmission at any received optical power.

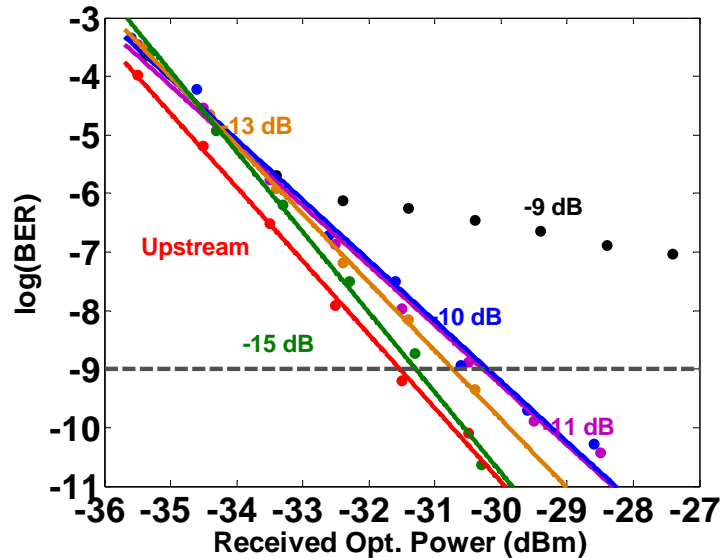


Figure 3.30 Bit error rate versus received optical power of upstream VCSEL transmission under different optical feedback powers. Critical feedback occurs at -9 dB. [86]

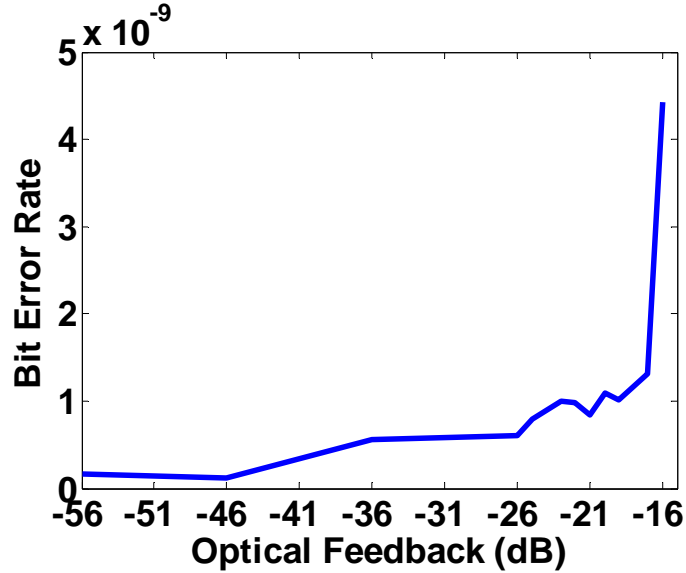


Figure 3.31 Bit error rate of upstream VCSEL transmission at -30.5 dBm received optical power with downstream transmission at various optical feedback powers. Critical feedback is -16 dB. [86]

3.5.2 Discussion and conclusion

We have successfully demonstrated a WDM-PON scheme utilizing VCSELs under orthogonal optical injection. Optical feedback tolerance of the modulated VCSEL is seen versus both downstream data as well as reflected feedback with less than 1 dB of power penalty seen. Currently, this system requires the VCSEL polarization to be known beforehand; however with the advent of polarization-selective VCSELs [3] and planar lightwave circuits with polarization diversity [4], integration of a low-cost ONU is possible. 10 Gb/s upstream data transmission with optical feedback will be presented at the conference.

In wavelength division multiplexed passive optical networks (WDM-PONs), a key requirement for the upstream laser transmitters is that their lasing wavelength does not drift too much from the assigned wavelength, so that crosstalk with other WDM channels and transmission loss at the wavelength multiplexers and demultiplexers are minimized [87]. Widely-used transmitters such as distributed feedback (DFB), distributed Bragg, and tunable lasers require wavelength stabilization circuitry making them cost prohibitive for use as optical network unit (ONU) upstream transmitters.

In this section, we demonstrate experimentally a novel WDM-PON design that utilizes optically injection-locked vertical cavity surface-emitting laser (OIL VCSEL) for isolator-less, directly-modulated ONU transmitters. OIL VCSELs are highly desirable candidates for WDM-PON due to their narrow linewidth single-mode behavior, reduced chirp and low cost of manufacture. Though previous demonstrations of OIL VCSELs for WDM-PON have shown performance improvements they have relied on circulators to isolate the injecting laser from the VCSEL adding cost and complexity [88]. For this experiment we replace the circulators with 3-dB power splitters greatly simplifying the network and reducing cost. Downstream data is

transmitted using an externally modulated DFB laser which serves a secondary role as the master laser to injection lock the ONU slave VCSEL onto the WDM grid. The wavelength locking of the VCSEL allows a specific AWG (arrayed waveguide grating) port to be assigned at the central office (CO) for each ONU without the need for complicated wavelength stabilization circuitry [89]. Optically injection locking the VCSEL also results in chirp reduction improving the transmission performance over standard positive dispersion fiber through dispersion compensation [90]. Furthermore, the VCSEL modulation is not strongly effected by the master data thus both downstream and upstream transmission can achieve good BER performance.

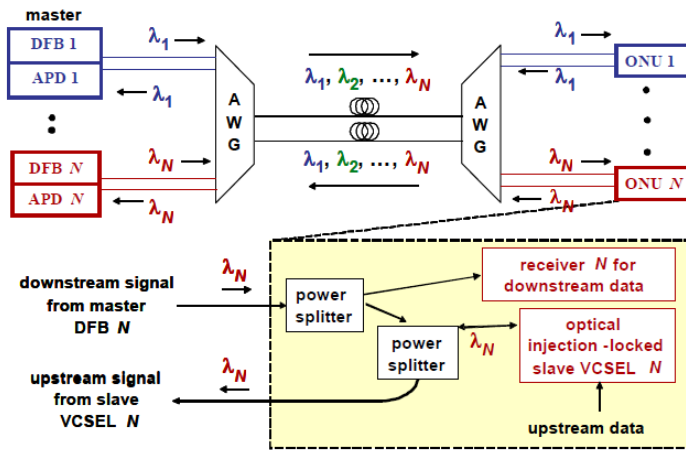


Figure 3.32 WDM-PON with OIL_VCSELs and 3-dB couplers. The slave VCSEL at each optical network unit (ONU) is injection-locked by the modulated downstream signal transmitted from the master DFB laser at the central office (CO).

3.5.3 WDM-PON with OIL-VCSELs

Figure 1 shows a schematic of a WDM-PON implemented using OIL-VCSELs and 3-dB splitters. Each master DFB at the central office can either be directly or externally modulated at a wavelength on the DWDM grid. Multiple downstream transmitters can then be multiplexed onto a single fiber and demultiplexed at the downstream site. Each ONU consists of an optical splitter which splits the optical power of the demultiplexed downstream signal to a downstream receiver and to another 3-dB coupler. The second coupler's output port is then used to injection lock the slave VCSEL with its other "input" being the splitter output from the now directly modulated OIL VCSEL, which is then multiplexed and sent upstream.

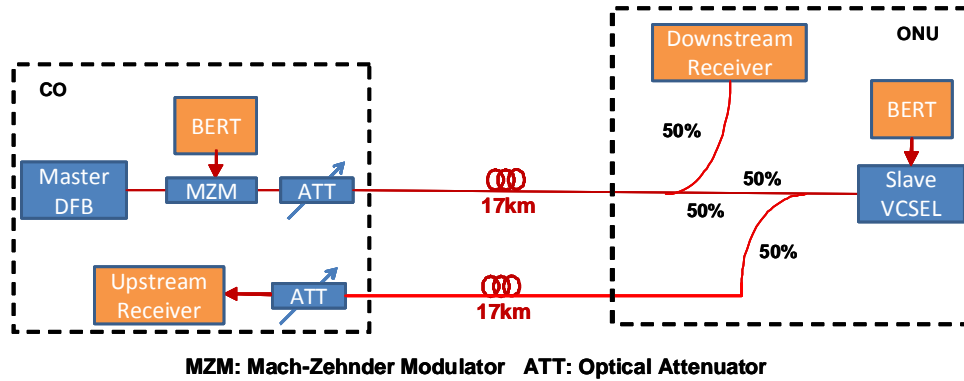


Figure 3.33 Experimental Setup for WDM-PON based on OIL VCSEL

Rayleigh backscattering of the master laser may result in performance degradation at the upstream receiver since its wavelength is the same as the slave VCSEL, so unidirectional fibers for upstream and downstream data are used to minimize the impact of this phenomenon with minimal additional cost.

3.5.4 Experiment and Results

Figure 2 shows the experimental setup for our isolator-free OIL-VCSEL WDM-PON scheme. At the CO, a DFB laser is externally modulated with 2.5 Gb/s 2^{23} -1 pseudorandom bit sequence (PRBS) non-return-to-zero (NRZ) data from a bit-error-rate test set (BERT). The modulated signal is then sent through 17 km of standard single-mode fiber (SSMF). At the ONU a 3-dB power splitter divides the signal to a 2.5 GHz APD receiver and a 3-dB coupler. The output port of the coupler is then used to injection lock a 1.55- μ m buried tunnel junction (BTJ) VCSEL with a 5- μ m aperture size optimized for high-speed modulation [5]. The other port of the coupler acts as the upstream output of the OIL VCSEL, directly modulated with a 2.5 Gb/s NRZ signal from another BERT, and is connected to another 17 km of SSMF to return to the CO. At the CO the upstream data is detected by another 2.5 GHz APD receiver. Optical attenuators are placed in front of the receivers and in the downstream link to adjust the received power and injected powers, respectively.

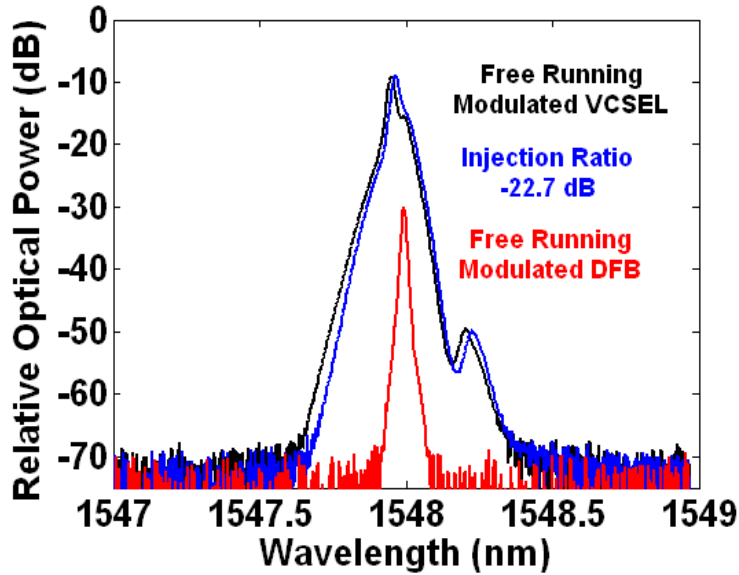
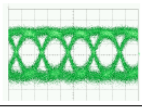
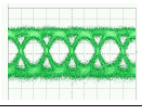
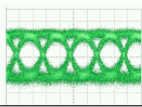
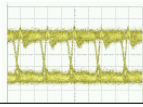
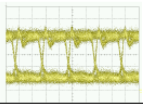
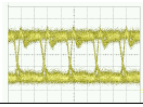


Figure 3.34 Electrical eye diagrams (green) for free running, -27.4 dB injection ratio and -31.4 dB injection ratio at error-free condition. Optical eye diagrams (yellow) prior to upstream transmission. [91]

	Free Running	-27.4 dB Injection Ratio	-31.4 dB Injection Ratio
$2^{23}-1$ PRBS			
			

Initially, we characterize the performance of the free running VCSEL directly modulated at $2^{23}-1$ PRBS to provide a baseline performance. The VCSEL is then optically injection locked by the modulated master and characterized at injection ratios of -27.4 and -31.4 dB. Eye diagrams are taken at error free conditions ($BER < 10^{-9}$) for all cases using a sampling oscilloscope. In Fig. 3 injection locking is seen when the linewidth is narrowed with respect to the free running case along with a redshift and suppression of the other polarization mode. The free running externally modulated DFB master laser is also shown in the graph. Though weak injection locking limits the locking range of the VCSEL to < 0.1 nm around its center wavelength when locked the VCSEL is stable. Detuning between the master and the slave is 0.04 nm for the case shown. Figure 4 shows the electrical and optical eye diagrams for error-free conditions for free running and at injection ratios of -27.4 and -31.4 dB for $2^{23}-1$ PRBS direct modulation on the OIL VCSEL. Electrical eye diagrams are taken at the upstream receiver, while optical eye diagrams are taken before upstream transmission. Extinction ratio is kept constant at 6.3 dB before upstream transmission.

Bit error rate curves are seen in Fig. 5 for 2^{23} -1 PRBS modulated upstream data. Fig. 5 shows reductions in necessary received power of 0.4 dB and 0.5 dB for -27.4 dB and -31.4 dB injection ratios, respectively. However, at this higher PRBS pattern dependence is observed in the flooring behavior of the curves higher than -31 dBm received power. This degradation for long monotonic sequences is caused by low frequency parasitics in the electrical probing setup.

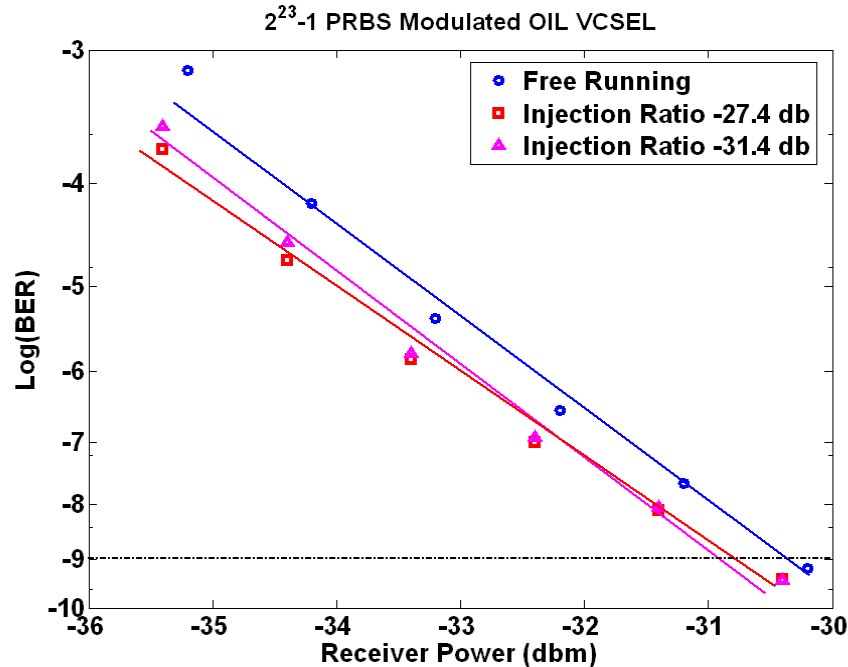


Figure 3.35 Upstream BER of 2.5 Gb/s 2^{23} -1 PRBS directly modulated OIL and free running VCSELs for 17 km transmission. [91]

3.5.5 Summary

In this section, we described a novel WDM-PON implementation that uses modulated downstream signals to injection-lock VCSELs for operation as wavelength-locked directly modulated ONU transmitters without the need for isolators. The proposed injection-locking scheme can be applied to higher bit rates as chirp reduction will then have a greater effect on dispersion compensation. Moreover, our scheme eliminates expensive components such as circulators, wavelength stabilization circuitry for ONU, and external modulator for ONU. Moreover, the wavelength matching of the slave VCSEL to the master reduces the need for active temperature management allowing for the possibility of uncooled operation at the ONU site. These characteristics make isolator-free OIL VCSEL WDM-PON an excellent candidate for low-cost, broadband FTTx applications.

Due to their low cost and high speed, vertical-cavity surface-emitting lasers (VCSEL) are the workhorse of short distance optical links. However, for next generation 100G optical Ethernet and millimeter-wave analog fiber links, higher modulation speeds and longer transmission distances are needed. Moreover, the need to do processing in the optical domain will become a necessity as high frequency electronics are complex and bulky. Optical injection locking (OIL) has been shown to solve the former issue by increasing the modulation bandwidth

by tenfold. OIL has also been shown to create data pattern inversion by interference effects, helping with dispersion compensation to allow for longer reach.

3.6 Signal Processing

3.6.1 Motivation

Ultra-wideband (UWB) transmission has attracted interest for short-range, high-throughput wireless and sensor networks due to its immunity to multipath fading, high data rates and low power consumption, however their generation using electronic methods has proven difficult. Generating UWB signals optically has previously been demonstrated using either external phase modulators or semiconductor optical amplifiers through phase-to-intensity conversion. Moreover, optical data-format conversion and clock recovery are indispensable functions for network diagnostics and signal processing, but are currently realized through various nonlinear elements.

In this section, we propose and demonstrate multiple signal processing operations utilizing an optically injection locked single or multi-transverse mode VCSEL, showing UWB-monocycle generation, data-format conversion, and clock recovery. The key new element for this system is the addition of a tunable interferometer to selectively filter the frequency chirp after OIL. Polarity-switchable UWB monocycles are generated with a 5.1 GHz center frequency and a fractional bandwidth of 129%. Rising and falling edge detection leads to NRZ to RZ format conversion using this method. Also, a 10-GHz clock tone with 35 dB suppression ratio is also recovered from a 10-Gb/s NRZ input with PRBS15.

3.6.2 Concept and Working Principle

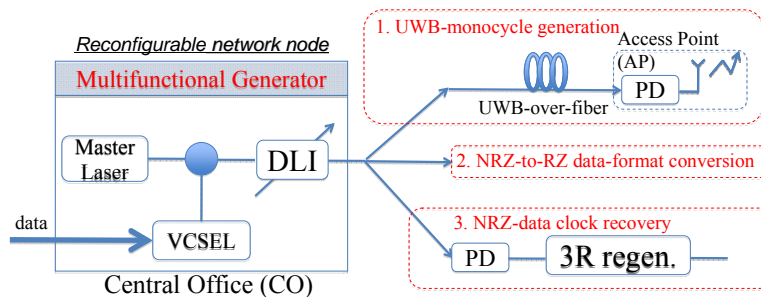


Figure 3.36 Concept of multifunctional generator using optical injection-locked (OIL) VCSEL followed by a delay-line interferometer (DLI). Three unique and reconfigurable functions are generated by utilizing the adjustable-chirp from the OIL-VCSEL and subsequent tunable filtering.[71]

3.6.3 Experimental Setup and Time-Resolved Chirp after OIL

The experimental setup is shown in Fig. 2.41. A DFB laser serves as the master to injection-lock a 1.55- μm single or multi-transverse mode VCSEL. A 10 Gb/s PRBS15 NRZ-data signal directly modulates the VCSEL at an optimized bias and driving voltage. A 10-GHz all-fiber delay-line interferometer (DLI) is placed after the OIL-VCSEL to serve as a tunable filter. An Advantest Q7606B chirp-form analyzer is used in conjunction with a sampling oscilloscope to obtain time-resolved chirp and intensity waveforms. To measure the output, a 10 GHz photodiode connected to a radio frequency spectrum analyzer are used for the varying functions.

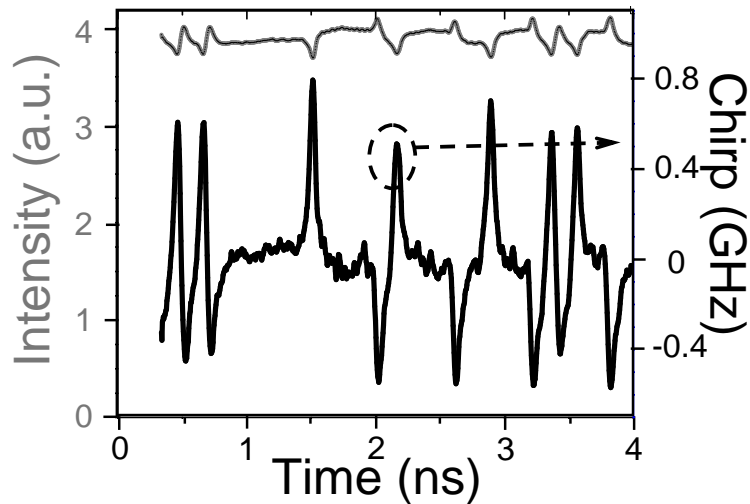


Figure 3.37 Time-resolved frequency chirp measurement of OIL-VCSEL under the transition state.[71]

3.6.4 NRZ-to-RZ format conversion/Clock recovery

Detuning the DLI either way by 0.06 nm from the center frequency of the OIL data signal, the center frequency components of the original transition state signal can be suppressed, and chirped components can be enhanced. Fig. 3.33 (a) and (b) show the detection of either the rising edge or the falling edge of the original data signal, respectively using this method. Fig. 3.33 (c) shows the rising edge detected eye diagram, which is an RZ data format compared to the original NRZ eye diagram, demonstrating the NRZ-to-RZ format conversion capabilities of OIL.

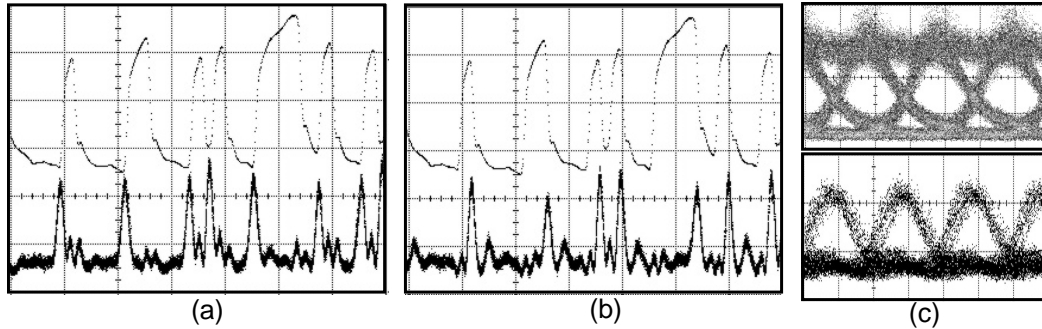


Figure 3.38 (a) Rising-edge detection (b) Falling-edge detection (c) eye diagrams of NRZ and format converted RZ from the rising-edge detection. [71]

Since the DLI is spectrally periodic, if the signal is placed at the notch of the DLI spectrum, both the negative and positive chirped components are enhanced while the center frequency is suppressed. This can then be utilized to detect both the rising and falling edges of the original 10-Gb/s NRZ data pattern as shown in Fig. 3.34 (a), with the corresponding RF spectrum shown in Fig. 3.34 (b), containing a 10-GHz recovered clock with > 35 dB suppression ratio and 0.3 MHz tone spacing, matching the original 10-Gb/s data with $2^{15}-1$ PRBS.

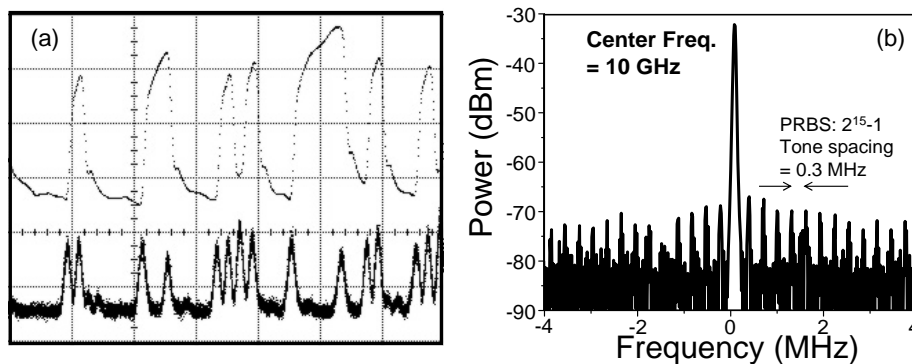


Figure 3.39 (a) Edge detection of both rising and falling edges. (b) RF spectrum showing the recovered 10-GHz clock and the 0.3 MHz tone spacing. [71]

3.7 Optical Logic Gates

In this section, we focus on using OIL induced data pattern inversion to create an optical NOT gate. By injecting master light into a modulated slave VCSEL we are able to switch from a state where the optical data pattern is the same as the electrically modulated signal to one that is inverted. Switching from a non-inverted to inverted state based on changing the injection ratio and based on wavelength detuning ($\Delta\lambda = \lambda_{\text{Master}} - \lambda_{\text{Slave}}$) are both demonstrated. Short switching times are seen when actively switching from non-inverted to inverted data while optically

injection locked. We also propose a structure to create NAND and NOR gates for optical computation based on this phenomena.

3.7.1 Theory and Experimental Setup

In Fig. 1, the OIL reflection model schematic is shown [3]. The field of the master laser is shown by E_{inj} , of which the >99% is reflected, denoted by E_r . E_s is the cavity output governed by the OIL rate equations. The phase difference between E_r and E_s creates destructive interference at the output which leads to the data inversion previously reported. By changing the wavelength detuning and injection ratio, the phase of E_s can be altered to create non-inverted and inverted data patterns.

Figs. 2-4 show the schematics of three experimental setups to test data inversion by parameter change. Fig. 1 shows the basic setup where a high power (40 mW) CW distributed feedback master laser injection locks the modulated VCSEL via a circulator. In this setup the wavelength of the master is detuned versus the wavelength of the slave laser via temperature tuning creating the switch between the non-inverted and inverted data patterns. Fig. 2 shows the master laser being externally modulated by a Mach Zehnder modulator before injection locking the modulated slave VCSEL. In this case, the injection ratio modulation is used to flip the data pattern. Lastly, in Fig. 3 we realize an all-optical NOT gate configuration where the VCSEL is biased for CW operation, and two masters are used one operating in CW to set the threshold inversion condition and the other externally modulated to provide the injection ratio change for switching.

3.7.2 Results

For the injection locking experiment in Fig. 1, the VCSEL is biased with ~1 mW output power. The master laser, set at a fixed output power, is then wavelength detuned with respect to the free running VCSEL wavelength. Starting from small positive detuning, the slave laser is locked on polarization mode #1 and a non-inverted data pattern is seen (Fig. 4). Moving to a larger positive detuning, a transient state is reached where the destructive interference dominates, after which an inverted state is reached showing the data pattern flipped.

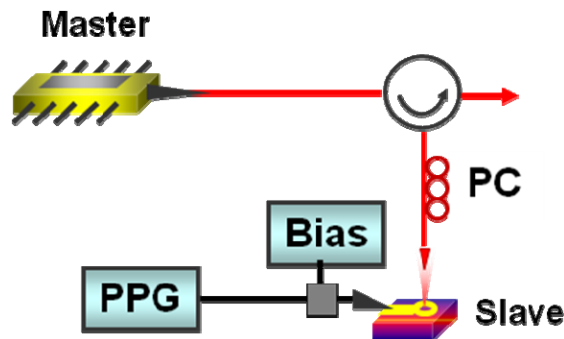


Figure 3.40 OIL-based NOT gate based on wavelength detuning

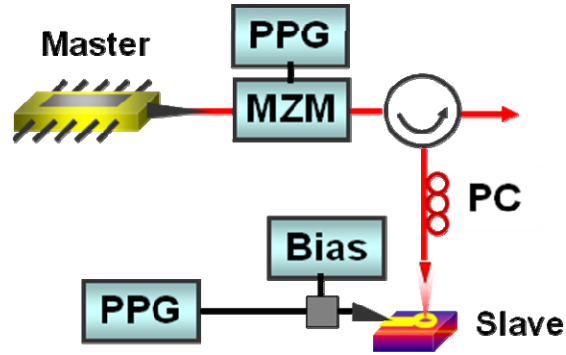


Figure 3.41 OIL-based NOT gate based on injection ratio change

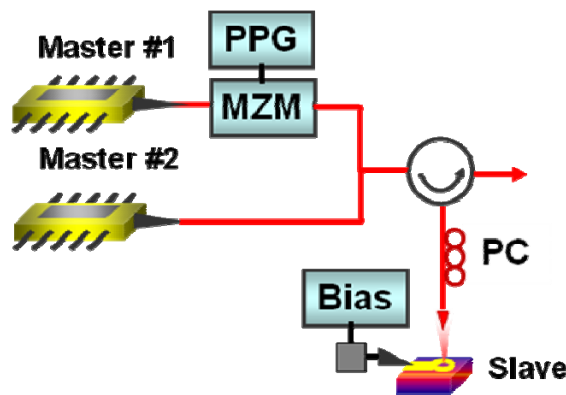


Figure 3.42 All-optical NOT gate based on OIL injection ratio change

Detuning further, the master now locks on polarization mode #2 and a non-inverted data pattern is seen again. Transient and inverted states are also seen for this second polarization mode by increasing the positive detuning further.

Using the setup in Fig. 3, the injection ratio is modulated causing the VCSEL bit pattern to switch from non-inverted to inverted at high frequencies. In Fig. 6, we see the bits at the lower injection ratio (lower intensity level) follow the free running pattern but as the injection ratio increases the intensity level shifts up and the bits invert while still maintaining a reasonable extinction ratio. From this data we also can observe that the switching time is less than 100 ps. Moreover, this feature may allow for multi-level amplitude modulation to increase the spectral efficiency for OIL VCSELs.

Setups in Fig. 2 and 3 require the VCSEL to be modulated making these systems an electro-optical NOT gate. In Fig. 4 we implement an all-optical NOT gate with two master lasers (one modulated, one CW) and a CW VCSEL. The modulated master acts as the signal laser while the CW master sets the state of the output based on wavelength detuning. Again, a switch from non-inverted data to a transition state to inverted data is seen with this all-optical setup. To increase the speed of this gate, a modulator may be added to the CW master arm. A NAND-gate can then be created by changing one master arm to two modulated master lasers and a coupler to form an AND gate cascaded with the NOT gate.

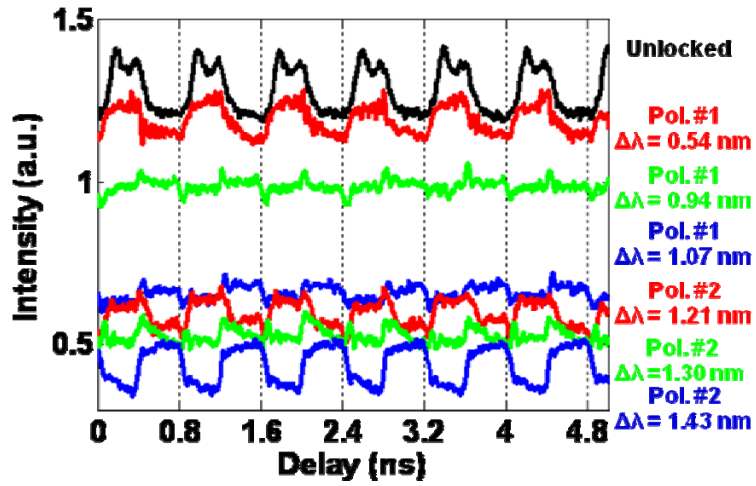


Figure 3.43 Switching of inversion by injection ratio modulation of an OIL VCSEL

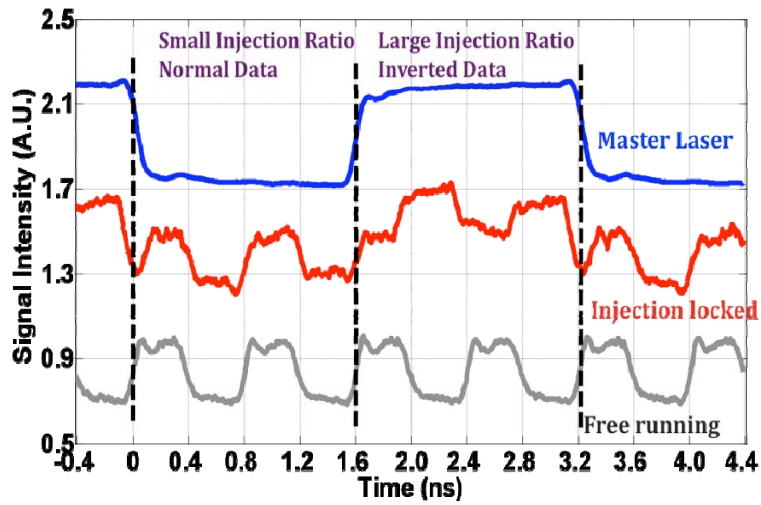


Figure 3.44 Switching of inversion by injection ratio modulation of an OIL VCSEL

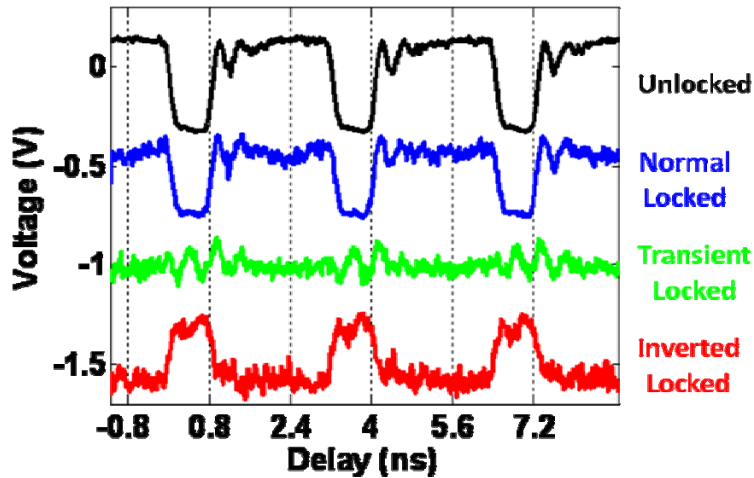


Figure 3.45 All-optical NOT-gate by wavelength detuning of master #2

3.7.3 Conclusions

We have successfully demonstrated a NOT gate by both wavelength detuning and changing injection ratio, as well as demonstrated a switch with switching time of <100 ps. An all-optical NOT gate was also demonstrated with the ability to be modified into a NAND gate.

3.8 Summary

In conclusion, we have demonstrated that optical injection locking of VCSELs can improve performance in digital communication systems. By reducing chirp and inverting data, chromatic dispersion can be mitigated and fiber transmission distance increased. Moreover, phase modulation of VCSELs can be achieved allowing for more advanced modulation formats. This can lead to more spectrally efficient communications and other interesting applications such as optical logic gates using a VCSEL.

Chapter 4 Conclusion

In summary, optical injection locking of VCSELs can be applied to many different telecommunication applications to improve performance and to investigate device dynamics. Previous experiments have shown only isolated performance improvements, however this thesis has theoretically and experimentally shown that optical injection locking can be applied at the system level. Resonance frequency enhancement was shown for both single and multi-transverse mode VCSELs showing over 10 times improvement for each. This allows for millimeter-wave applications to use VCSELs, which were demonstrated in a radio over fiber system transmitting 4 Gb/s at a 60 GHz carrier frequency. Another application demonstrated was an optoelectronic oscillator at 20 GHz showing extremely low phase noise comparatively to electronic oscillators. For digital communications, the reduction in frequency chirp and inversion of the bit pattern by optical injection locking was used to extend fiber transmission of both single and multimode VCSELs at 10 Gbps. These system experiments as well as others have shown optical injection locking of VCSELs to be a viable method for post-fabrication performance improvement.

Looking forward for optical injection locking, there are numerous additional areas where it can improve performance as well as ways its implementation can be enhanced. Currently, optical injection locking still relies on a discrete master laser and VCSEL coupled via a fiber, which makes it bulky and inefficient for many applications. Research into integrating both on to a single chip with integrated isolator would make it a stronger candidate for deployment. Moreover, optimizing the reflectivity of the slave laser would allow for improved performance as well. The main area where optical injection locking can greatly benefit systems applications is on the analog side. As digital communications move to more multi-level modulation formats, and radio over fiber systems move to the millimeter wave, increased frequency response and lower noise are both required, and both are enhancements that optical injection locking can provide. Other areas that have not fully been explored are polarization multiplexing based on injection locking and looking at what the theoretical limits of strong injection locking are. Though this thesis covers many different optical injection locking scenarios there are still many yet to be explored.

Appendix 1 Metal Nanoparticle and Quantum Dot Metamaterials for Near Resonant Surface Plasmon Waveguides

Introduction

Recently there has been a surge of interest in materials with negative refractive index. A sufficient condition for such a material is that ϵ as well as μ are negative [92]. However, even materials with only negative ϵ are very interesting since they offer the possibility of increasing the integration density in photonic lightwave circuits [93]. In fact, to increase integration further, it is necessary to find a successor to the current silicon nanowire technology, which has enabled the recent progress in integration density [94], [95].

One can show that the minimum field extension for a planar silicon waveguide in air is ~ 300 nm, with a wavelength in the medium of ~ 500 nm, at a vacuum wavelength of $1.55 \mu\text{m}$. Thus, any attempts in nanophotonics should be below these values, as measured in proportion to the relevant vacuum wavelength. Now, such successors could be metals, since they offer negative ϵ at optical frequencies, however, their accompanying dissipative losses are forbiddingly high for many, albeit not all, applications. By creating a planar structure, where the ϵ is engineered to be negative on one side and positive ϵ of nearly equal magnitude on the other side, i.e. a near resonant structure, with low losses in both cases, high lateral spatial confinement as well as short propagation wavelengths along the interface, much shorter than the vacuum wavelength, can be obtained [96]. This can also be used for high confinement channel waveguides [97] and opens avenues for a wide range of novel structures and applications based on dense lateral and longitudinal integration of waveguide devices. But flexibility in the employed wavelength and other parameters requires the use of novel materials, where the metamaterial of this section is one possibility. Thus, this section aims at elucidating the prospects for such planar waveguide structures, employing metamaterials rather than existing materials.

In this section we analyze a metamaterial based on cubically arranged spherical metal, notably silver, nanoparticles embedded in a dielectric for controllably generating a range of negative or positive ϵ to be used for nanophotonic integrated photonic circuits and assess the associated dissipative loss [98–100]. The influence of different material parameters such as nanoparticle fill factor, ϵ of the host medium as well as the frequency of operation are analyzed. As an example silver is used and modeled beyond the Drude model, and a comparison with bulk silver is made. The gain required to obtain a low loss medium using quantum dots or general two-level systems is analyzed and requirements on such systems given. Finally, we use the results to create near resonant (ϵ on both sides nearly equal but of opposite signs, ideally with both $\epsilon''=0$) planar surface plasmon waveguides having high field confinement as well as high effective indices.

It should be mentioned that we analyze structures where we maximize field confinement as well as effective indices, while trying to keep the losses to reasonable values. There is little difficulty in having low plasmonics losses if the optical field is mainly confined to a lossless dielectric.

All results pertain to room temperature unless otherwise stated.

ENGINEERABLE ϵ BASED ON METAL NANOPARTICLES EMBEDDED IN A DIELECTRIC

We analyze a metamaterial with metal nanoparticles embedded in a dielectric. The metal particles, taken as silver here, are conventionally modeled by the two-parameter (plasma frequency, ω_p , and electron collision frequency, β) Drude model. This model is conceptually simple and gives good agreement with experimental data over a limited wavelength range, however, more accurate modeling and optimization require better representation of the experimental data of silver, and we employ the data in [101].

We further employ spherical, cubically arranged nanoparticles to generate an isotropic ϵ and calculate the complex macroscopic dielectric constant ϵ_{MAC} by using the expressions for the polarizability α of a spherical metallic nanoparticle in a surrounding medium and the Clausius-Mossotti (CM) relation. The reason for using this simplified model instead of a more accurate modeling of metamaterials, taking into account nanoparticle interactions, is the reasonable accuracy of the method we use, as treated in this reference; this allows optimizations without extensive computational efforts, which could obscure the general features we wish to identify.

Thus:

$$\alpha = V \frac{\epsilon_m / \epsilon_d - 1}{1 + d(\epsilon_m / \epsilon_d - 1)} \quad (\text{A.1})$$

Here V is the volume of the nanoparticle, and ϵ_m, ϵ_d are the dielectric constants of the nanoparticle material (complex) and of the surrounding medium, respectively and $d = 1/3$ is the depolarization factor for spheres. It is assumed that the radii of the spheres are much smaller than the wavelength in the medium. The dipole moment p is given by $p = \alpha \epsilon_0 E$

We can thus derive the relation between the macroscopic dielectric constant and the microscopic polarizability:

$$\frac{\epsilon_{MAC} / \epsilon_d - 1}{\epsilon_{MAC} / \epsilon_d + 2} = \frac{\alpha}{3V_{cell}} \quad (\text{A.2})$$

(Or more generally

$$\frac{\varepsilon_{MAC} / \varepsilon_d - 1}{\varepsilon_{MAC} / \varepsilon_d + 2} = \sum_j \frac{\alpha_j N_j}{3} \quad (\text{A.3})$$

if different nanoparticles j of concentrations N_j are hosted in the dielectric with dielectric constant ε_d).

Here ε_{MAC} is the macroscopic dielectric constant and V_{cell} is the volume of a cell generated by an assumed cubically arranged regular array of Ag nanoparticles. The cubic arrangement is assumed in order to make this form of the CM relation valid. It should be noted that the validity of CM rests on the wavelength in the medium being much larger than the fictive Lorentz sphere used to derive the CM relation, and the radius of this sphere should in turn be much larger than the dipole size and separation. Further, it should be noted that in structures where the metamaterial is interfaced to another material, interface effects are not explicitly taken into account in the CM relation used.

We study below $\varepsilon'_{MAC}, \varepsilon''_{MAC}$ vs. nanoparticle fill factor η , ε_d of the embedding dielectric and wavelength.

From Equation A.1 and A.2 we derive (for spherical particles in a cubic arrangement):

$$\varepsilon_{MAC}' = \Re \left[\frac{\varepsilon_m (1 + 2\eta) + 2\varepsilon_d (1 - \eta)}{\varepsilon_m (1 - \eta) + \varepsilon_d (2 + \eta)} \right] \cdot \varepsilon_d \quad (\text{A.4})$$

$$\varepsilon_{MAC}'' = \Im \left[\frac{\varepsilon_m (1 + 2\eta) + 2\varepsilon_d (1 - \eta)}{\varepsilon_m (1 - \eta) + \varepsilon_d (2 + \eta)} \right] \cdot \varepsilon_d \quad (\text{A.5})$$

Equations A.4 and A.5 are related by the Kramers-Krönig relations. Figures 4.1 and 4.2 show the real and imaginary parts of the macroscopic dielectric constant for an embedding dielectric constant $\varepsilon_d = 5$ for various fill factors η , smaller than or equal to .5. At the fill factor $\frac{\pi}{6}$ spheres touch and multipole effects become strong [102]. Figures 4.3 and 4.4 show the corresponding data, now with the fill factor fixed at .06 and as a function of ε_d .

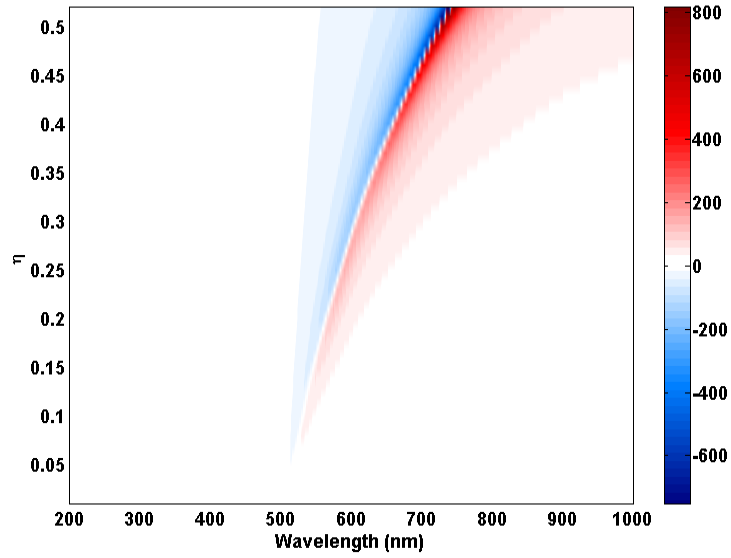


Figure 4.1 Real part of dielectric constant of the metallodielectric metamaterial plotted as a function of wavelength and fill factor for a background dielectric constant of 5.

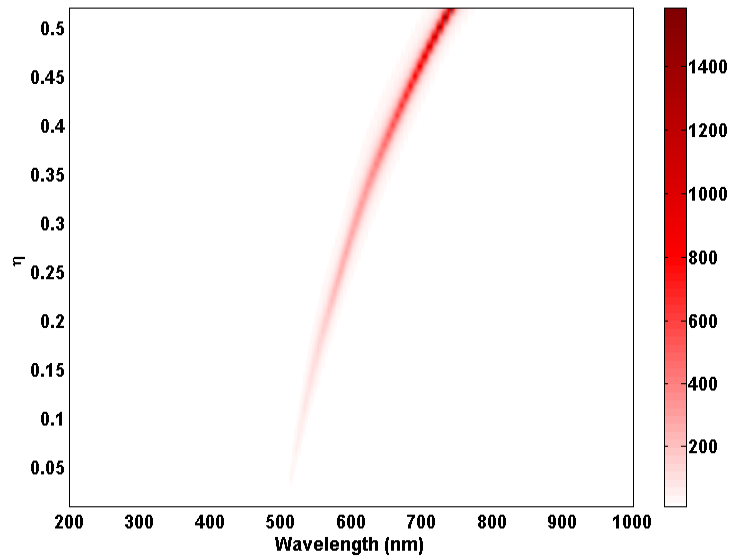


Figure 4.2 Imaginary part of dielectric constant of the metallodielectric metamaterial plotted as a function of wavelength and fill factor for a background dielectric constant of 5.

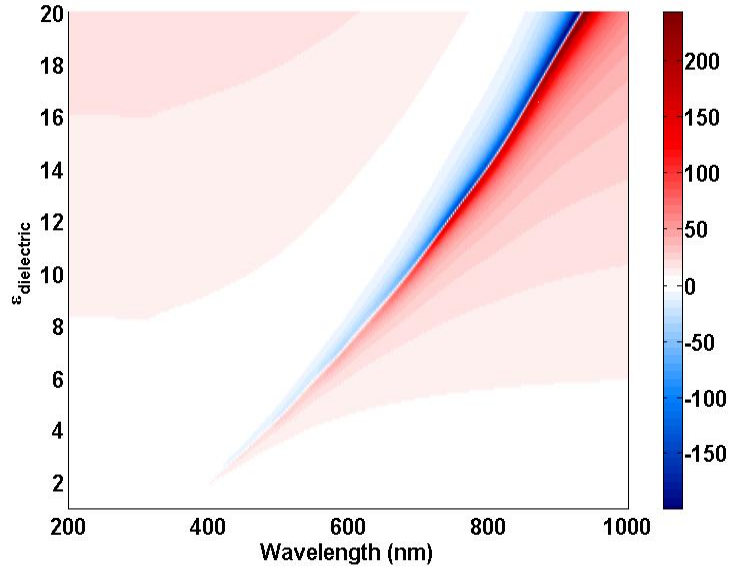


Figure 4.3 Real part of dielectric constant of the metallodielectric metamaterial plotted as a function of wavelength for different background dielectric constants.

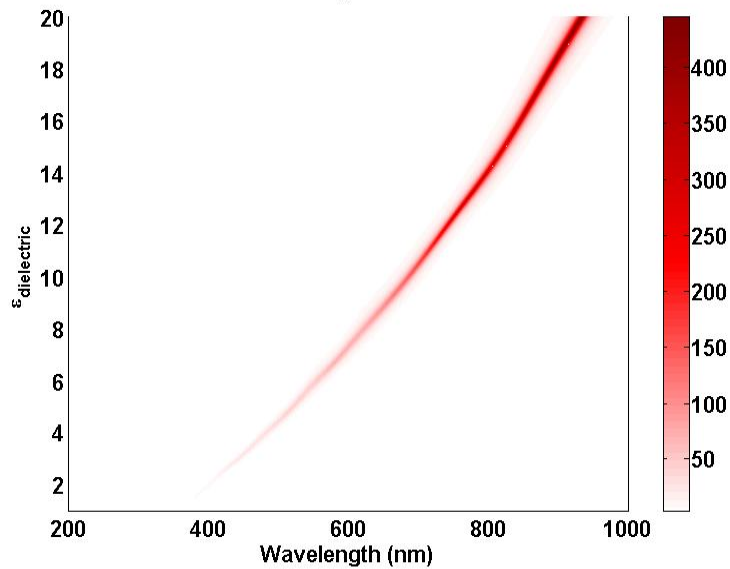


Figure 4.4 Imaginary part of dielectric constant of the metallodielectric metamaterial plotted as a function of wavelength for different background dielectric constants.

The strong resonances in Figures 4.1-4.4, analogous to the polarization catastrophe in ferroelectrics, are a consequence of the way the CM relation can generate a polarization even in the absence of an applied field. The large values at resonance lack physical significance, since

nonlinear effects will limit the dielectric constants. We note, as expected, that larger fill factors and dielectric constants of the dielectric lead to stronger resonances.

We can employ the above figures to find operating points where $|\epsilon'_{MAC}|$ is reasonably large and ϵ''_{MAC} as low as possible. Thus Table 4.1 shows one such operating point.

Material	ϵ'	ϵ''	Fill	Host ϵ
Metamaterial "dielectric"	5.0276	.3252	.27	19.8
Metamaterial "metal"	-5.0015	.4402	.52	16.3
Ag	-12.9189	.4306	NA	NA
SiO ₂	2.1314	0	NA	NA

Table 4.1 Values of macroscopic dielectric constant at 550 nm wavelength, optimized with respect to ϵ_{MAC} , with the condition that $|\epsilon_{MAC}|$ should be ~ 5 ,

It is interesting to note that the bulk silver data are comparable to those of the metamaterial, in spite of the fact that the silver is "diluted" in the metamaterial. However, silver and dielectrics by themselves, as analyzed in many publications cannot in general produce the near resonance condition for high field confinement, nor give the metamaterial flexibility.

The role of the ϵ_{MAC} can be seen by the expression for the temporal decay constant of the electromagnetic energy

$$\frac{1}{\tau_E} = \frac{\omega \epsilon_{MAC}'' \epsilon_0 EE^*}{.5(\text{Re}(\frac{d(\omega \epsilon_{MAC})}{d\omega}) \epsilon_0 EE^* + \mu_0 HH^*)} \quad (\text{A.6})$$

where $\frac{1}{\tau_E}$ is the EM energy decay rate and $\mu_0 HH^*$ can be replaced by $\epsilon_0 |\epsilon_{MAC}| EE^*$. This

expression is valid when ϵ_{MAC}'' is much smaller than ϵ_{MAC}' .

This also shows that for the metamaterials, the decay times are on the order of the oscillation period of the light, making the losses large even for this optimized cases.

Properties of Metamaterials with Ag Nanoparticles and Amplifying Two Level Systems (Quantum Dots) in a Dielectric Host

In this section, we combine the silver nanoparticles from the previous section with amplifying nanoparticles, assumed to be hosted in the same dielectric medium as the silver ones. As long as the negative permittivity and gain cannot be realized in the same nanoparticle, an interesting challenge, the metal and amplifying nanoparticles will be separated. It is assumed that the two level systems are by some method totally inverted.

The linear susceptibility of a fully inverted two level system (i.e. with gain) such as a quantum dot (QD) is:

$$\chi'' = -\frac{1}{1+T_2^2\Delta^2} \frac{T_2\rho^2 N_a}{\varepsilon_0\hbar} \quad (\text{A.7})$$

$$\chi' = \frac{\Delta T_2}{1+T_2^2\Delta^2} \frac{T_2\rho^2 N_a}{\varepsilon_0\hbar} \quad (\text{A.8})$$

Here T_2 is the transverse relaxation time of the two level medium, Δ , deviation from resonance, in rad/s, ρ , the dipole moment, and N_a , the quantum dot spatial density, with all dots or atoms assumed inverted.

From this we can derive the out of phase (amplifying) component of the dipole moment at resonance:

$$p = -i \frac{\rho^2 T_2}{\hbar} E \quad (\text{A.9})$$

And since p is given by $p = \alpha\varepsilon_0 E$, we can calculate

$$\alpha = -i \frac{1}{\hbar\varepsilon_0} \frac{\rho^2 T_2}{\hbar} \quad (\text{A.10})$$

i.e. we have at resonance a purely imaginary polarizability.

Equation A.10 can now be used in Equation A.2 to calculate the macroscopic dielectric constant, the imaginary part of which describes gain/loss. V_{cell} is the cell size of the quantum dot structure. For the two level gain medium we use in our simple model as examples the parameters [103–105] $N_a \leq 10^{23} m^{-3}$; $\rho \approx .8nm \cdot e$; $T_2 \approx 100fs$. 100 fs corresponds to a line width of 6 meV at a wavelength of 550 nm, used below. Using the above data ($T_2=100$ fs) we obtain $\chi'' = \varepsilon'' = -0.03$. This should be compared to the data in Table 1, which for negative ε_{MAC} are an order of magnitude larger. We now turn to a more complete calculation of the properties of the metallodielectric QD structures.

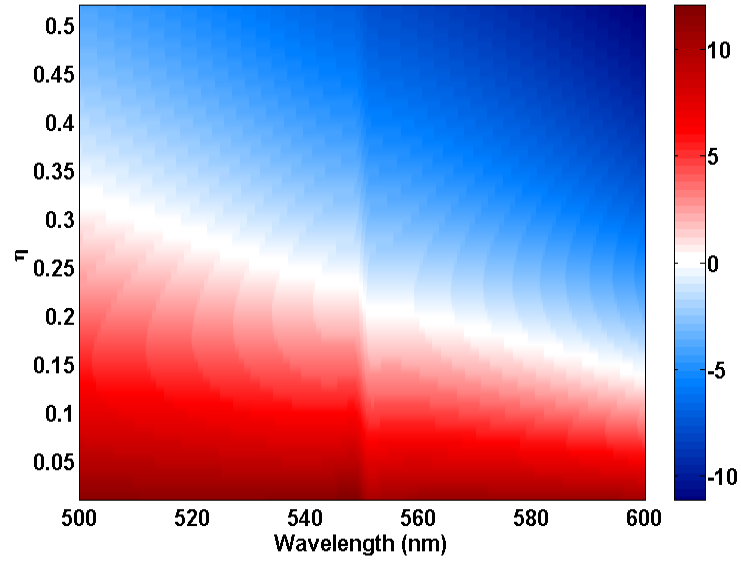


Figure 4.5 Dielectric constant of the metallodielectric quantum dot metamaterial plotted as a function of wavelength for different fill factors (η) at a constant background dielectric constant ($\epsilon=12$)

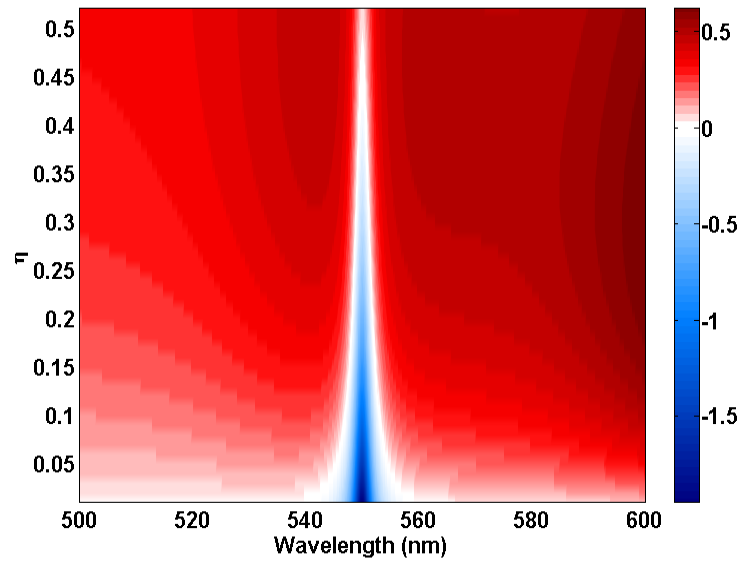


Figure 4.6 Dielectric constant of the metallodielectric quantum dot metamaterial plotted as a function of wavelength for different fill factors (η) at a constant background dielectric constant ($\epsilon=12$).

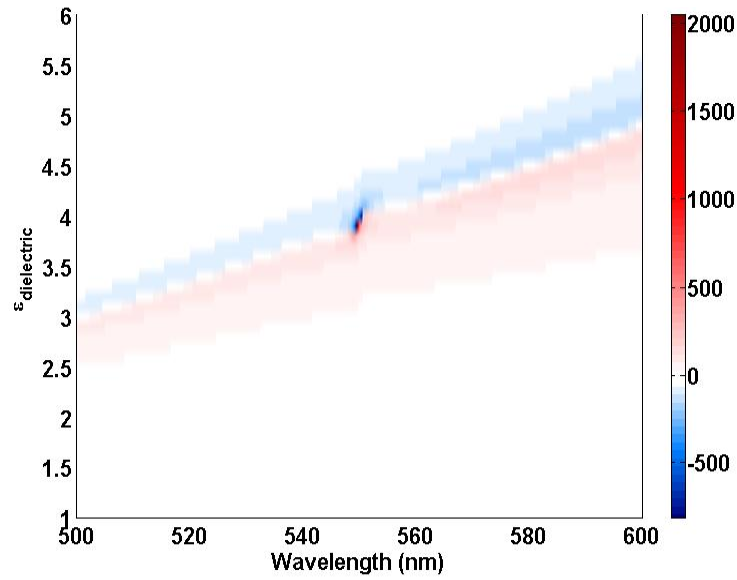


Figure 4.7 Dielectric constant of the metallodielectric with two-level system metamaterial plotted as a function of wavelength for different background dielectric constants at a constant fill factor ($\eta=0.3$)

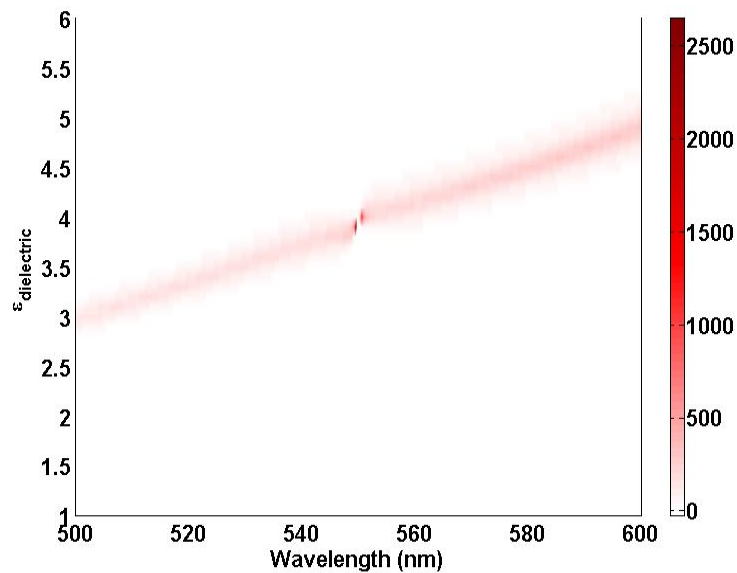


Figure 4.8 Imaginary part of dielectric constant of the metallodielectric with two-level system metamaterial plotted as a function of wavelength for different background dielectric constants at a constant fill factor ($\eta=0.3$).

Figures 4.5-4.8 show data corresponding to Figures 4.1-4.4. Figures 4.5 and 4.6 show the real and imaginary parts of the macroscopic dielectric constant vs. wavelength and with the Ag

fill factor as a parameter, and for QD data as above with $T_2=100$ fs. The strong resonances due to the Ag nanospheres in the absence of QDs are modified by the presence of the QDs,

Figures 4.7 and 4.8, show real and imaginary parts of ϵ_{MAC} vs. wavelength with host dielectric constant as parameter. In this case, for e.g. an Ag fill factor of 0.3, one can obtain around -2 and -0.2 for real and imaginary parts of ϵ_{MAC} , respectively. The imaginary part is obviously larger in magnitude than the one calculated above (-0.03), but that was based on vacuum, with no local field correction. It turns out that the higher the dielectric constant of the embedding medium, the more negative the ϵ_{MAC} " (implying gain), within a small bandwidth, and that the "resonant" nature of the CM relation with negative permittivity nanoparticles actually assists in producing higher gain. Thus, it appears does indeed appear possible to generate, at least in theory, a negative ϵ'_{MAC} as well as low loss or gain for the parameters listed above.

Near Resonant Plasmonic Planar Waveguides Based on Metamaterials with Positive and Negative Dielectric Constants

We can now use the results from above to investigate the properties of planar near resonant waveguides, potentially important elements in photonic circuits, given that the losses can be compensated to some extent. We have for such waveguides:

$$\beta_z^2 = k_0^2 \frac{\epsilon_{MAC2} \epsilon_{MAC1}}{\epsilon_{MAC2} + \epsilon_{MAC1}} = \left(\frac{2\pi}{\lambda_{eff}} \right)^2 \quad (\text{A.11})$$

$$\gamma_{MAC1}^2 = -k_0^2 \frac{\epsilon_{MAC1}^2}{\epsilon_{MAC2} + \epsilon_{MAC1}} \quad (\text{A.12})$$

$$\gamma_{MAC2}^2 = -k_0^2 \frac{\epsilon_{MAC2}^2}{\epsilon_{MAC2} + \epsilon_{MAC1}} \quad (\text{A.13})$$

These equations relate the effective index $\beta_z \equiv N_{eff} k_0$ (Equation A.11); confinement factors (inverse of 1/e penetration depth in the metamaterials) $\gamma_{MAC1}; \gamma_{MAC2}$, Equations A.12 and A.13, to the macroscopic dielectric constants. Making the dielectric constants nearly equal but with opposite signs in the two media (and with small imaginary parts) will lead to very large values for effective index (enabling e.g. short resonators) and confinement (close laterally packed waveguides), i.e. the desired lateral and longitudinal confinement, leading to dense integration. Unfortunately, it will also lead to losses per unit length that increase dramatically as this integration density is increased. However, for resonators, this is not an issue since the length will also decrease, the decisive parameter is the ϵ_{MAC} " of Equation A.6. Thus there is an interest in compensating these losses e.g. by gain, and we use the results above for this purpose. (The increase in losses per unit length can be understood from the fact the group velocity approaches 0 at the resonance, hence the temporal decay time corresponds to a vanishingly small propagation length, giving a very high loss coefficient, per unit length.) It should also be pointed out that the conditions for resonance are very far from being fulfilled in e.g. an Ag-dielectric system, but can more closely be met in a metamaterial system with gain as discussed here.

First, looking at the hypothetical case of lowering the ϵ'' of silver from its intrinsic value down to 0, we see that propagation length exponentially increases for both a bulk Ag-SiO₂ plasmonic waveguide and the metamaterial surface plasmon waveguides (Figure 4.9 and 4.10). However, the confinement of the bulk Ag-SiO₂ shows no improvement in lateral confinement, while the metamaterial shows tighter confinement on both the metal and dielectric sides. Now, adding gain to the system in the form of a two-level system, e.g. CdSe quantum dots (Figures 4.11 and 4.12), we see that propagation lengths can be greatly increased close to the two-level system resonance, while lateral confinement is still better than the Ag-SiO₂ reference case.

Other publications have also investigated amplification [106]. In that publication, however, conclusions are drawn that an amplification of $7 \times 10^4 \text{ cm}^{-1}$ can be obtained; however, this is a material gain and not the macroscopic gain, which is, as evidenced from, very much lowered by the confinement factor. The numbers presented in this section are more realistic from that point of view in that the macroscopic ϵ_{MAC}'' is calculated. As expected, balancing loss with gain gives high lateral confinement as well as long propagation lengths, Equation A.11-A.13.

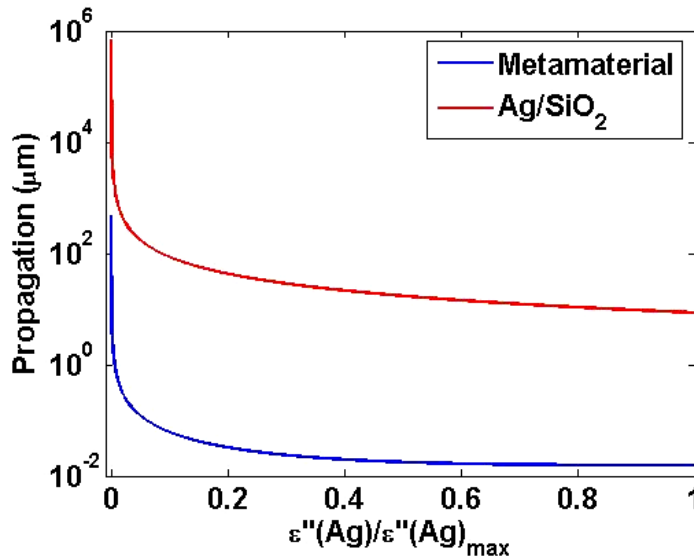


Figure 4.9 Propagation length for metallodielectric metamaterial surface plasmon waveguide plotted versus Ag ϵ'' without QDs. As ϵ'' reduces towards 0, the propagation length increases exponentially.

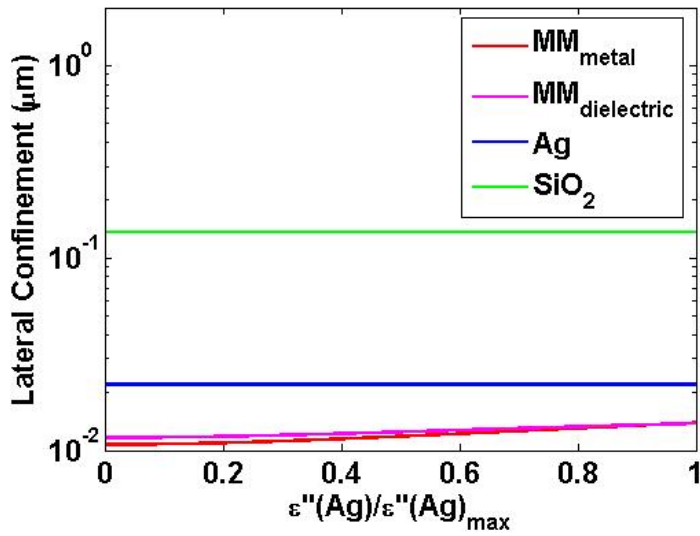


Figure 4.10 Confinement for metallodielectric metamaterial surface plasmon waveguide plotted versus Ag ϵ'' without QDs, Maximum confinement is reached at $\epsilon''=0$, as expected.

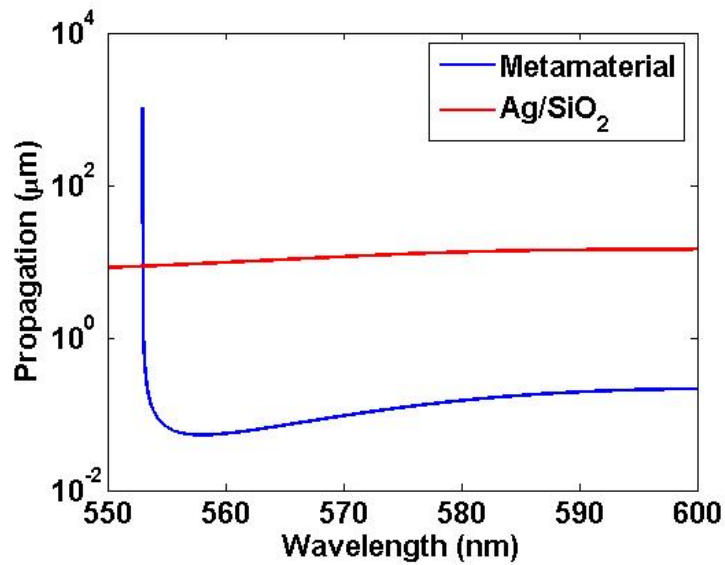


Figure 4.11 Propagation length plotted against wavelength for optimized metallodielectric metamaterial with QDs. Longer than Ag/SiO₂ surface plasmon waveguide propagation lengths are seen at $\sim 553\text{nm}$.

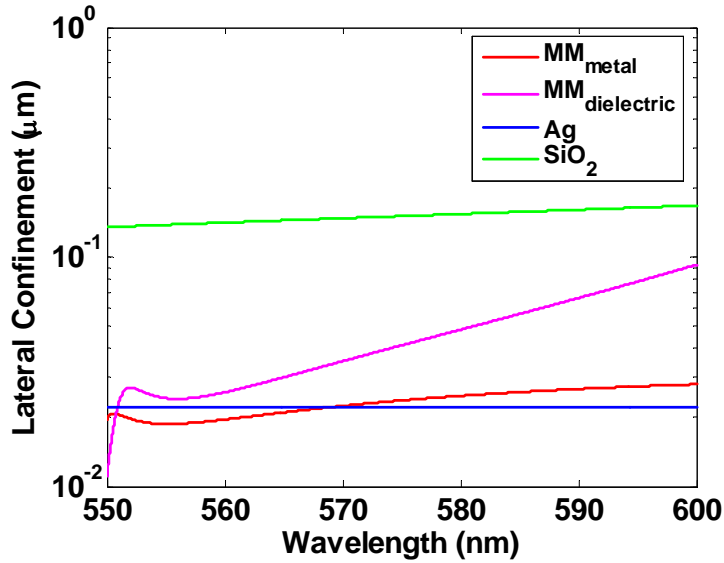


Figure 4.12 Confinement plotted against wavelength for optimized metallodielectric metamaterial with QDs. Confinement in the “metal” and “dielectric” are shown to be <50nm at the wavelengths of longest propagation (~553nm).

Conclusion

We have analyzed metamaterials composed of silver nanospheres embedded in a dielectric background and also the combination of silver nanospheres and quantum dots in such a dielectric host. In the former case, a range of positive as well as negative macroscopic ϵ can be generated, but it is found that these metamaterials, when designed for negative ϵ_{MAC}' actually have ϵ_{MAC}'' , comparable to bulk silver at the wavelengths investigated, even in optimized metamaterial structures. When adding fully inverted two level systems with linewidths on the order of 6 meV and dipole moments on the order of 1 nm times electron charge, it is found that one can combine negative ϵ_{MAC}' with low loss or gain, capitalizing on a large epsilon of the embedding dielectric. The feasibility of such a medium is a subject of further research.

The results above were used to analyze near resonant planar surface plasmon waveguides, based on metamaterials on both sides of the interface, for high lateral field confinement as well as large effective indices. The characteristics of such a structure were compared to a reference Ag-SiO₂ plasmonic waveguide. The comparison was carried out for the hypothetical case of ϵ'' of silver as a free parameter (actually changing ϵ'' also changes the real part, due to Kramers-Krönig) and it was found that the metamaterial structure is inferior to the reference system regarding propagation length but superior with respect to confinement when ϵ'' approaches zero. When introducing QD gain in the system, the metamaterial waveguide is superior to the Ag-SiO₂ reference system when one approaches the QD resonance. It should also be pointed out that the near resonant planar surface plasmon waveguide structure can in turn be used to generate channel waveguides, resonators, filters etc.

The future progress of plasmonics for integrated photonics, at least for generically useful devices, seems to be very much tied to the possibilities to decrease the optical losses. Introducing gain, in the shape of simple two-level systems or quantum dots, as was analyzed, is an interesting option, however, apart from feasibility considerations, the compensation of distributed losses will introduce noise [107], which also has to be taken into account.

It should be noted that the high positive ϵ of the metamaterial can give higher refractive index than e.g. silicon, and thus can also be interesting to use in conventional total internal reflection type waveguides to generate tightly confined fields. However, the losses are still an issue, though marginally lower, as analyzed above in Table 4.1.

In the quest for high confinement, large effective index structures and effective wavelengths in the 10 nm size range, photonic crystal like effects have to be considered, since the wavelength in the medium will eventually be of the same order as the nanostructures involved. Thus, future work should include ab initio material and electromagnetic simulations, in order to model the complex interplay between the embedding matrix, nanoparticles and amplification nanoparticles, hence establishing a solid basis for the feasibility of negative epsilon materials with ultra-low losses and the resulting possibility for ultra-compact integrated photonics.

BIBLIOGRAPHY

- [1] C. Huygens, *Horologium oscillatorium sive de motu pendularium*. 1675.
- [2] H. L. Stover and W. H. Steier, "LOCKING OF LASER OSCILLATORS BY LIGHT INJECTION," *Applied Physics Letters*, vol. 8, no. 4, pp. 91–93, Feb. 1966.
- [3] R. Lang, "Injection locking properties of a semiconductor laser," *IEEE Journal of Quantum Electronics*, vol. 18, no. 6, pp. 976–983, Jun. 1982.
- [4] S. Kobayashi and T. Kimura, "Injection locking characteristics of an AlGaAs semiconductor laser," *IEEE Journal of Quantum Electronics*, vol. 16, no. 9, pp. 915–917, Sep. 1980.
- [5] S. Kobayashi and T. Kimura, "Injection locking in AlGaAs semiconductor laser," *IEEE Journal of Quantum Electronics*, vol. 17, no. 5, pp. 681–689, May 1981.
- [6] T. B. Simpson, J. M. Liu, K. F. Huang, K. Tai, C. M. Clayton, A. Gavrielides, and V. Kovanis, "Cavity enhancement of resonant frequencies in semiconductor lasers subject to optical injection," *Phys. Rev. A*, vol. 52, no. 6, p. R4348–R4351, Dec. 1995.
- [7] G. Yabre, "Effect of relatively strong light injection on the chirp-to-power ratio and the 3 dB bandwidth of directly modulated semiconductor lasers," *Journal of Lightwave Technology*, vol. 14, no. 10, pp. 2367–2373, Oct. 1996.
- [8] J. Wang, M. K. Haldar, L. Li, and F. V.C. Mendis, "Enhancement of modulation bandwidth of laser diodes by injection locking," *IEEE Photonics Technology Letters*, vol. 8, no. 1, pp. 34–36, Jan. 1996.
- [9] Xue Jun Meng, Tai Chau, and M. C. Wu, "Experimental demonstration of modulation bandwidth enhancement in distributed feedback lasers with external light injection," *Electronics Letters*, vol. 34, no. 21, pp. 2031–2032, Oct. 1998.
- [10] Xue Jun Meng, Tai Chau, and M. C. Wu, "Improved intrinsic dynamic distortions in directly modulated semiconductor lasers by optical injection locking," *IEEE Transactions on Microwave Theory and Techniques*, vol. 47, no. 7, pp. 1172–1176, Jul. 1999.
- [11] T. B. Simpson, J. M. Liu, and A. Gavrielides, "Small-signal analysis of modulation characteristics in a semiconductor laser subject to strong optical injection," *IEEE Journal of Quantum Electronics*, vol. 32, no. 8, pp. 1456–1468, Aug. 1996.
- [12] S. Piazzolla, P. Spano, and M. Tamburrini, "Small signal analysis of frequency chirping in injection-locked semiconductor lasers," *IEEE Journal of Quantum Electronics*, vol. 22, no. 12, pp. 2219–2223, Dec. 1986.
- [13] K. Iiyama, K. Hayashi, and Y. Ida, "Simple method for measuring the linewidth enhancement factor of semiconductor lasers by optical injection locking," *Opt. Lett.*, vol. 17, no. 16, pp. 1128–1130, 1992.
- [14] H. F. Chen, J. M. Liu, and T. B. Simpson, "Response characteristics of direct current modulation on a bandwidth-enhanced semiconductor laser under strong injection locking," *Optics Communications*, vol. 173, no. 1–6, pp. 349–355, Jan. 2000.
- [15] R. Hui, "Optical PSK modulation using injection-locked DFB semiconductor lasers," *IEEE Photonics Technology Letters*, vol. 2, no. 10, pp. 743–746, Oct. 1990.
- [16] S. Kobayashi and T. Kimura, "Optical Phase Modulation in an Injection Locked AlGaAs Semiconductor Laser," *IEEE Transactions on Microwave Theory and Techniques*, vol. 30, no. 10, pp. 1650–1657, Oct. 1982.
- [17] T. B. Simpson, J. M. Liu, and A. Gavrielides, "Bandwidth enhancement and broadband noise reduction in injection-locked semiconductor lasers," *IEEE Photonics Technology Letters*, vol. 7, no. 7, pp. 709–711, Jul. 1995.

- [18] A. Murakami, K. Kawashima, and K. Atsuki, "Cavity resonance shift and bandwidth enhancement in semiconductor lasers with strong light injection," *IEEE Journal of Quantum Electronics*, vol. 39, no. 10, pp. 1196–1204, Oct. 2003.
- [19] S. Mohrdiek, H. Burkhard, and H. Walter, "Chirp reduction of directly modulated semiconductor lasers at 10 Gb/s by strong CW light injection," *Journal of Lightwave Technology*, vol. 12, no. 3, pp. 418–424, Mar. 1994.
- [20] N. Olsson, H. Temkin, R. Logan, L. Johnson, G. Dolan, J. van der Ziel, and J. Campbell, "Chirp-free transmission over 82.5 km of single mode fibers at 2 Gbit/s with injection locked DFB semiconductor lasers," *Journal of Lightwave Technology*, vol. 3, no. 1, pp. 63–67, Feb. 1985.
- [21] T. B. Simpson and J. M. Liu, "Enhanced modulation bandwidth in injection-locked semiconductor lasers," *IEEE Photonics Technology Letters*, vol. 9, no. 10, pp. 1322–1324, Oct. 1997.
- [22] Y. Okajima, S. Hwang, and J. Liu, "Experimental observation of chirp reduction in bandwidth-enhanced semiconductor lasers subject to strong optical injection," *Optics Communications*, vol. 219, no. 1–6, pp. 357–364, Apr. 2003.
- [23] C. Lin, J. K. Andersen, and F. Mengel, "Frequency chirp reduction in a 2.2 Gbit/s directly modulated InGaAsP semiconductor laser by CW injection," *Electronics Letters*, vol. 21, no. 2, pp. 80–81, Jan. 1985.
- [24] I. Petitbon, P. Gallion, G. Debarge, and C. Chabran, "Locking bandwidth and relaxation oscillations of an injection-locked semiconductor laser," *IEEE Journal of Quantum Electronics*, vol. 24, no. 2, pp. 148–154, Feb. 1988.
- [25] H.-K. Sung, T. Jung, M. C. Wu, D. Tishinin, T. Tanbun-Ek, K. Y. Liou, and W. T. Tsang, "Modulation bandwidth enhancement and nonlinear distortion suppression in directly modulated monolithic injection-locked DFB lasers," in *International Topical Meeting on Microwave Photonics, 2003. MWP 2003 Proceedings*, 2003, pp. 27–30.
- [26] J. M. Liu, H. F. Chen, X. J. Meng, and T. B. Simpson, "Modulation bandwidth, noise, and stability of a semiconductor laser subject to strong injection locking," *IEEE Photonics Technology Letters*, vol. 9, no. 10, pp. 1325–1327, Oct. 1997.
- [27] Y. Hong, P. S. Spencer, P. Rees, and K. A. Shore, "Optical injection dynamics of two-mode vertical cavity surface-emitting semiconductor lasers," *IEEE Journal of Quantum Electronics*, vol. 38, no. 3, pp. 274–278, Mar. 2002.
- [28] C. Lin and F. Mengel, "Reduction of frequency chirping and dynamic linewidth in high-speed directly modulated semiconductor lasers by injection locking," *Electronics Letters*, vol. 20, no. 25, pp. 1073–1075, Dec. 1984.
- [29] X. Jin and S. L. Chuang, "Relative intensity noise characteristics of injection-locked semiconductor lasers," *Applied Physics Letters*, vol. 77, no. 9, p. 1250, 2000.
- [30] K. Iwashita and K. Nakagawa, "Suppression of Mode Partition Noise by Laser Diode Light Injection," *IEEE Transactions on Microwave Theory and Techniques*, vol. 30, no. 10, pp. 1657–1662, Oct. 1982.
- [31] Hua Li, T. L. Lucas, J. G. McInerney, M. W. Wright, and R. A. Morgan, "Injection locking dynamics of vertical cavity semiconductor lasers under conventional and phase conjugate injection," *IEEE Journal of Quantum Electronics*, vol. 32, no. 2, pp. 227–235, Feb. 1996.

- [32] L. Chrostowski, Chih-Hao Chang, and C. J. Chang-Hasnain, "Enhancement of dynamic range in 1.55- μm VCSELs using injection locking," *IEEE Photonics Technology Letters*, vol. 15, no. 4, pp. 498–500, Apr. 2003.
- [33] E. K. Lau, Hyuk-Kee Sung, and M. C. Wu, "Frequency Response Enhancement of Optical Injection-Locked Lasers," *IEEE Journal of Quantum Electronics*, vol. 44, no. 1, pp. 90–99, Jan. 2008.
- [34] X. Zhao, B. Zhang, L. Christen, D. Parekh, W. Hofmann, M. C. Amann, F. Koyama, A. E. Willner, and C. J. Chang-Hasnain, "Greatly increased fiber transmission distance with an optically injection-locked vertical-cavity surface-emitting laser," *Opt. Express*, vol. 17, no. 16, pp. 13785–13791, 2009.
- [35] Xiaoxue Zhao, D. Parekh, E. Lau, Hyuk-Kee Sung, M. C. Wu, and C. J. Chang-Hasnain, "High-Speed Laser Transmitters Using Cascaded Optical Injection Locking," in *Nano-Optoelectronics Workshop, 2007. i-NOW '07. International*, 2007, pp. 196–197.
- [36] Chih-Hao Chang, L. Chrostowski, and C. J. Chang-Hasnain, "Injection locking of VCSELs," *IEEE Journal of Selected Topics in Quantum Electronics*, vol. 9, no. 5, pp. 1386–1393, Oct. 2003.
- [37] L. Chrostowski, C. H. Chang, and C. J. Chang-Hasnain, "Injection-locked 1.55 μm VCSELs with enhanced spur-free dynamic range," *Electronics Letters*, vol. 38, no. 17, pp. 965–967, Aug. 2002.
- [38] L. Chrostowski, Chih-Hao Chang, and C. J. Chang-Hasnain, "Injection-locked 1.55- μm tunable VCSEL for uncooled WDM transmitter applications," *IEEE Photonics Technology Letters*, vol. 16, no. 3, pp. 888–890, Mar. 2004.
- [39] L. Chrostowski, Xiaoxue Zhao, and C. J. Chang-Hasnain, "Microwave performance of optically injection-locked VCSELs," *IEEE Transactions on Microwave Theory and Techniques*, vol. 54, no. 2, pp. 788–796, Feb. 2006.
- [40] X. Zhao, D. Parekh, E. K. Lau, H.-K. Sung, M. C. Wu, W. Hofmann, M. C. Amann, and C. J. Chang-Hasnain, "Novel cascaded injection-locked 1.55- μm VCSELs with 66 GHz modulation bandwidth," *Opt. Express*, vol. 15, no. 22, pp. 14810–14816, Oct. 2007.
- [41] E. Wong, Xiaoxue Zhao, C. J. Chang-Hasnain, W. Hofmann, and M. C. Amann, "Optically Injection-Locked 1.55- μm VCSELs as Upstream Transmitters in WDM-PONs," *IEEE Photonics Technology Letters*, vol. 18, no. 22, pp. 2371–2373, Nov. 2006.
- [42] L. Chrostowski, C.-H. Chang, and C. Chang-Hasnain, "Reduction of relative intensity noise and improvement of spur-free dynamic range of an injection locked VCSEL," in *The 16th Annual Meeting of the IEEE Lasers and Electro-Optics Society, 2003. LEOS 2003*, 2003, vol. 2, pp. 706–707 vol.2.
- [43] E. K. Lau, H.-K. Sung, and M. C. Wu, "Scaling of resonance frequency for strong injection-locked lasers," *Opt. Lett.*, vol. 32, no. 23, pp. 3373–3375, Dec. 2007.
- [44] Elaine Wong, Xiaoxue Zhao, C. J. Chang-Hasnain, W. Hofmann, and M. C. Amann, "Uncooled, Optical Injection-Locked 1.55 μm VCSELs for Upstream Transmitters in WDM-PONs," in *Optical Fiber Communication Conference, 2006 and the 2006 National Fiber Optic Engineers Conference. OFC 2006*, 2006, pp. 1–3.
- [45] Xiaoxue Zhao, E. K. Lau, D. Parekh, Hyuk-Kee Sung, W. Hofmann, M. C. Amann, M. C. Wu, and C. J. Chang-Hasnain, "107-GHz Resonance Frequency of 1.55- μm VCSELs under ultra-high optical injection locking," in *Conference on Lasers and Electro-Optics, 2008 and 2008 Conference on Quantum Electronics and Laser Science. CLEO/QELS 2008*, 2008, pp. 1–2.

- [46] X. Zhao, M. Moewe, L. Chrostowski, C.-H. Chang, R. Shau, M. Ortsiefer, M.-C. Amann, and C. J. Chang-Hasnain, "28 GHz optical injection-locked 1.55 μm VCSELs," *Electronics Letters*, vol. 40, no. 8, pp. 476–478, Apr. 2004.
- [47] L. Chrostowski, X. Zhao, C. J. Chang-Hasnain, R. Shau, M. Ortsiefer, and M. C. Amann, "50 GHz directly-modulated injection-locked 1.55 μm VCSELs," in *Optical Fiber Communication Conference, 2005. Technical Digest. OFC/NFOEC, 2005*, vol. 4.
- [48] L. Chrostowski, X. Zhao, C. J. Chang-Hasnain, R. Shau, M. Ortsiefer, and M.-C. Amann, "Very high resonance frequency (>40 GHz) optical injection-locked 1.55 μm VCSELs," in *2004 IEEE International Topical Meeting on Microwave Photonics, 2004. MWP'04, 2004*, pp. 255–258.
- [49] W. E. Lamb, "Theory of an Optical Maser," *Physical Review*, vol. 134, pp. 1429–1450, Jun. 1964.
- [50] W. Yang, P. Guo, D. Parekh, and C. J. Chang-Hasnain, "Reflection-mode optical injection locking," *Opt Express*, vol. 18, no. 20, pp. 20887–20893, Sep. 2010.
- [51] F. Mogensen, H. Olesen, and G. Jacobsen, "Locking conditions and stability properties for a semiconductor laser with external light injection," *IEEE Journal of Quantum Electronics*, vol. 21, no. 7, pp. 784–793, Jul. 1985.
- [52] W. Hofmann, N. H. Zhu, M. Ortsiefer, G. Bohm, Y. Liu, and M.-C. Amann, "High speed (>11 GHz) modulation of BCB-passivated 1.55 μm InGaAlAs-InP VCSELs," *Electronics Letters*, vol. 42, no. 17, pp. 976–977, Aug. 2006.
- [53] E. K. Lau, X. Zhao, H.-K. Sung, D. Parekh, C. Chang-Hasnain, and M. C. Wu, "Strong optical injection-locked semiconductor lasers demonstrating > 100 -GHz resonance frequencies and 80-GHz intrinsic bandwidths," *Opt. Express*, vol. 16, no. 9, pp. 6609–6618, Apr. 2008.
- [54] C. J. Chang-Hasnain, J. P. Harbison, G. Hasnain, A. C. Von Lehmen, L. T. Florez, and N. G. Stoffel, "Dynamic, polarization, and transverse mode characteristics of vertical cavity surface emitting lasers," *IEEE Journal of Quantum Electronics*, vol. 27, no. 6, pp. 1402–1409, Jun. 1991.
- [55] Ning Hua Zhu, Wei Li, Ji Mim Wen, Wei Han, Wei Chen, and Liang Xie, "Enhanced Modulation Bandwidth of a Fabry-Pérot Semiconductor Laser Subject to Light Injection From Another Fabry-Pérot Laser," *IEEE Journal of Quantum Electronics*, vol. 44, no. 6, pp. 528–535, Jun. 2008.
- [56] A. Valle, I. Gatere, K. Panajotov, and M. Sciamanna, "Transverse Mode Switching and Locking in Vertical-Cavity Surface-Emitting Lasers Subject to Orthogonal Optical Injection," *IEEE Journal of Quantum Electronics*, vol. 43, no. 4, pp. 322–333, Apr. 2007.
- [57] J. Y. Law, G. H. M. van Tartwijk, and G. P. Agrawal, "Effects of transverse-mode competition on the injection dynamics of vertical-cavity surface-emitting lasers," *Quantum and Semiclassical Optics: Journal of the European Optical Society Part B*, vol. 9, no. 5, pp. 737–747, Oct. 1997.
- [58] D. Parekh, X. Zhao, W. Hofmann, M. C. Amann, L. A. Zenteno, and C. J. Chang-Hasnain, "Greatly enhanced modulation response of injection-locked multimode VCSELs," *Opt. Express*, vol. 16, no. 26, pp. 21582–21586, Dec. 2008.
- [59] D. Parekh, Xiaoxue Zhao, W. Hofmann, M. C. Amann, and C. J. Chang-Hasnain, "Systematic study on locking stability and frequency response of injection-locked multimode VCSELs," in *IEEE Lasers and Electro-Optics Society, 2008. LEOS 2008. 21st Annual Meeting of the*, 2008, pp. 324–325.

- [60] Wen-Jr Jiang, Chun-Ting Lin, Han-Sheng Huang, Po-Tsung Shih, J. Chen, and Sien Chi, "60-GHz photonic vector signal generation employing frequency quadrupling scheme for radio-over-fiber link," in *Conference on Optical Fiber Communication - includes post deadline papers, 2009. OFC 2009*, 2009, pp. 1–3.
- [61] A. Ng'oma, M. Sauer, J. George, and D. Thelen, "Bit-rate doubling in multi-Gbps wideband ASK-modulated 60 GHz RoF links using linear feed-forward equalisation and direct conversion transceivers," in *34th European Conference on Optical Communication, 2008. ECOC 2008*, 2008, pp. 1–2.
- [62] M. Weiss, A. Stohr, M. Huchard, S. Fedderwitz, B. Charbonnier, V. Rymanov, S. Babel, and D. Jager, "60GHz radio-over-fibre wireless system for bridging 10Gb/s ethernet links," in *34th European Conference on Optical Communication, 2008. ECOC 2008*, 2008, pp. 1–2.
- [63] C. Lim, A. Nirmalathas, M. Bakaul, K.-L. Lee, D. Novak, and R. Waterhouse, "Mitigation strategy for transmission impairments in millimeter-wave radio-over-fiber networks [Invited]," *J. Opt. Netw.*, vol. 8, no. 2, pp. 201–214, Feb. 2009.
- [64] Hyuk-Kee Sung, E. K. Lau, and M. C. Wu, "Near-single sideband modulation in strong optical injection-locked semiconductor lasers," in *Optical Fiber Communication Conference, 2006 and the 2006 National Fiber Optic Engineers Conference. OFC 2006*, 2006.
- [65] F. Devaux, Y. Sorel, and J. F. Kerdiles, "Simple measurement of fiber dispersion and of chirp parameter of intensity modulated light emitter," *Journal of Lightwave Technology*, vol. 11, no. 12, pp. 1937–1940, Dec. 1993.
- [66] B. Wedding, "Analysis of fibre transfer function and determination of receiver frequency response for dispersion supported transmission," *Electronics Letters*, vol. 30, no. 1, pp. 58–59, Jan. 1994.
- [67] C. Lim, M. Attygalle, A. Nirmalathas, D. Novak, and R. Waterhouse, "Analysis of optical carrier-to-sideband ratio for improving transmission performance in fiber-radio links," *IEEE Transactions on Microwave Theory and Techniques*, vol. 54, no. 5, pp. 2181–2187, May 2006.
- [68] X. S. Yao, L. Maleki, and D. Eliyahu, "Progress in the opto-electronic oscillator - a ten year anniversary review," in *Microwave Symposium Digest, 2004 IEEE MTT-S International*, 2004, vol. 1, pp. 287–290 Vol.1.
- [69] X. S. Yao and L. Maleki, "Optoelectronic oscillator for photonic systems," *IEEE Journal of Quantum Electronics*, vol. 32, no. 7, pp. 1141–1149, Jul. 1996.
- [70] Xiaoxue Zhao, D. Parekh, Hyuk-Kee Sung, E. Lau, M. C. Wu, and C. J. Chang-Hasnain, "Optoelectronic Oscillator Using Injection-Locked VCSELs," in *The 20th Annual Meeting of the IEEE Lasers and Electro-Optics Society, 2007. LEOS 2007*, 2007, pp. 190–191.
- [71] Bo Zhang, Xiaoxue Zhao, D. Parekh, Yang Yue, W. Hofmann, M. C. Amann, C. J. Chang-Hasnain, and A. E. Willner, "Reconfigurable Multifunctional Operation Using Optical Injection-Locked Vertical-Cavity Surface-Emitting Lasers," *Journal of Lightwave Technology*, vol. 27, no. 15, pp. 2958–2963, Aug. 2009.
- [72] Bo Zhang, Xiaoxue Zhao, L. Christen, D. Parekh, W. Hofmann, M. C. Wu, M. C. Amann, C. J. Chang-Hasnain, and A. E. Willner, "Adjustable Chirp Injection-Locked 1.55- μm VCSELs for Enhanced Chromatic Dispersion Compensation at 10-Gbit/s," in *Conference on Optical Fiber communication/National Fiber Optic Engineers Conference, 2008. OFC/NFOEC 2008*, 2008, pp. 1–3.

- [73] D. Vez, S. Eitel, S. G. Hunziker, G. Knight, M. Moser, R. Hoewel, H.-P. Gauggel, M. Brunner, A. Hold, and K. H. Gulden, "10 Gbit/s VCSELs for datacom: devices and applications," *Proceedings of SPIE*, vol. 4942, no. 1, pp. 29–43, Apr. 2003.
- [74] T. L. Koch and R. A. Linke, "Effect of nonlinear gain reduction on semiconductor laser wavelength chirping," *Applied Physics Letters*, vol. 48, no. 10, pp. 613–615, Mar. 1986.
- [75] R. Linke, "Modulation induced transient chirping in single frequency lasers," *IEEE Journal of Quantum Electronics*, vol. 21, no. 6, pp. 593–597, Jun. 1985.
- [76] D. Parekh, B. Zhang, X. Zhao, Y. Yue, W. Hofmann, M. C. Amann, A. Willner, and C. J. Chang-Hasnain, "Long Distance Single-mode Fiber Transmission of Multimode VCSELs by Injection Locking," *Optics Express*, vol. 18, p. 20552, Sep. 2010.
- [77] L.-S. Yan, Y. Wang, B. Zhang, C. Yu, J. McGeehan, L. Paraschis, and A. E. Willner, "Reach extension in 10-Gb/s directly modulated transmission systems using asymmetric and narrowband optical filtering," *Opt Express*, vol. 13, no. 13, pp. 5106–5115, Jun. 2005.
- [78] P. Guo, W. Yang, D. Parekh, C. Hong, C. Zhang, Z. Chen, and C. J. Chang-Hasnain, "MPSK modulation by optical injection locked VCSEL," in *2010 Conference on Lasers and Electro-Optics (CLEO) and Quantum Electronics and Laser Science Conference (QELS)*, 2010, pp. 1–2.
- [79] P. Pepeljugoski, D. Kuchta, Y. Kwark, P. Pleunis, and G. Kuyt, "15.6-Gb/s transmission over 1 km of next generation multimode fiber," *IEEE Photonics Technology Letters*, vol. 14, no. 5, pp. 717–719, May 2002.
- [80] P. Matthijsse, G. Kuyt, F. Gooijer, F. Achten, R. Freund, L. Molle, C. Caspar, T. Rosin, D. Schmidt, A. Beling, and T. Eckhardt, "Multimode fiber enabling 40 Gbit/s multi-mode transmission over distances >400 m," in *Optical Fiber Communication Conference, 2006 and the 2006 National Fiber Optic Engineers Conference. OFC 2006*, 2006.
- [81] S. S.-H. Yam and F. Achten, "Single wavelength 40 Gbit/s transmission over 3.4 km broad wavelength window multimode fibre," *Electronics Letters*, vol. 42, no. 10, pp. 592–594, May 2006.
- [82] Hejie Yang, S. C. . Lee, E. Tangdiongga, C. Okonkwo, H. van den Boom, F. Breyer, S. Randel, and A. Koonen, "47.4 Gb/s Transmission Over 100 m Graded-Index Plastic Optical Fiber Based on Rate-Adaptive Discrete Multitone Modulation," *Journal of Lightwave Technology*, vol. 28, no. 4, pp. 352–359, Feb. 2010.
- [83] Jeffrey Lee, F. Breyer, S. Randel, J. Zeng, F. Huijskens, H. P. van den Boom, A. M. Koonen, and N. Hanik, "24-Gb/s Transmission over 730 m of Multimode Fiber by Direct Modulation of an 850-nm VCSEL Using Discrete Multi-Tone Modulation," in *Optical Fiber Communication Conference and Exposition and The National Fiber Optic Engineers Conference*, 2007, p. PDP6.
- [84] S. C. Jeffrey Lee, F. Breyer, S. Randel, H. P. A. van den Boom, and A. M. J. Koonen, "High-speed transmission over multimode fiber using discrete multitone modulation [Invited]," *J. Opt. Netw.*, vol. 7, no. 2, pp. 183–196, Feb. 2008.
- [85] K. Szczerba, B.-E. Olsson, P. Westbergh, A. Rhodin, J. S. Gustavsson, A. Haglund, M. Karlsson, A. Larsson, and P. A. Andrekson, "37 Gbps transmission over 200 m of MMF using single cycle subcarrier modulation and a VCSEL with 20 GHz modulation bandwidth," 2010, pp. 1–3.
- [86] D. Parekh, W. Yang, W. Hofmann, M. C. Amann, and C. J. Chang-Hasnain, "Isolator-less optically injection-locked 1.55- μm vcsels for upstream transmitters in WDM-PONs," in

- Conference on Optical Fiber Communication - includes post deadline papers, 2009. OFC 2009, 2009, pp. 1–3.*
- [87] Y. Takushima, K. Y. Cho, and Y. C. Chung, “Design Issues in RSOA-based WDM PON,” in *IEEE Photonics Global@Singapore, 2008. IPGC 2008, 2008, pp. 1–4.*
- [88] L. Chrostowski, P. Bala Subrahmanyam, Y. Zhou, and C. J. Chang-Hasnain, “VCSEL tolerance to optical feedback for inter-chip optical interconnects,” in *Semiconductor Laser Conference, 2004. Conference Digest. 2004 IEEE 19th International, 2004, pp. 113–114.*
- [89] M. C. Y. Huang, Y. Zhou, and C. J. Chang-Hasnain, “A nanoelectromechanical tunable laser,” *Nature Photonics*, vol. 2, no. 3, pp. 180–184, Feb. 2008.
- [90] M. R. Watts, Minghao Qi, T. Barwicz, L. Socci, P. T. Rakich, E. P. Ippen, H. I. Smith, and A. H. Hermann, “Towards integrated polarization diversity: design, fabrication, and characterization of integrated polarization splitters and rotators,” in *Optical Fiber Communication Conference, 2005. Technical Digest. OFC/NFOEC, 2005, vol. 6.*
- [91] D. Parekh, J. Treu, W. Yang, W. Hofmann, and C. J. Chang-Hasnain, “Robustness of VCSEL-based WDM-PON using orthogonally polarized injection,” in *2010 Conference on Lasers and Electro-Optics (CLEO) and Quantum Electronics and Laser Science Conference (QELS), 2010, pp. 1–2.*
- [92] J. B. Pendry, “Negative Refraction Makes a Perfect Lens,” *Phys. Rev. Lett.*, vol. 85, no. 18, pp. 3966–3969, Oct. 2000.
- [93] L. Thylen and E. Berglind, “Plasmonics, Coherent Light Matter Interactions and Photonic Crystals: Shaping the Future of Photonics?,” in *2006 International Conference on Transparent Optical Networks, 2006, vol. 1, pp. 1–5.*
- [94] D. Dai, L. Liu, L. Wosinski, and S. He, “Design and fabrication of ultra-small overlapped AWG demultiplexer based on α -Si nanowire waveguides,” *Electronics Letters*, vol. 42, no. 7, pp. 400–402, Mar. 2006.
- [95] L. Thylén, S. He, L. Wosinski, and D. Dai, “The Moore’s Law for photonic integrated circuits,” *Journal of Zhejiang University SCIENCE A*, vol. 7, no. 12, pp. 1961–1967, Dec. 2006.
- [96] J. A. Dionne, L. A. Sweatlock, H. A. Atwater, and A. Polman, “Planar metal plasmon waveguides: frequency-dependent dispersion, propagation, localization, and loss beyond the free electron model,” *Phys. Rev. B*, vol. 72, no. 7, p. 075405, 2005.
- [97] A. Karalis, E. Lidorikis, M. Ibanescu, J. D. Joannopoulos, and M. Soljačić, “Surface-Plasmon-Assisted Guiding of Broadband Slow and Subwavelength Light in Air,” *Phys. Rev. Lett.*, vol. 95, no. 6, p. 063901, 2005.
- [98] A. N. Oraevskii and I. E. Protsenko, “High refractive index and other optical properties of heterogeneous media,” *Journal of Experimental and Theoretical Physics Letters*, vol. 72, no. 9, pp. 445–448, Nov. 2000.
- [99] A. N. Oraevsky and I. E. Protsenko, “Optical properties of heterogeneous media,” *Quantum Electronics*, vol. 31, no. 3, pp. 252–256, Mar. 2001.
- [100] N. M. Lawandy, “Localized surface plasmon singularities in amplifying media,” *Applied Physics Letters*, vol. 85, no. 21, pp. 5040–5042, Nov. 2004.
- [101] P. B. Johnson and R. W. Christy, “Optical Constants of the Noble Metals,” *Phys. Rev. B*, vol. 6, no. 12, pp. 4370–4379, Dec. 1972.
- [102] S. Riiikonen, I. Romero, and F. J. García de Abajo, “Plasmon tunability in metallodielectric metamaterials,” *Phys. Rev. B*, vol. 71, no. 23, p. 235104, Jun. 2005.

- [103] V. I. Klimov, A. A. Mikhailovsky, S. Xu, A. Malko, J. A. Hollingsworth, C. A. Leatherdale, H.-J. Eisler, and M. G. Bawendi, "Optical Gain and Stimulated Emission in Nanocrystal Quantum Dots," *Science*, vol. 290, no. 5490, pp. 314–317, Oct. 2000.
- [104] D. J. Norris and M. G. Bawendi, "Measurement and assignment of the size-dependent optical spectrum in CdSe quantum dots," *Phys. Rev. B*, vol. 53, no. 24, pp. 16338–16346, Jun. 1996.
- [105] M. Shim and P. Guyot-Sionnest, "Permanent dipole moment and charges in colloidal semiconductor quantum dots," *The Journal of Chemical Physics*, vol. 111, no. 15, pp. 6955–6964, Oct. 1999.
- [106] M. Nezhad, K. Tetz, and Y. Fainman, "Gain assisted propagation of surface plasmon polaritons on planar metallic waveguides," *Opt. Express*, vol. 12, no. 17, pp. 4072–4079, 2004.
- [107] E. Berglind and L. Gillner, "Optical quantum noise treated with classical electrical network theory," *IEEE Journal of Quantum Electronics*, vol. 30, no. 3, pp. 846–853, Mar. 1994.